



**HAL**  
open science

# In silico thrombosis risk analysis for left ventricular assist device implantation

Amal Ben Abid

► **To cite this version:**

Amal Ben Abid. In silico thrombosis risk analysis for left ventricular assist device implantation. Human health and pathology. Université de Rennes, 2022. English. NNT : 2022REN1B051 . tel-04122048

**HAL Id: tel-04122048**

**<https://theses.hal.science/tel-04122048v1>**

Submitted on 8 Jun 2023

**HAL** is a multi-disciplinary open access archive for the deposit and dissemination of scientific research documents, whether they are published or not. The documents may come from teaching and research institutions in France or abroad, or from public or private research centers.

L'archive ouverte pluridisciplinaire **HAL**, est destinée au dépôt et à la diffusion de documents scientifiques de niveau recherche, publiés ou non, émanant des établissements d'enseignement et de recherche français ou étrangers, des laboratoires publics ou privés.

# THESE DE DOCTORAT DE

L'UNIVERSITE DE RENNES 1

ECOLE DOCTORALE N° 605

*Biologie Santé*

Spécialité : « Analyse et traitement de l'information et des images médicales »

Par

« **Amal Ben Abid** »

« **In silico thrombosis risk analysis for left ventricular assist device  
implantation** »

Thèse présentée et soutenue à Rennes, le 07 Novembre 2022

Unité de recherche : Laboratoire Traitement du Signal et de l'Image (LTSI), UMR Inserm 1099

## Rapporteurs avant soutenance :

## Composition du Jury :

Virginie Fouilloux

PU-PH Université Aix Marseille,  
AP HM, Dept. Chirurgie Cardiaque et  
Pédiatrique, Marseille, France

Virginie Fouilloux

PUPH, Université Aix Marseille, AP  
HM, Marseille, France

Gabriele Dubini

Professor, Politecnico di Milano,  
Milano MI, Italie

Manuel Lagache

MC, Université Savoie Mont-Blanc, Le  
Bourget du Lac, France

### Président

Jean-Christian Roussel

PUPH, Unité de recherche de l'institut  
du thorax, Nantes, France

### Directeur de thèse

Erwan Flecher

PUPH, LTSI, Université de Rennes 1,  
CHU de Rennes, France

### Co-directeur de thèse

Pascal Haigron

PU, LTSI, Université de Rennes 1,  
CHU de Rennes, France

### Invités

Amedeo Anselmi

MCPH, LTSI, Université de Rennes 1,  
CHU de Rennes, France

Michel Rochette

Senior Director of research, Ansys,  
Lyon, France

Gabriele DUBINI

Professor Department of Chemistry,  
Materials and Chemical Engineering  
'Giulio Natta' Politecnico di Milano  
Piazza Leonardo da Vinci, 32, 20133  
Milano MI, Italie.



# Contents

<b>Contents</b>	<b>iii</b>
<b>List of Figures</b>	<b>vii</b>
<b>List of Tables</b>	<b>xi</b>
<b>Nomenclature</b>	<b>xvii</b>
<b>French extended summary of the thesis</b>	<b>xix</b>
<b>Introduction</b>	<b>1</b>
<b>1 Clinical Context</b>	<b>5</b>
1.1 Cardiovascular system . . . . .	5
1.1.1 Blood circulation . . . . .	5
1.1.2 Heart anatomy . . . . .	6
1.1.3 Heart functioning . . . . .	9
1.2 Heart Failure . . . . .	13
1.2.1 Pathology and symptoms . . . . .	13
1.2.2 Diagnosis and treatments . . . . .	15
1.2.3 End-stage heart failure . . . . .	19
1.3 Mechanical Circulatory Support (MCS) devices . . . . .	20
1.3.1 Total Artificial Heart (TAH) . . . . .	22
1.3.2 Ventricular Assist Devices (VAD) . . . . .	23
1.4 MCS implantation . . . . .	24
1.4.1 Implantation criteria . . . . .	24
1.4.2 Surgical procedure . . . . .	25
1.4.3 Post-operative follow-up and eventual complications . . . . .	28
1.5 Summary . . . . .	30

<b>2</b>	<b>State of the art and Work positioning</b>	<b>31</b>
2.1	Device-structure interactions . . . . .	31
2.2	Morphological constraints . . . . .	33
2.2.1	Anatomical constraints . . . . .	33
2.2.2	Overview of the literature . . . . .	34
2.3	Mechanical and Fluid issues . . . . .	36
2.3.1	Overview . . . . .	36
2.3.2	Issues related to LV haemodynamic . . . . .	38
2.4	Computational modelling . . . . .	43
2.5	Summary and Work positioning . . . . .	47
<b>3</b>	<b>Model definition for haemodynamics analysis</b>	<b>49</b>
3.1	3D approach . . . . .	49
3.1.1	Model Presentation . . . . .	49
3.1.2	Results . . . . .	54
3.1.3	Discussion . . . . .	55
3.2	2D assumption . . . . .	57
3.2.1	Model presentation . . . . .	57
3.2.2	Results and discussion . . . . .	60
3.2.3	Conclusion . . . . .	62
3.3	2D proposed approach . . . . .	62
3.3.1	Numerical model: inlet / outlet . . . . .	62
3.3.2	Influence of inflow cannula angulation . . . . .	63
3.3.3	Influence of inflow cannula length . . . . .	68
3.4	Conclusion . . . . .	71
<b>4</b>	<b>A personalised thrombogenic potential marker</b>	<b>73</b>
4.1	Blood stagnation and thrombus formation . . . . .	73
4.2	Vortices definitions and identification . . . . .	75
4.2.1	Coherent structures . . . . .	75
4.2.2	Vorticity . . . . .	76
4.2.3	Vortices identification methods . . . . .	76
4.3	Personalised Thrombogenic Potential Marker: A Novel Digital Marker	80
4.3.1	Personalised Thrombogenic Potential Marker: definition . . . . .	81
4.3.2	Platelet Activation Potential . . . . .	81
4.3.3	Blood Stagnation score . . . . .	82
4.3.4	Anatomical Correction Factor . . . . .	86
4.3.5	Proposed Pipeline . . . . .	87
4.4	Personalised Thrombogenic Potential Marker: settings . . . . .	89
4.4.1	Clinical database . . . . .	89
4.4.2	Parameters definition . . . . .	92

4.4.3	PTPM: comparison to clinical outcome . . . . .	94
4.5	PTPM: applications for decision support . . . . .	95
4.5.1	PTPM: Influence of IC angulation . . . . .	96
4.5.2	PTPM: LV diameter . . . . .	98
4.5.3	IC length . . . . .	99
4.6	PTPM: limitation and perspective . . . . .	100
4.6.1	3D patient-specific model: Model presentation . . . . .	100
4.6.2	PTPM limitation: shape approximation . . . . .	102
4.6.3	PTPM limitation: analysis plan definition . . . . .	103
4.7	Summary and conclusion . . . . .	105
<b>Conclusion and perspectives</b>		<b>107</b>
<b>Appendices</b>		<b>111</b>
<b>A Total Artificial Hearts - TAH</b>		<b>113</b>
<b>B Ventricular Assist Device – VAD</b>		<b>117</b>
<b>C Conversion of flow rate Q</b>		<b>119</b>
<b>D Mesh independence: 3D model</b>		<b>121</b>
<b>E Mesh independence: 2D model</b>		<b>123</b>
<b>F 2D model thickness</b>		<b>125</b>
<b>Bibliography</b>		<b>127</b>

\*



# List of Figures

1	Dispositif d'assistance ventriculaire gauche. . . . .	xxii
2	Contexte et positionnement de la these. . . . .	xxiii
3	Approche 2D proposee. . . . .	xxiv
4	Différentes plage d'angulation de la CA. . . . .	xxv
1.1	Blood circulation. . . . .	6
1.2	Heart Location. . . . .	7
1.3	Superficial heart anatomy (Anterior). . . . .	8
1.4	Heart anatomy and circulation. . . . .	8
1.5	Cardiac cycle. . . . .	9
1.6	P-V Loop of cardiac cycle. . . . .	11
1.7	Cardiac conduction system. . . . .	11
1.8	PQRST wave. . . . .	12
1.9	Heart beat: electrical/mechanical coupling. . . . .	12
1.10	Prevalence of hearth failure in population-based studies around the world, in percentage, per region. . . . .	13
1.11	Differences in mortality rate of heart failure patients according to age, gender, race and condition. . . . .	14
1.12	INTERMACS classification system compared to New York Heart Association classification. . . . .	17
1.13	Heart transplant Activities in 2018. . . . .	18
1.14	Number of heart transplants (adult and pediatric) by year (transplants: 1988–2017) and geographic region. . . . .	19
1.15	Number of waiting list candidates compared to the number of transplantations by year, in France. . . . .	20
1.16	Mechanical circulatory support components; example of left ventricular assist device. . . . .	20
1.17	Implant strategies by year. . . . .	21
1.18	Normal structure and location of the heart vs total artificial heart. . . . .	22



1.19	Ventricular assist device pump: example of left ventricular assist device (HeartMate 3 - Thoratec Inc., Pleasanton, CA).	23
1.20	Ventricular assist devices categories.	24
1.21	Conventional incision - sternotomy.	26
1.22	Minimal invasive incision – thoracotomy.	26
1.23	Extra-Corporeal Circulation (ECC).	27
1.24	Mechanical circulatory support implantation - Surgical captures.	27
1.25	Total artificial heart implantation -Surgical steps.	28
1.26	Left ventricular assist device implantation -Surgical steps.	29
2.1	Different anatomical structures interacting with the LVAD device.	31
2.2	State of the art of MCS numerical approaches.	35
2.3	IC insertion: aligned IC vs. angled IC	42
2.4	Postoperative radiographs illustrating two IC angulations of the HM2.	42
2.5	Summary of IC influential features and related consequences.	43
2.6	Work positioning.	48
3.1	Model definition, with LV features (A) and IC features (B).	50
3.2	Phases of virtual ink technique.	52
3.3	3D approach: Numerical Model.	53
3.4	CFD simulation results for C3 (top) and C14 (bottom) for both IC angulation $0^\circ$ (IC0) and $20^\circ$ (IC20).	56
3.5	Relationship between 2D and 3D models.	58
3.6	Model definition with LV features (A) and IC features (B).	59
3.7	2D assumption: Numerical model.	60
3.8	Simulation results for C3 in 3D (top) and 2D (bottom).	60
3.9	Simulation results for C14 in 3D (top) and 2D (bottom).	61
3.10	2D model: Input / output.	63
3.11	Proposed Numerical Model.	64
3.12	IC angulation: Velocity path-lines for case C3.	65
3.13	IC angulation: Velocity path-lines for case C14.	65
3.14	IC angulation: RIC for case C3.	66
3.15	IC angulation: RIC for case C14.	66
3.16	Angulation ranges based on the RIC distribution.	67
3.17	WSS max as a function of IC angulations, for C3 and C14.	68
3.18	IC length: Velocity pathlines for case C3.	69
3.19	IC length: Velocity pathlines for case C14.	69
3.20	IC length: RIC for case C3.	70
3.21	IC length: RIC for case C14.	70
4.1	Transfer function of the Platelet Activation Potential	81
4.2	Summary of the main steps to evaluate blood stagnation regions.	84

4.3	Image segmentation process based on vortices identification. . . . .	85
4.4	Transfer functions associated with the blood stagnation attributes. . . . .	86
4.5	Representation of the sphericity index computation of the left ventricle. . . . .	87
4.6	Personalised Thrombogenic Potential Marker pipeline. . . . .	88
4.7	Ultrasound images in long axis parasternal (above: A/B) and 4-chamber (below: C/D) views during diastolic phase for patients with bad (right: B/D) vs. good (left: A/C) echogenicity. . . . .	90
4.8	LV measures in diastolic phase from Ultrasound images of LV-D mea- sure in long axis parasternal view (A) and measures of LV-H and VM- D in 4-chamber view (B and C, respectively). . . . .	92
4.9	Ultrasound images during diastolic (A) and systolic (B) phases of LV- D and LV-H measures (for the same left ventricle) in 4-chamber view. . . . .	92
4.10	Measure of IC implantation angle on CT-scan. . . . .	93
4.11	ROC curve of different filling and clearing phases for HM2 patients. . . . .	93
4.12	Youden Index identification on the ROC curve. . . . .	94
4.13	Influence of LV-D variation on ventricular shape. . . . .	99
4.14	Illustration of the different geometry elaboration steps. . . . .	101
4.15	Numerical model of the CFD simulation. . . . .	101
4.16	Investigated Cases: Apical ( $0^\circ$ ) and IVS ( $90^\circ$ ) configurations. . . . .	102
4.17	2D proposed model and their corresponding 3D planes. . . . .	103
4.18	PTPM: investigated plans. . . . .	104
A.1	TAH without FDA approval. . . . .	114
A.2	TAH with FDA approval . . . . .	114
A.3	TAH prototypes. . . . .	115
B.1	First generation VADs. . . . .	117
B.2	Second generation VADs. . . . .	117
B.3	Thrid generation VADs. . . . .	118
C.1	Analytical velocity profile. . . . .	120
C.2	Average velocity profile. . . . .	120
D.1	Mesh independence: Velocity Magnitude. . . . .	121
E.1	Mesh independence: velocity magnitude. . . . .	124
E.2	Relative error for mesh size of 2 mm and 3 mm related to mean and max velocity magnitude. . . . .	124
F.1	Hypothetical IC output surface. . . . .	125



# List of Tables

1	MPTP : influence de la CA. . . . .	xxvii
1.1	NYHA functional Classification. . . . .	15
1.2	American Heart Association Heart Failure Stages. . . . .	16
2.1	Literature summarizing the factors influencing physiological modifications of the hemodynamic in the left ventricle. . . . .	45
2.2	Overview of the main CFD models limitations encountered in the literature. . . . .	46
3.1	Investigated cases. . . . .	50
3.2	HM2 pump properties. . . . .	51
3.3	QOI reading grid for thrombogenic analysis. . . . .	54
3.4	QOI reading grid of both IC angulations for C3. . . . .	55
3.5	QOI reading grid of both IC angulations for C14. . . . .	57
3.6	Impact of IC angulation on WSS maximal value for both cases. . . . .	68
3.7	Impact of IC angulation on WSS maximal value for both cases. . . . .	71
4.1	Patient conditions and HM2 LVAD implantation features. . . . .	91
4.2	Patient conditions and HM3 LVAD implantation features. . . . .	91
4.3	Filling and clearing phases investigated configurations. . . . .	93
4.4	Youden Index identification. . . . .	94
4.5	PTPM obtained for HM2 implanted patients. . . . .	95
4.6	PTPM obtained for HM3 implanted patients. . . . .	96
4.7	PTPM: influence of IC angulation. . . . .	97
4.8	Variation set of LV-D and its influence on the anatomical correction factor. . . . .	98
4.9	Influence of LV-D on PTPM. . . . .	99
4.10	PTPM: influence of IC length combined with IC angulation for two patients. . . . .	100

4.11 Investigated Cases. . . . .	103
4.12 PTPM applied on different planes of the Coaxial configuration. . . . .	104
4.13 PTPM applied on different planes of the IVS configuration. . . . .	105
E.1 Computation time for 1 s of simulation time required for every mesh size. . . . .	124

# Glossary

**ADP** Adenosine DiPhosphate.

**AoV** Aortic Valve.

**ASTS** American Society of Transplant Surgeons.

**AUC** Area Under Curve.

**AV** AtrioVentricular.

**BiVAD** Bi-Ventricular Assist Device.

**BTD** Bridge to Decision.

**BTR** Bridge To Recovery.

**BTT** Bridge To Transplant.

**CFD** Computational Fluid Dynamics.

**CFL** Courant-Friedrichs-Lewy.

**CFVAD** Continuous-Flow VAD.

**Cp** Clearing phase.

**CT** Computerized Tomography.

**CVDs** CardioVascular Diseases.

**DT** Destination Therapy.

**ECC** Extra-Corporeal Circulation.

**ECG** ElectroCardioGram.

**EDP** End Diastolic Pressure.

**EDV** End Diastolic Volume.

**EF** Ejection Fraction.

**ESV** End-Systolic Volume.

**F<sub>AC</sub>** Anatomical Correction Factor.

**F<sub>p</sub>** Filling phase.

**FT** Filling Time.

**GODT** Global Observatory on Donation and Transplantation.

**HF** Heart Failure.

**HFpEF** HF with preserved Ejection Fraction.

**HF<sub>r</sub>EF** HF with reduced Ejection Fraction.

**HM2** HeartMate 2.

**HM3** HeartMate 3.

**HT** Heart Transplant.

**HTh** High Thrombogenicity.

**HVAD** HeartWare Ventricular Assist Device.

**IC** Inflow Canula.

**IC-AD** Inflow Canula Angular Deviation.

**IC-D** Inflow Canula Diameter.

**IC-L** Inflow Canula Length.

**ICD** Intra-Cardiac Device.

**INTERMACS** Interagency registry for Mechanically Assisted Circulatory Support.

**I<sub>p</sub>** Initialization phase.

**ISHLT** International Society of heart and Lung Transplant.

**IVS** Inter Ventricular Septum.

**LES** Large Eddy Simulation.

**LPM** Lumped Parameter Model.

**LV** Left Ventricle.

**LV-D** Left Ventricle - Diameter.

**LV-H** Left Ventricle - Height.

**LVAD** Left Ventricular Assist Device.

**LVHF** Left Ventricle Heart Failure.

**LVSI** Left Ventricular Sphericity Index.

**MCS** Mechanical Circulatory Support.

**MPA** Mechanical Platelet Activation.

**MRI** Magnetic Resonance Imaging.  
**MV** Mitral Valve.  
**MV-D** Mitral Valve long Diameter.  
**NYHA** New York Heart Association.  
**OC** Outflow Canula.  
**P-V** Pressure and Volume.  
**PFVAD** Pulsatile-Flow VADs.  
**PISO** Pressure Implicit with Splitting of Operators.  
**PIV** Particle Image Velocimetry.  
**PTPM** Personalised Thrombogenic Potential Marker.  
**Q** Flow Rate.  
**QOI** Quantities Of Interest.  
**RIC** Remaining Ink Concentration.  
**ROC** Receiver Operating Characteristic.  
**RT** Residence Time.  
**RV** Right Ventricle.  
**RVAD** Right Ventricular Assist Device.  
**s<sub>B</sub>** Blood Stagnation score.  
**SA** SinoAtrial.  
**SI** Sphericity Index.  
**SV** Stroke Volume.  
**TAH** Total Artificial Heart.  
**TP** Thrombogenic Potential.  
**Ts** Time step.  
**TTE** TransThoracic Echocardiography.  
**VAD** Ventricular Assist Device.  
**VL** Left ventricle Volume.  
**vWF** Von Willebrand Factor.  
**WHO** World Health Organization.  
**WSS** Wall Shear Stress.  
**YI** Youden Index.





# Nomenclature

## Scalars

$\delta x_i$	Distance component along the orthogonal axis $i$
$\epsilon$	Threshold value
$\kappa, \delta$	Positive values that ensure the orbital compactness
$\lambda_r, \lambda_{cr} \pm i\lambda_{ci}$	Eigenvalues of the velocity gradient tensor $\nabla \mathbf{u}$
$\pi$	Pi constant value
$\varphi$	Blood density
$a_{i,j}$	Acceleration gradient
$P, Q$ and $R$	Three invariants of the Cayley Hamilton theorem
$p_{i,j}$	Local pressure extremum
$u_i$	Velocity component along the orthogonal axis $i$
$\Delta t$	Time step (Ts)
$\Delta x$	Cell size
$c$	Courant number
$v$	Velocity magnitude
$Q$	Flow rate
$s$	IC output surface

## Vectors

$\mathbf{a}$	Weight vector associated with the blood stagnation risk
$p_n$	Blood stagnation risk vector
$\mathbf{u}$	Velocity fields

## Matrices

$\mathbf{\Omega}$	Vorticity tensor
$\mathbf{A}$	Second-order Cartesian tensor
$\mathbf{S}$	Rate of strain tensor

## Norms and operators

$\nabla$	Gradient operator
$\ \cdot\ _F$	Frobenius norm squared
$\overrightarrow{\text{rot}}$	Rotational or curl vector operator
$\det$	Determinant operator

## Trace function

## Exponents and indices

$n$	Normalized value
$max$	Maximum value
ED	During diastolic phase
ES	During systolic phase
$i, j, k$	Orientation indices of an orthonormal basis

## Functions and Metrics

$F_{AC}$	Anatomical correction factor
$P_{WSS}$	Platelet activation potential
$s_B$	Blood stagnation score
$p_C$	Orbital compactness attribute
$p_{RIC}$	Remaining Ink Concentration attribute
$p_{SW}$	Swirling Strength attribute
$p_V$	Velocity Magnitude attribute
ICAD	Inflow Canula Angular Deviation

LVD	Left Ventricle greater cross-sectional Diameter	<b>GHz</b>	Giga Hertz
		<b>kg</b>	Kilogram
LVL	Left Ventricle Longitudinal Length	<b>min</b>	Minute
PTPM	PTPM criterion	<b>ml.kg<sup>-1</sup>.min<sup>-1</sup></b>	Maximal Oxygen uptake <b>VO<sub>2</sub> max</b>
SI	Sphericity Index	<b>ml</b>	Milliliter
YI	Youden Index	<b>Pa</b>	Pascal
<b>Units</b>		<b>s</b>	Second
<b>dm</b>	Decimeter	<b>V</b>	Volt
<b>Gb</b>	Giga Bytes		

**French extended summary of the  
thesis**



# Résumé de la thèse

## Introduction

Dans le cadre d'un stade final de l'Insuffisance Cardiaque (IC), les dispositifs d'Assistance Circulatoire Mécanique (ACM) à longue durée sont actuellement la seule alternative à la transplantation cardiaque. Parmi ces dispositifs, les Dispositifs d'Assistance Ventriculaire Gauche (DAVG) sont les plus implantés. Ils sont implantés à l'apex du Ventricule Gauche (VG) par une Canule Apicale (CA) et à l'aorte par une canule d'éjection.

L'objectif de cette thèse est de comprendre, par des calculs d'analyse de Mécanique des Fluides Numérique (MFN), l'influence des caractéristiques de la CA, en particulier son angulation, sur le risque de thrombose, en tenant compte de l'influence de la forme du ventricule gauche. Notre but est de développer un marqueur de potentiel thrombogène personnalisé, capable d'évaluer le risque de thrombose associé à chaque angulation de la CA, pour des caractéristiques spécifiques du VG. Il s'agit d'une première étape vers l'objectif ambitieux de développer un système d'aide à la décision clinique capable de prédire l'angulation optimale du CA ayant le plus faible potentiel thrombogène. Par conséquent, une méthodologie d'aide à la décision facile à utiliser, nécessitant des calculs relativement rapides et une mise en œuvre aisée est nécessaire.

## Contexte clinique

L'IC est un état clinique dans lequel le cœur est incapable de répondre aux besoins de l'organisme. Il peut se produire lorsque le ventricule gauche se raidit et se remplit d'une quantité insuffisante de sang ou s'affaiblit et devient incapable d'éjecter une quantité suffisante de sang. Ce syndrome clinique peut apparaître soudainement (aigu) ou progressivement (chronique). En France, on compte 165000 d'hospitalisations annuelles dues à l'IC dont 45% de ré-hospitalisations et 29% de décès dans l'année (Tuppin et al., 2014). Sa gravité dépend de la capacité du cœur à pomper le

sang. Elle est classée en quatre stades. Lorsque le stade final est atteint, une Transplantation Cardiaque (TC) est nécessaire. Face à la pénurie de coeur disponible à la transplantation, l'implantation des dispositifs de ACM est la seule alternative. En fonction de l'état du patient, ces dispositifs peuvent être utilisés comme un pont vers la transplantation ou comme une thérapie de destination pour les patients qui ne sont pas éligibles pour la TC. Les dispositifs d'ACM peuvent être divisés en deux catégories : ceux qui consistent à transplanter un cœur mécanique (on parle de Transplantation Totale du Cœur (TTC)) et les Dispositifs d'Assistance Ventriculaire (DAV) qui consistent à aider le ventricule dans son fonctionnement, en implantant une CA à l'apex du ventricule et une canule d'éjection dans l'aorte (Figure 1).

Bien que l'implantation des dispositifs ACM se soit avérée être une thérapie durable et bénéfique pour les patients atteints d'IC, elle est associée à des complications, surtout à long terme, à savoir des maladies thromboemboliques et un dysfonctionnement de la pompe associés à la formation de thrombus.

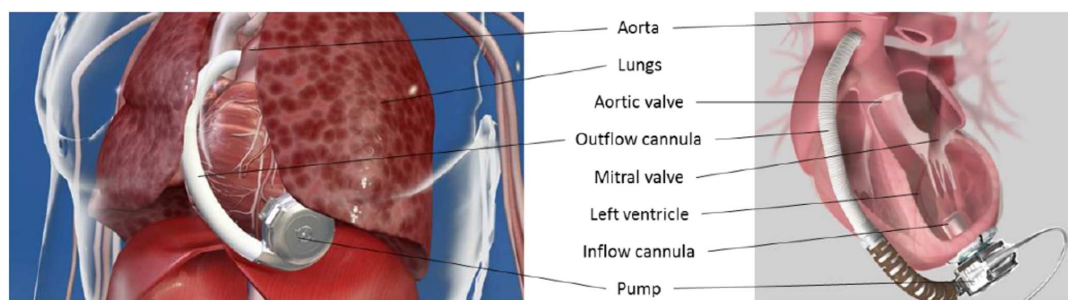


FIGURE 1 : Dispositif d'assistance ventriculaire gauche.

## État de l'art et positionnement de la thèse

Dans la littérature, la recherche s'est intéressée à l'interaction des dispositifs ACM avec l'anatomie et la physiologie des patients. Deux questions principales ont été soulevées : les problèmes morphologiques et les problèmes de fluides. Les contraintes morphologiques sont principalement liées à l'espace intrathoracique disponible pour l'implantation du dispositif ACM et la fermeture du thorax. Dans le cas de l'implantation d'un DAVG, ce problème peut entraîner une angulation du CA qui influence l'hémodynamique à l'intérieur du ventricule. Ceci nous amène à la deuxième question liée aux contraintes de fluide. Certains travaux rapportés supposent que la thrombose serait liée aux caractéristiques de la CA (forme de la canule, sa longueur et son angulation d'insertion). Ils ont étudié l'influence de ces caractéristiques sur l'hémodynamique du ventricule gauche et ont tenté d'évaluer le risque de thrombose par différents moyens. En particulier, des approches MFN ont été utilisées pour analyser différentes Quantités d'Intérêts (QI) afin d'essayer d'évaluer la stagnation du sang, l'activation plaquettaire et le risque de thrombose, car il s'agit de phénomènes com-

plexes qui ne sont pas entièrement compris. Plusieurs questions restent en suspens car les résultats sont préliminaires, voire contradictoires. La nécessité de développer un marqueur capable de prédire le risque de thrombose reste une question ouverte.

Parmi les caractéristiques de la CA, les effets de son angulation sur le flux sanguin à l'intérieur du coeur est le principal objet de notre étude. Contrairement à sa forme et sa longueur qui dépendent de la conception de la DAVG, une déviation de la CA vers le septum peut se produire à un moment donné de la procédure chirurgicale. De plus, étant donné que certains types de DAVG proposent deux longueurs de CA différentes, celle-ci sera également étudiée dans notre travail.

La Figure 2 illustre le contexte de nos travaux et leur positionnement. Cette thèse de doctorat vise plus précisément à comprendre les changements hémodynamiques qui se produisent en raison des caractéristiques de la CA (angulation et longueur) et à développer un marqueur thrombogène capable d'évaluer le risque de thrombose lié à une configuration spécifique. Le positionnement de notre travail est décrit dans la Figure .

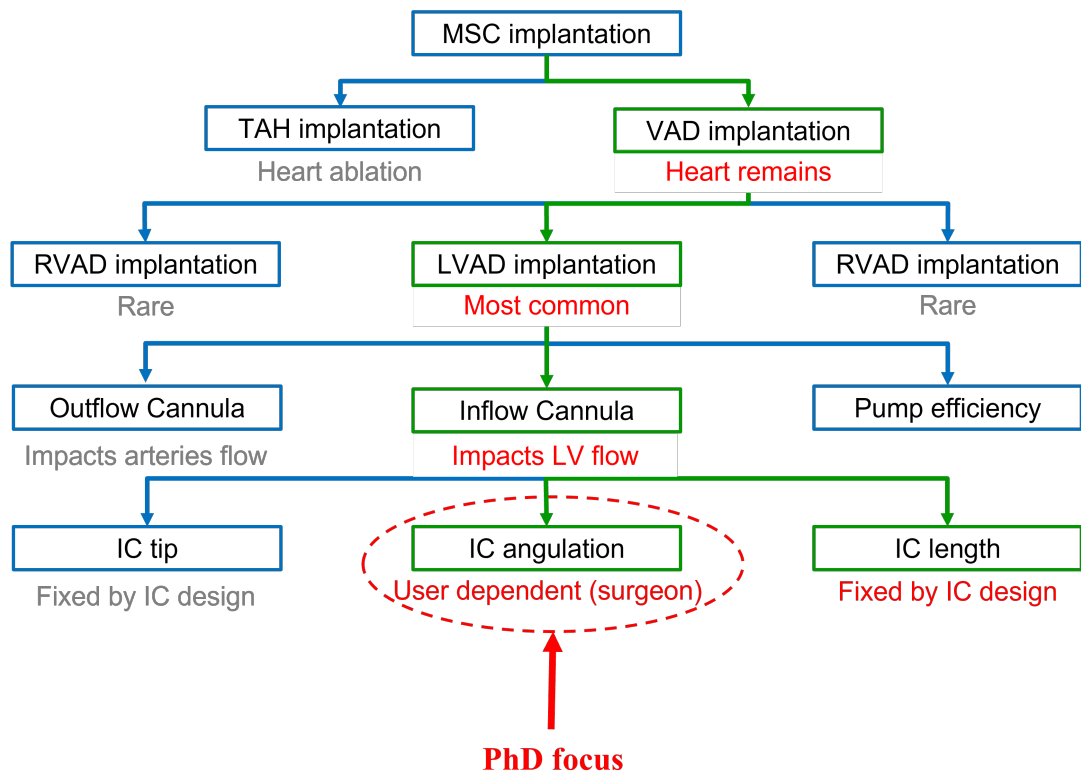


FIGURE 2 : Contexte et positionnement de la thèse.

## Définition du modèle pour l'analyse hémodynamique

L'objectif de ce chapitre est de proposer un modèle simplifié capable de permettre une meilleure compréhension de l'influence des caractéristiques de la CA, en particulier



de son angulation sur l'hémodynamique du VG et d'identifier les QI pertinentes à cette analyse.

D'abord, une approche 3D-générique a été effectuée, elle a permis de conclure que l'étude de plusieurs QI, tels que la vitesse, les contraintes de cisaillements des parois et le colorant virtuel (indicateur de l'évacuation du sang du ventricule), est pertinente et qu'une étude sur un large intervalle d'angulation permettrait de mieux comprendre le comportement hémodynamique du ventricule et des QI en fonction de l'angulation de la CA. Comme les temps de calcul des modèles 3D sont coûteux, l'analyse des modèles 2D a été envisagée. L'hypothèse 2D a été vérifiée en comparant deux modèles 3D et leurs modèles 2D correspondants où les mêmes tendances hémodynamiques ont été trouvées.

Malgré leurs limites, les modèles 2D ont montré que les tendances des différents QI en fonction de l'angulation de la CA, sont similaires à celles des modèles 3D. Les modèles 2D se sont révélés intéressants car leur analyse était plus simple et l'analyse des QI semblait pertinente. Ainsi, une approche 2D simplifiée a été proposée. Elle considère le ventricule comme une ellipse recoupée dans sa partie supérieure par la valve mitrale et insérée dans sa partie inférieure par la CA, représentée par un rectangle (Figure 3). Le VG est défini par son axe court (Left Ventricle - Diameter (LV-D)) et son axe long (Left Ventricle - Height (LV-H)), la valve mitrale est définie par son long diamètre (Mitral Valve long Diameter (MV-D)) et la CA est définie par son diamètre (Inflow Canula Diameter (IC-D)), sa longueur d'insertion (Inflow Canula Length (IC-L)) et sa déviation angulaire par rapport à l'axe long du VG (Inflow Canula Angular Deviation (IC-AD)). Le modèle considère le sang comme un fluide Newtonien dont l'écoulement est laminaire. Il admet une pression nulle en entrée, un débit massique de la pompe en sortie et des parois (LV wall, IC wall) rigides.

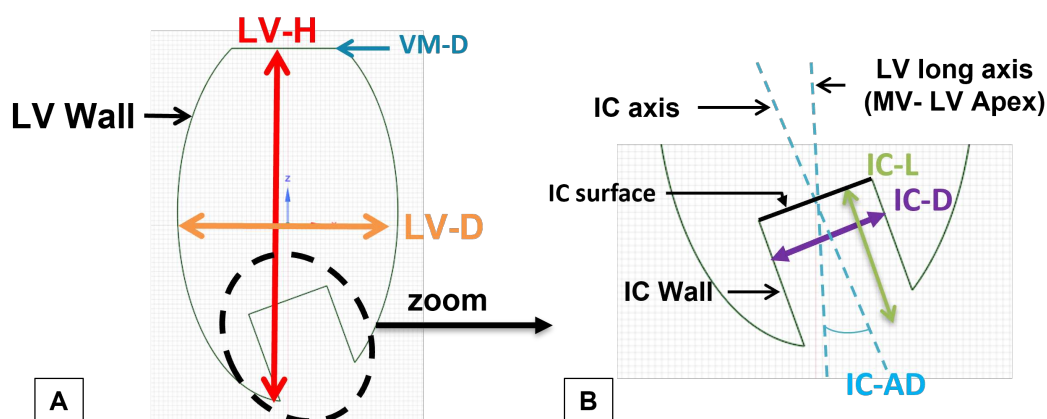


FIGURE 3 : Approche 2D proposée.

Cette approche a été utilisée pour étudier l'angulation sur un large intervalle et différentes longueurs de la CA pour deux formes de ventricule différentes.

Pour les deux cas, les résultats ont permis d'identifier les mêmes tendances dans les comportements des QI concernant les caractéristiques de la CA. Ces comportements ont identifié la formation de vortex qui ont mis en évidence la nécessité de combiner certains QI, notamment la vitesse et le colorant virtuel qui évalue l'évacuation du sang du ventricule, avec les vortex pour permettre une meilleure compréhension de la stagnation du sang. L'analyse du colorant virtuel a permis de distinguer trois plages d'angulations de la CA où le comportement des QI diffère (Figure 4).

Cependant, une analyse simple et directe des différentes QI n'est pas suffisante pour être utilisée et interprétée directement pour l'aide à la décision clinique. Un marqueur capable d'évaluer le risque de thrombose associé à une configuration spécifique (forme du VG et caractéristique de la CA) est nécessaire. Dans le chapitre suivant, un marqueur du potentiel thrombogène personnalisé est proposé.

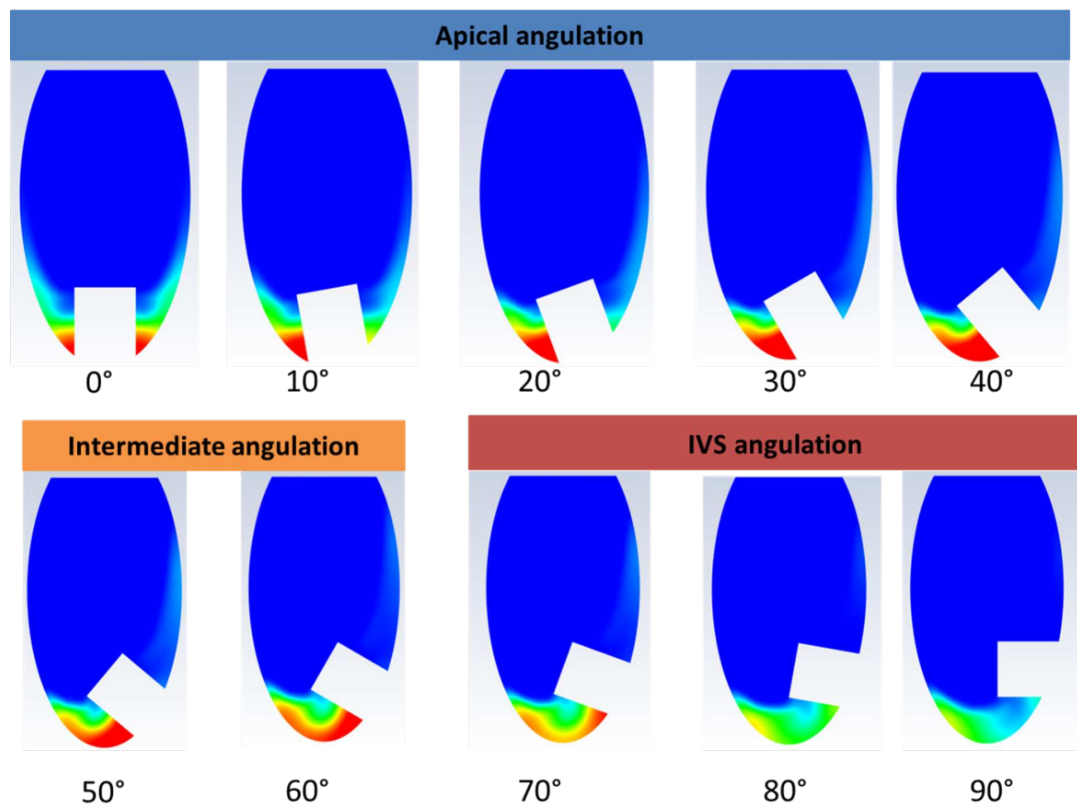


FIGURE 4 : Différentes plage d'angulation de la CA.

## Marqueur du Potentiel Thrombogène Personnalisé

Dans ce chapitre, le Marqueur du Potentiel Thrombogène Personnalisé (MPTP) a été proposé. Il s'agit d'un marqueur basé sur les vortex qui prend en compte certaines données patients telles que la morphologie du ventricule gauche (géométrie, forme ventriculaire en phases diastolique et systolique), les caractéristiques spéci-

fiques de la CA (géométrie, angle d'implantation) et les données surveillées (débit de la pompe). Il considère le potentiel d'activation plaquettaire via les contraintes de cisaillement aux parois, le score de stagnation sanguine via la vitesse et la concentration du colorant virtuel au sein de chaque vortex et les facteurs anatomiques en considérant le remodelage ventriculaire via l'indice de sphéricité du ventricule durant les phases diastolique et systolique. Le MPTP est un marqueur absolu qui ne nécessite pas de configuration comparative et qui est cohérent avec les résultats cliniques.

Nos résultats montrent que l'angulation de la CA influence le risque de thrombose (TABLEAU 1) et que cette influence dépend fortement de l'anatomie du VG. En effet, aucune angulation spécifique n'était optimale ou recommandée pour tous les patients. Nous avons remarqué que le MPTP moyen obtenu pour un large intervalle d'angulations simulés pouvait caractériser le profil thrombogène du patient. Ces profils reflètent la tendance à l'apparition de complications liées aux DAVG. Les résultats de l'influence du diamètre du ventricule ont montré que pour un VG plutôt petit ou relativement dilaté, le risque de thrombose augmente ce qui est cohérent avec les observations cliniques. Les résultats de l'influence de la longueur de la CA ont montré que le risque de thrombose augmente avec sa longueur, en particulier, lorsque la CA est aussi déviée. Enfin, nous avons confronté les résultats MPTP d'un modèle 2D à un modèle 3D spécifique au patient pour deux configurations. Les résultats préliminaires sur le modèle 3D avaient la même tendance que ceux obtenus avec le modèle 2D.

## Conclusion

Ces travaux de thèse se sont concentrés sur le risque de thrombose associé à l'implantation d'un DAVG pour les patients atteints d'IC. En utilisant le calcul MFN, notre objectif était double : i) mieux comprendre le comportement de plusieurs QI en ce qui concerne l'influence de certaines caractéristiques du CA (longueur et angulation) et ii) développer un marqueur de potentiel thrombogène personnalisé capable d'évaluer le risque de thrombose associé aux caractéristiques du CA, en particulier son angulation.

A notre connaissance, il s'agit du premier travail où le modèle proposé est paramétré avec les données du patient et les données surveillées (rapport anatomique du VG, angulation clinique du CA et le débit de la pompe). Cet aspect personnalisé est accentué avec le MPTP proposé en considérant l'indice de sphéricité ventriculaire pendant les phases diastoliques et systoliques. Ce marqueur absolu a la capacité d'évaluer le risque de thrombose lié à une configuration spécifique sans nécessiter une configuration comparative. Sa définition a le potentiel d'être adaptée à différents niveaux de complexité selon l'intérêt de l'utilisateur (2D, 3D ou 2D-3D).

	0	10	20	30	40	50	60	Average
P1	<b>0.87</b>	0.46	0.74	0.43	<u>0.38</u>	0.61	0.50	0.57
P2	0.53	<b>0.52</b>	0.53	0.54	0.53	0.61	<b>0.67</b>	0.56
P3	0.23	0.26	<u>0.05</u>	0.31	0.32	<b>0.33</b>	0.32	0.26
P4	<u>0.48</u>	0.50	0.57	0.57	<b>0.68</b>	0.66	0.55	0.57
P5	<u>0.45</u>	0.51	0.56	0.57	0.59	<b>0.60</b>	0.59	0.55
P8	<u>0.19</u>	0.20	0.20	0.20	0.23	<b>0.25</b>	0.22	0.21
P9	0.41	0.45	0.42	0.39	<b>0.47</b>	0.47	<u>0.38</u>	0.43
P10	0.68	0.65	<b>0.68</b>	0.62	0.63	0.63	<u>0.51</u>	0.63
P11	0.57	<b>0.68</b>	0.41	<u>0.40</u>	0.41	0.47	0.56	0.49
P12	0.45	0.44	<u>0.40</u>	0.46	0.52	<b>0.64</b>	0.54	0.49
P13	0.67	<b>0.75</b>	<u>0.31</u>	0.39	0.37	0.35	0.36	0.46
P14	0.46	0.44	0.45	<b>0.53</b>	<u>0.40</u>	0.44	0.47	0.46
P15	0.33	<b>0.41</b>	0.35	0.28	0.30	<u>0.21</u>	0.38	0.32
P16	0.37	<b>0.41</b>	0.39	0.38	<u>0.25</u>	0.28	0.32	0.34
P18	0.49	<b>0.60</b>	0.57	0.43	<u>0.34</u>	0.39	0.46	0.47
P19	0.27	0.28	0.24	<u>0.22</u>	<b>0.41</b>	0.26	0.34	0.29
P20	0.30	0.32	0.32	0.35	0.26	<b>0.51</b>	<u>0.25</u>	0.33
P22	0.22	0.21	0.14	0.19	0.22	<u>0.12</u>	<b>0.29</b>	0.20
P23	0.21	0.21	0.22	0.22	0.23	<b>0.24</b>	<u>0.15</u>	0.21

TABLEAU 1 : MPTP : influence de la CA.

Cependant, ce travail présente certaines limites. Comme le nombre de dispositifs implantés reste limité, le nombre de cas cliniques utilisés pour étudier le MPTP est réduit. L'acquisition de plus de données cliniques provenant de plusieurs centres cliniques permettrait de valider le marqueur sur un plus grand nombre de cas. La Valve Aortique (VAo) n'est pas prise en compte et pourrait être représentée dans le modèle 2D. En pratique, les mesures du long diamètre de la VAo de chaque patient ainsi que de la fraction d'éjection associée pourraient être collectées et prises en compte dans les simulations MFN. Il serait intéressant d'analyser l'influence de l'ouverture de la VAo sur l'hémodynamique du VG et son impact sur le MPTP. Une approche 3D du marqueur pourrait également être développée pour approfondir son intérêt. Toutefois, cette approche nécessitera le recours à une infra-structure de calcul plus conséquente tels que un cluster et un Cloud. Il serait également intéressant d'envisager des simulations prenant en compte les battements de cœur. Bien que les patients souffrant de IC aient une contractilité réduite du VG, il reste intéressant de réaliser des simulations de cœur battant, afin d'étudier l'influence des mouvements de la paroi sur les événements de succion et la stagnation du sang, en particulier au niveau de l'apex.

Ce travail est une piste prometteuse vers l'objectif ambitieux de développer un système d'aide à la décision clinique capable de prédire l'angulation optimale de la CA, associée à un risque de thrombose minimal.





# Introduction

Heart Failure (HF) is a long-term condition where the heart muscle is unable to pump blood efficiently, thus, fails to meet the needs of the body in oxygen and nutriment. It may occur when the Left Ventricle (LV) either stiffens and is filled with insufficient amount of blood or weakens and is not able to eject a sufficient amount of blood. This clinical syndrome may appear suddenly (acute) or progressively (chronic). There are 165,000 annual hospitalizations due to HF in France with 45% re-hospitalizations and 29% death within one year (Tuppin et al., 2014).

A Heart Transplant (HT) is required for patients that reached an advanced stage of HF and that are resistant to medical treatment. Due to insufficient donor supply alongside with ineligible patients for HT, Mechanical Circulatory Support (MCS) currently represents the only alternative. These devices could be used to totally replace the heart (Total Artificial Heart (TAH)) or to assist the ventricle (Ventricular Assist Device (VAD)). VAD is an intra-thoracic pump connected to the assisted ventricle through a cannula. As indicated by its name, VAD assists the failing ventricle (left, right or both) to supply a sufficient cardiac output into the corresponding artery. It is composed of an intra-thoracic pump, an Inflow Canula (IC) anastomosed to the ventricle apex, an Outflow Canula (OC) anastomosed to the artery (pulmonary artery / aorta depending on the assisted ventricle) and a drive-line connected to an extra-corporal battery. The most implanted VAD is the Left Ventricular Assist Device (LVAD).

LVAD could be implanted temporarily, as a bridge to transplantation or permanently as a destination therapy, especially for patients that are ineligible for HT. These devices allow a better mobility for patients and enhance their life quality. To date, LVAD implantation rate is growing. However, the incidence of LVAD related complications is also growing as LVAD implanted patients have an admission rate of 64% in emergency department (Tainter et al., 2018). The main LVAD related complications are thromboembolic events such as thrombus formation, pump thrombosis, strokes, .... They are considerable complications as they could significantly impair the health of



the patient, its quality of life and may even be life-threatening.

For LVAD patients, thrombus formation could be triggered by the presence of the foreign material of the IC and the change of flow field distribution that the IC causes within the LV. Depending on IC angulation, the flow field distribution of the blood varies. It is recommended to have an apical implantation of the IC, where the IC is along the LV long axis, facing the Mitral Valve (MV). Nevertheless, this hypothetical ideal IC angulation, is not guaranteed as during LVAD implantation, an IC angulation can occur. A preoperative virtual positioning of the device may reveal that the intra-thoracic space of the patient is not sufficient to implant the LVAD and the surgeon may be constrained to deviate the IC. During the LVAD implantation, the surgeon relies on his professional experience and habits to insert the IC. After placing the pump in the intra-thoracic space and while closing the chest, the IC may deviate at one point of the procedure toward the inter-ventricular septum.

Anecdotal evidence tends to suggest that IC angulation enhances thrombosis, however, this suggestion remain unproved scientifically as thrombus formation is a complex phenomenon. It is associated with coagulation and platelet aggregation which are two intertwined processes that are strongly affected by blood dynamics in ways not fully understood (Carrascal et al., 2017). Due to its complexity, factors involved in thrombus formation can be studied through multiple discipline. Today, the knowledge involving these factors and the way they interact are also not fully grasped, making the thrombosis risk evaluation challenging as it does not have a proper definition yet and remains under investigation. Recent works have investigated the link between IC angulation and thrombosis risk based on Computational Fluid Dynamics (CFD) analysis. They attempted to evaluate thrombosis risk based on platelet activation and blood stagnation. The evaluation of these features differs from one study to another even if they are mainly expressed through shear stress, time exposure and velocity. These investigations were also conducted on limited IC angulations and LV shapes. Obtained results were preliminary and never compared to existent clinical cases.

Developing a marker able to evaluate the thrombosis risk of a patient related to an IC angulation is interesting as it would help to aware the surgeons of an eventual thrombosis risk for postoperative use and help decision makings of the least thrombogenic IC angulation for preoperative use.

The objective of this work is to assess, through CFD computations, the influence of IC features, especially IC angulation, on thrombogenic potential taking into account the influence of LV shape. It aims to develop a Personalised Thrombogenic Potential Marker (PTPM) able to evaluate the thrombogenic potential associated with each IC angulation for specific LV features. It is a first step to the ambitious objective of developing a clinical decision support system able to predict the optimal IC angula-

tion with the least thrombogenic potential. Therefore, user-friendly decision-support methodology with a relatively fast computation and an easy implementation is required.

This PhD dissertation is composed as follows:

**Chapter 1** introduces the clinical context of this dissertation. In this chapter, an overview of the cardiovascular system, heart anatomy and functioning are presented. Then, the heart failure pathology, symptoms as well as diagnosis and associated medical treatments are introduced. Among these treatments, the focus is put on MCS devices and surgical procedures are detailed alongside with post-operative complications, especially thromboembolic events.

**Chapter 2** gives an overview of the state of the art regarding MCS devices related complications, especially LVAD devices. First the impact of the interaction between LVAD implant and the anatomical structure. Afterward, anatomical, mechanical, and fluid constrains are detailed. Gradually the focus is put on research related to LVAD devices generally and IC features (angulation and length) especially. Among these researches, thrombogenic potential related to IC features using CFD simulations is presented. Quantities Of Interest (QOI) and model limitations analysis are carried out. Finally, the positioning of our contribution towards the state of art is highlighted.

**Chapter 3** presents a simplified CFD model to investigate the influence of IC features, especially IC angulation, on the LV haemodynamic. Beforehand the 2D assumption is investigated. Finally, analysis aiming to understand the influence of IC features on LV haemodynamic are carried out.

**Chapter 4** proposes a personalised thrombogenic potential marker able to evaluate the thrombogenic potential related to a specific ventricular shape and IC features. This chapter is a first step to develop a preoperative decision-support methodology able to help clinician to predict the optimal IC angulation with the least the thrombogenic potential.



# Clinical Context

This first chapter introduces the clinical context of Left Ventricular Assist Device (LVAD) implantation. First, the cardiovascular system anatomy and functioning is introduced. Second, the Heart Failure (HF) pathology, diagnosis and treatments are detailed. Then, Mechanical Circulatory Support (MCS) devices are presented. Finally, the surgical procedure of the implantation and associated complications are detailed.

## 1.1 Cardiovascular system

Cardiovascular system supplies body tissues with oxygen and nutriment and removes metabolic wastes. It is composed of a heart and a closed system of vessels. The heart pumps blood and maintains the flow, while vessels carry blood throughout the entire body.

### 1.1.1 Blood circulation

The human body is composed of two circulatory systems: the systemic circulation and the pulmonary circulation. The former connects the heart to the body while the latter connects the heart to the lungs (Figure 1.1).

The systemic circulation is a high-pressure system. It is composed of vessels with several types, diameters, and functions. The arteries are large vessels with thick and elastic walls; they are composed of three layers; their function is to carry oxygenated blood from the heart to the organs. In contrast to the arteries, veins carry deoxygenated blood toward the heart. The blood capillaries are extremely thin and numerous vessels; they connect venules and arterioles; thus, they loop the blood circulation system and ensure the distribution of nutrients and the evacuation of waste products as they interact closely with tissues.

In contrast, the pulmonary circulation is a low-pressure system, where arteries carry deoxygenated blood away from the heart and veins carry oxygenated blood toward the heart.

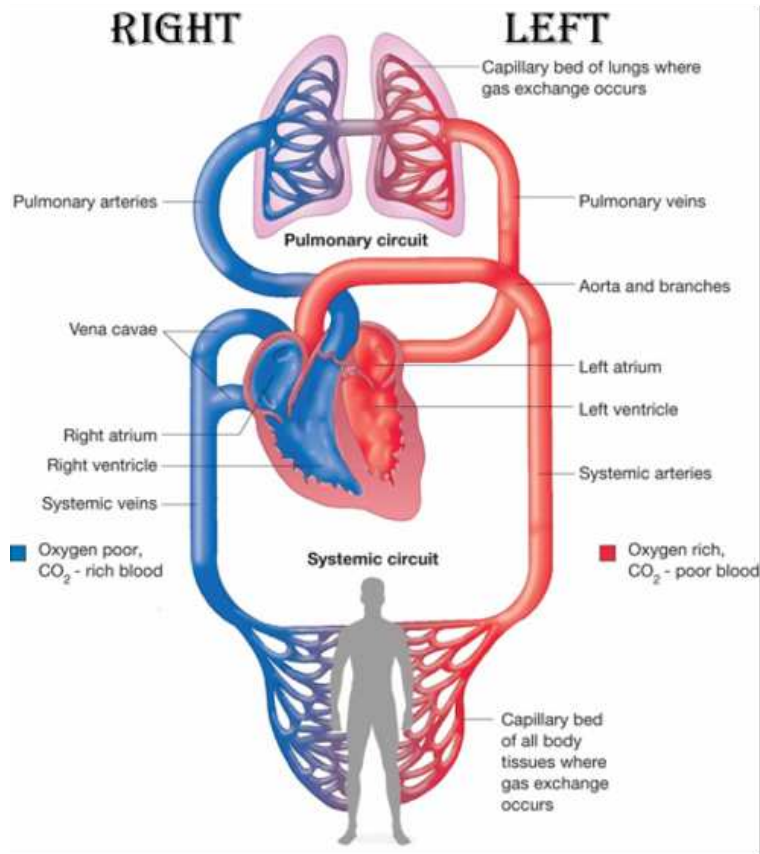


Figure 1.1: Blood circulation.

### 1.1.2 Heart anatomy

The heart is lodged in the thoracic region (chest). It is located on the lungs median line known as the mediastinum, slightly offset to the left so that two thirds of its mass is located on the left side. This is the normal position known as levocardia. Congenital heart defect can place it on the right side (dextrocardia) or in the middle (mesocardia). The heart is contained within the pericardial cavity and is surrounded by the lungs, the thoracic diaphragm at the bottom, the sternum at the front, the oesophagus at the back and the arterial trunks (aorta and pulmonary artery) at the top (Figure 1.2).

The heart is a muscle shaped as an upside-down triangular pyramid with its top oriented in anterior-inferior direction. It is divided by four chambers separated by two main grooves composed mainly of fat and main branches of the coronary vessels. Inter-ventricular grooves are composed of the anterior and posterior inter-ventricular sulci. They separate the left side of the heart from the right side. They run vertically

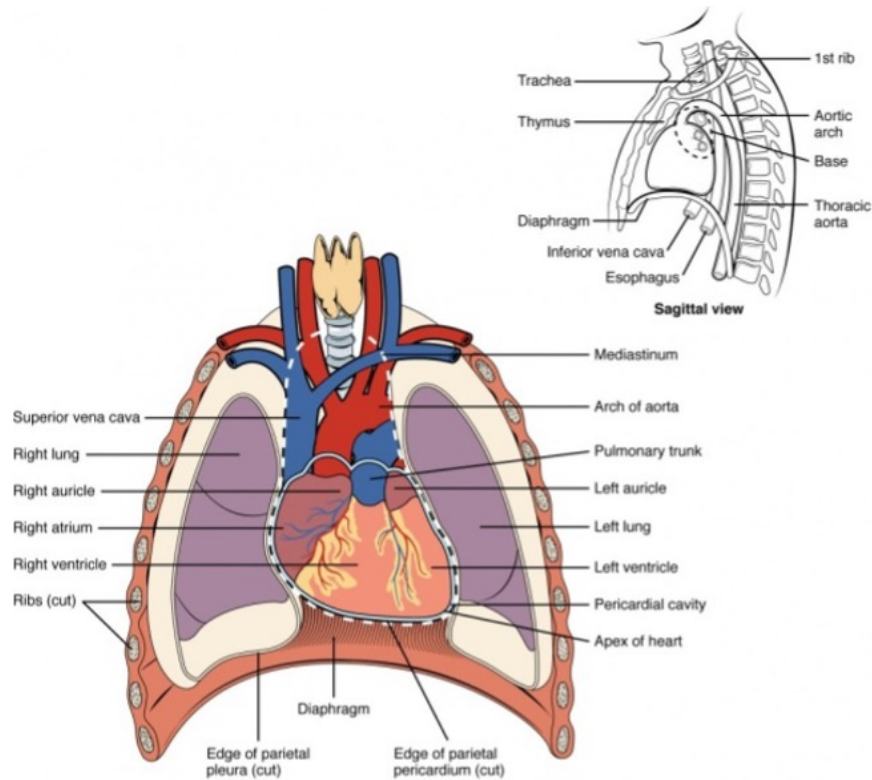


Figure 1.2: Heart Location.

from the anterior to the posterior surface of the heart. The anterior inter-ventricular sulcus holds the anterior inter-ventricular artery and the great cardiac vein while the posterior inter-ventricular sulcus holds the posterior inter-ventricular artery and the middle cardiac vein. The atrioventricular groove also known as the coronary sulcus is perpendicular to the inter-ventricular grooves as it runs transversely circling the heart. It separates the atria from the ventricles and holds the right coronary artery, the small cardiac vein, the coronary sinus, and the circumflex branch of the left coronary artery (Figure 1.3).

The left side of the heart is unequally divided to a small upper part called the atrium and a larger lower part called the ventricle (Figure 1.4). It is in charge of the systemic circulation. Oxygenated blood derived from the lungs fills the atrium through the pulmonary vein. Once full, the atrium transfers the oxygenated blood to the left ventricle through the Mitral Valve (MV) then it is distributed to the whole-body tissues through the aorta. The right side of the heart has the same architecture as the left side. It is in charge of the pulmonary circulation. The venous blood derived from the body tissues fills the atrium through the vena cava. Once full, the atrium transfers the venous blood to the Right Ventricle (RV) through the tricuspid valve. Then, the RV distributes it to the lungs through the pulmonary artery. Valves ensure that the blood circulate in one way, preventing thus, blood regurgitation.

The heart wall can be divided into three different layers:

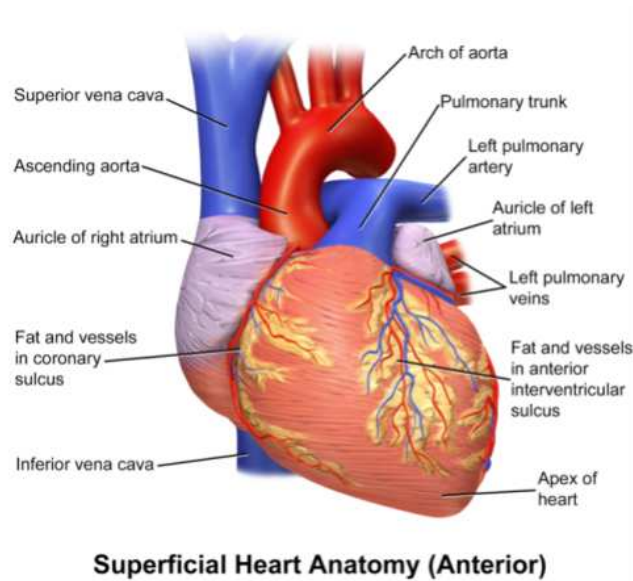


Figure 1.3: Superficial heart anatomy (Anterior).

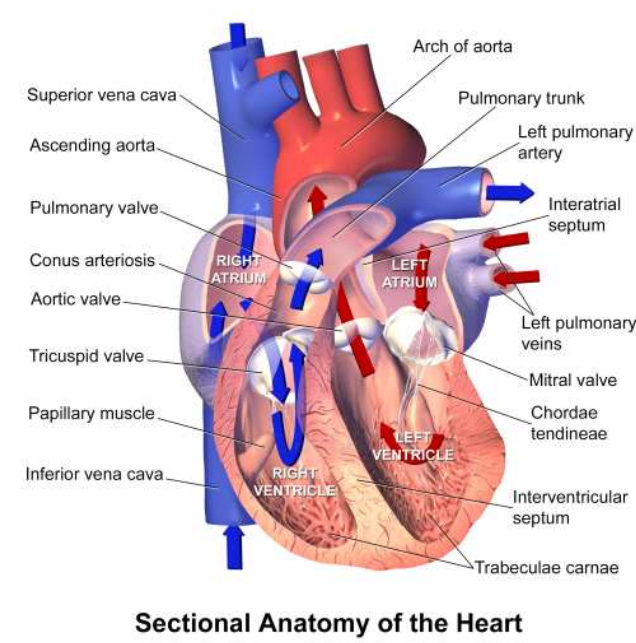


Figure 1.4: Heart anatomy and circulation.

- Endocardium is the inner layer of cardiac wall. It is a thin membrane composed of endothelial cells providing a non-adherent surface favouring the collection of blood. Its function consists in regulating the myocardial contractility.
- Epicardium is the outer layer of cardiac wall. It is a non-muscular thin membrane composed of fibrous tissue and fat providing an extra layer to protect the heart from trauma or friction as the fibrous tissue secretes lubricating fluid into the pericardial cavity in small amount.
- Myocardium is the middle layer of cardiac wall. It is a dense membrane com-

posed of striated muscle assuring the heart contractility. The myocardium thickness varies depending on its location. Indeed, the ventricles myocardia are thicker than those of the atria, and the left ventricle myocardium is thicker than the one of the right ventricle.

### 1.1.3 Heart functioning

The heart is composed of two independent pumps (right and left sides) working simultaneously. The pumping is provided by the coupling of mechanical and electrical phenomena. It is best illustrated by the alternation of clenching (myocardial contraction) and loosening (myocardial relaxation) a fist. Each beat, the heart pushes blood through the arteries. This creates the pulse.

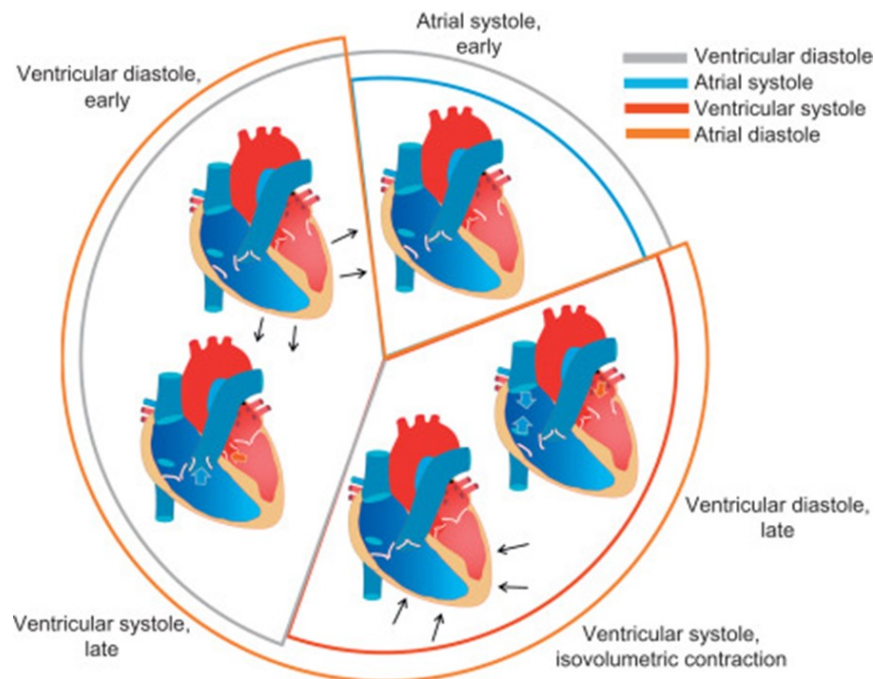


Figure 1.5: Cardiac cycle.<sup>1</sup>

A heartbeat is clinically composed two main phases (Figure 1.5):

- **Diastolic phase:** it is a phase where the heart is relaxed. In the right side of the heart, venous blood returns to the right atrium through superior and inferior vena cave. Blood filling increases the pressure within the right atrium till it exceeds the pressure of the right ventricle which opens the tricuspid valve and blood flows to the right ventricle. In the left side of the heart, oxygenated blood returns to the left atrium through the left pulmonary veins. When the pressure in the left atrium exceeds the pressure in the left ventricle, the mitral valve opens and blood flows to the left ventricle.

1. Source (Fotiadis and Athanasiou, 2017)



- **Systolic phase:** it is a phase where the heart contracts. The two atria contract to complete the filling of the ventricles by ejecting any remaining blood. Once both ventricles are filled, the atrioventricular valves (mitral and tricuspid valves) close and the ventricles begin their contractions. As for atria, when the ventricular pressure exceeds the pressures within the arteries (left pulmonary and ascending arteries), the semi-lunar valves (pulmonary and aortic valves) open and blood is ejected from the ventricles. Then, ventricles relax, and a new diastolic phase begins.

A mechanical interpretation of a heartbeat focuses on instantaneous ventricular Pressure and Volume (P-V) loop. It is a time independent representation composed of four phases (Figure 1.6):

- **Phase I** is the ventricular filling (a). The 1 point on the P-V loop marks the end of the diastolic phase. The pressure and volume at the end of ventricular filling are known as, the End Diastolic Pressure (EDP) and the End Diastolic Volume (EDV), respectively.
- **Phase II** is an isovolumetric contraction (b). Atrio-ventricular valves close; the ventricles contract while the blood volume remains unchanged (semi-lunar valves are already closed) resulting in an increased ventricular pressure represented by a vertical line in the P-V diagram. Once the pressure within the ventricles exceeds arterial pressure, semi-lunar valves open (point 2).
- **Phase III** is the ejection phase (c). The semi-lunar valves opening result in a ventricular volume decrease as the ventricular pressure increases till it reaches a peak known as systolic pressure peak then ventricular pressure starts to decrease as the ventricles start to relax. Once the ventricular pressure falls below arterial pressure, semi-lunar valves close (point 3).
- **Phase IV** is an isovolumetric relaxation (d). As ejection ends, isovolumetric ventricular relaxation begins where the ventricular pressure decreases while the ventricular volume remains the same (all valves are closed). It is represented in the P-V diagram by a vertical line. When the ventricular pressure falls below atrial pressure, the atrioventricular valves open and ventricular filling begins (point 4). At this point, ventricular volume is the End-Systolic Volume (ESV). Ventricular pressure continues to decrease as the ventricles are being filled since they are still relaxing. Once ventricles complete their relaxation, ventricular pressure increases gradually as ventricular volume increases. The Stroke Volume (SV) is the difference between EDV and ESV.

Heart contractions are ensured by an electrical activity provided by myocardial cells. A heartbeat can be electrically described by a specialised conduction pathway composed of five elements (Figure 1.7).

The SinoAtrial (SA) node is the natural pacemaker of the heart. According to the heart needs, it releases electrical stimuli that instantaneously spread to both atria

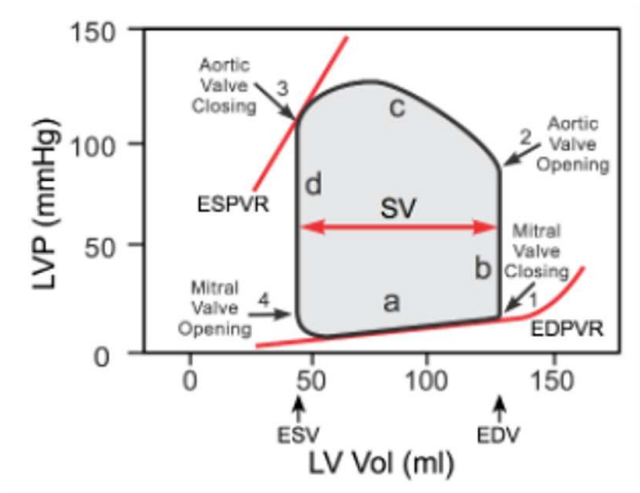


Figure 1.6: P-V Loop of cardiac cycle.<sup>2</sup>

causing their contraction. Once the SA stimulus reaches the AtrioVentricular (AV) node, a brief delay is performed till the MV and tricuspid valve close. Then the electrical stimulus travel through the AV node and Bundle of His into the Bundle branches and Purkinje fibres to contract the ventricles.

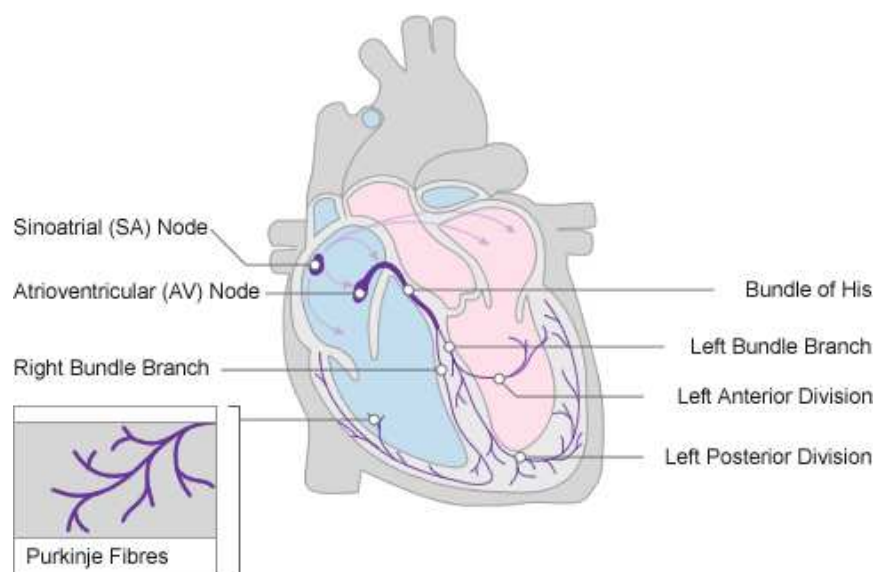


Figure 1.7: Cardiac conduction system.<sup>3</sup>

This electrical activity can be observed in an ElectroCardioGram (ECG) as a PQRST wave (Figure 1.8). The P wave is a depolarisation wave representing the spread of the SA node stimuli to atria. The time taking the stimulus to reach the AV node and Bundle of His is represented by a brief isoelectric (0V) period. The PR interval represents the time between the beginning of atrial depolarisation and the beginning of ventricular depolarisation (QRS complex). The ST segment is an isoelectric period

2. Source (Klabunde, 2017)

3. Source (School of Health Sciences, 2009)

that represents the period of time when the ventricles are completely depolarised. The T wave represents ventricular repolarisation. It is a positive deflection as the last cells to depolarise are the first ones to repolarise. The time for both ventricular depolarisation and repolarisation corresponds to the QT interval.

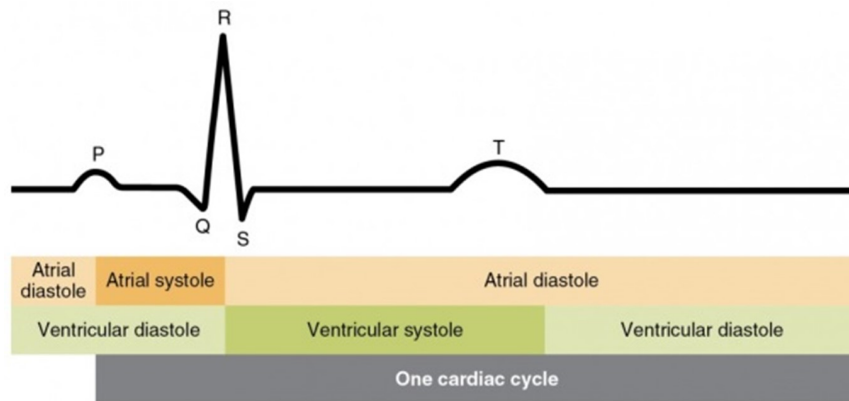


Figure 1.8: PQRST wave.<sup>4</sup>

A heart beat is the coupling of the electrical and mechanical activities of the heart (Figure 1.9). Any abnormality in the electrical activity may impact the mechanical activity and vice versa. Cardiac functioning is also closely related to the arteries behaviour. The occurrence of an abnormality at any level may cause CardioVascular Diseases (CVDs) that may lead, overtime, to heart failure.

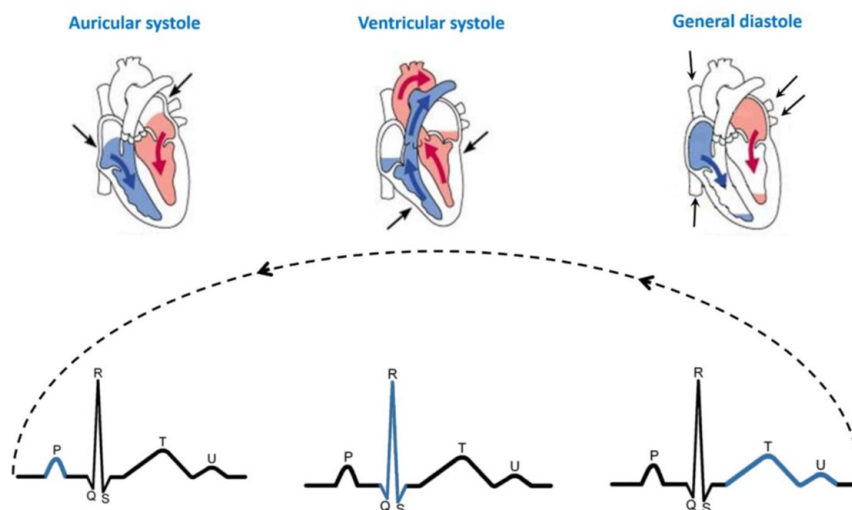
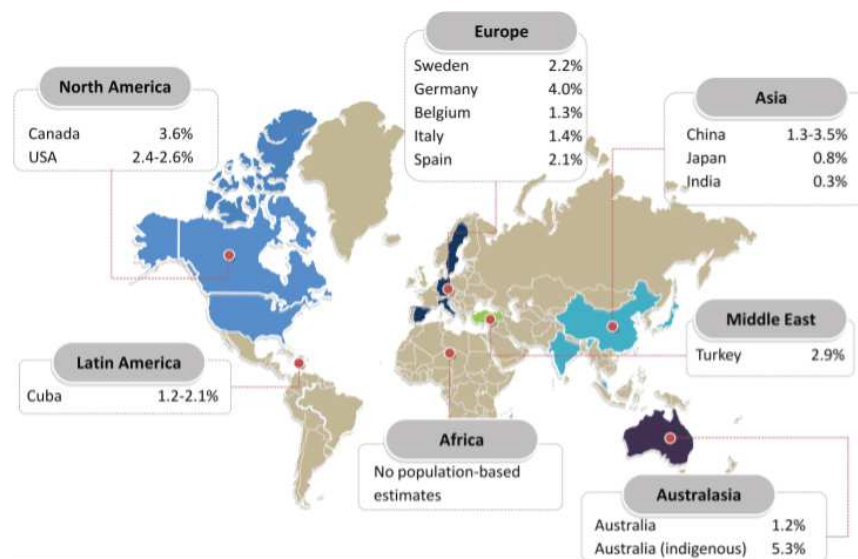


Figure 1.9: Heart beat: electrical/mechanical coupling.

4. Source (Lumen Learning, 2015)

## 1.2 Heart Failure

HF means that the heart fails to meet the needs of the body (oxygen, nutrients ...) preventing it from functioning properly. It is a chronic and progressive clinical syndrome caused by functional or structural defect in myocardium. It may result in impairing ventricular filling or ejection of the blood (Inamdar and Inamdar, 2016). HF is mainly an elderly disease; however, recent studies have pointed out that the HF burden in young people may increase (Groenewegen et al., 2020). Available data on worldwide prevalence is shown in Figure 1.10.



**Figure 1.10:** Prevalence of heart failure in population-based studies around the world, in percentage, per region.<sup>5</sup>

### 1.2.1 Pathology and symptoms

When the heart is unable to supply enough blood to the body, as a first measure, it tries to compensate by:

- Pumping faster in order to increase the cardiac output.
- Enlarging the concerned cavity (stretch) in order to contract more strongly to keep up with the pumping blood demands. Over time the heart becomes enlarged.
- Developing muscular mass as the myocardial cells get bigger. It helps the cavity to pump more strongly, at least initially.

More indirect ways are attempted to meet the body requirement such as narrowing the blood vessels to maintain the blood pressure up and vital selection, where the

<sup>5</sup> Source (Groenewegen et al., 2020)

body diverts blood away from non-vital tissues and organs. However, these temporary measures hide the HF symptoms without curing it. The HF condition continues and worsens till the efficiency of these compensating processes ceases and symptoms (fatigue and shortness of breath) appear. These mechanisms are the reason why HF is diagnosed only after the heart has already begun its declining.

HF patients suffer from an impaired life quality, especially when the symptoms are untreated which may increase clinical events (emergency department visits, hospitalisations, long term mortality...) which may impact these patients not only physically but also emotionally, socially and in the spiritual aspects of suffering (Alpert et al., 2017).

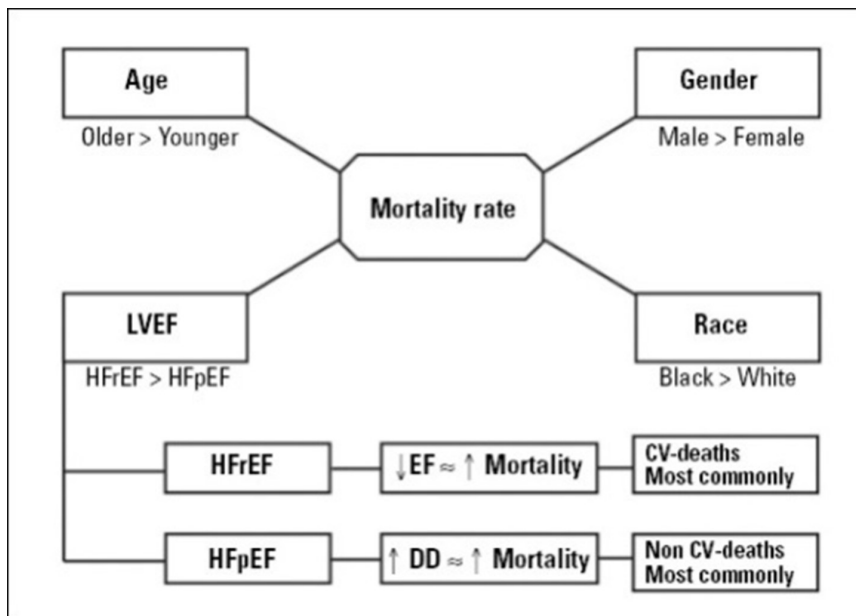


Figure 1.11: Differences in mortality rate of heart failure patients according to age, gender, race and condition. CV - Cardio-Vascular; DD - Diastolic Dysfunction; EF - Ejection Fraction.<sup>6</sup>

Many Conditions may lead to HF. Two major risk factors are Coronary disease and high blood pressure (Velagaleti and Vasani, 2007). The first one may damage the heart muscles in case of “heart attack” or may also contribute to a high blood pressure. The latter pushes the heart to pump harder than what it is supposed to in order to ensure blood circulation. This will damage the heart, and over time weakens and enlarges the chambers. Other leading conditions such as cardiomyopathy (heart muscle disease) or myocarditis (heart muscle inflammation), abnormal heart valves, arrhythmia (irregular heart rhythm or rate), congenital heart disease, viral infection, etc. (Dickstein et al., 2008). Other factors may promote the heart failing as obesity, high cholesterol, diabetes, alcohol, or smoking.

HF can involve the Left Ventricle (LV), the RV or both, but usually, the LV is affected first and may cause afterwards a right sided HF. Left Ventricle Heart Failure (LVHF)

6. Source (Bytyçi and Bajraktari, 2015)

NYHA Class	Description of HF Related Symptoms
I (Mild)	Patients with cardiac disease but without resulting in limitation of physical activity. Ordinary physical activity does not cause undue fatigue, palpitation (rapid or pounding heartbeat), dyspnoea (shortness of breath), or anginal pain (chest pain).
II (Mild)	Patients with cardiac disease resulting in slight limitation of physical activity. They are comfortable at rest. Ordinary physical activity results in fatigue, palpitation, dyspnoea, or anginal pain.
III (Moderate)	Patients with cardiac disease resulting in marked limitation of physical activity. They are comfortable at rest. Less than ordinary activity causes fatigue, palpitation, dyspnoea, or anginal pain.
IV (Severe)	Patients with cardiac disease resulting in the inability to carry on any physical activity without discomfort. Symptoms of heart failure or the anginal syndrome may be present even at rest. If any physical activity is undertaken, discomfort is increased.

**Table 1.1:** NYHA functional Classification.<sup>7</sup>

increases the transferred blood pressure to the lungs, ultimately damaging the right side of the heart. When the right ventricle fails to pump, blood regurgitates to the veins causing swelling in the legs, ankles or within the abdomen.

There are two types of HF:

- HF with reduced Ejection Fraction (HFrEF) or systolic heart failure. The LV is dilated which reduces its contracting ability to push enough blood into the body. Most of HF patients are with reduced ejection fraction.
- HF with preserved Ejection Fraction (HFpEF) or diastolic heart failure. The LV has become stiff which reduces its relaxing ability preventing it from properly being filled with blood.

### 1.2.2 Diagnosis and treatments

The mortality rate of HF patients differs according to age, gender, race and condition (Figure 1.11). Overall, the survival rates after one, five and ten years of being diagnosed with HF increased by 6.6% (from 72.2% in 2000 to 80.8% in 2016), 7.2% (from 41% in 2000 to 48.2% in 2012) and 6.4% (from 19.8% in 2000 to 26.2% in 2007) respectively (Taylor et al., 2019). Thus, it is important to be diagnosed at an early stage.

Clinical assessment of HF is made from clinical history and physical examination results. They include the presence of clinical symptoms, signs and blood tests such as a complete blood count, urinalysis, complete metabolic profile, glucose, fasting lipid profile, liver function tests and thyroid-stimulating hormones (Inamdar and Inam-

7. Source (Little, 1994)

Stage	Objective assessment
A	Presence of heart failure risk factors but no heart disease and no symptoms
B	Heart disease is present but there are no symptoms (structural changes in heart before symptoms occur)
C	Structural heart disease is present AND symptoms have occurred
D	Presence of advanced heart disease with continued heart failure symptoms requiring aggressive medical therapy

**Table 1.2:** American Heart Association Heart Failure Stages.<sup>8</sup>

dar, 2016). To confirm HF presumption, further investigations are done (Inamdar and Inamdar, 2016; Taylor et al., 2017):

- Chest X-ray: evaluate heart size, pulmonary congestion or other cardio-pulmonary diseases that may be related to the patient symptoms.
- TransThoracic Echocardiography (TTE): assess ventricular and atrial functions, sizes, walls thickness and motions, valves functions and Ejection Fraction (EF). It is a tool that helps in defining the appropriate therapy.
- Magnetic Resonance Imaging (MRI): as for echocardiography, it assesses EF and ventricular volume, but it also provides additional information about myocardial perfusion, viability, and fibrosis helpful for HF etiology identification and prognosis assessment.
- Computerized Tomography (CT): accurate assess of cardiac structure and function as well as coronary arteries. Nevertheless, MRI and CT are inaccurate for patients with high heart rates.
- Cardiac catheterization and coronary angiography: necessary for new HF onset and angina symptoms patients.
- ECG: records heart beats and detects abnormalities (atrial fibrillation) or irregularities.
- HF-specific laboratory tests: to detect bio-markers. They provide valuable information on the cause, the presence, and the severity of the ongoing disease.

The HF of a patient is classified based on the pathology symptoms and functional limitations. Its severity depends on the ability of the failing heart to pump blood. The most common classification of the HF severity is based on the New York Heart Association (NYHA) Class guidelines (Table 1.1). Later, a rating system evaluating the progress of the pathology symptoms was developed by the American Heart Association and American College of Cardiology. The grades describe the patient conditions as the HF progresses (Table 1.2).

For refractory or terminal HF (class III-IV), end stage or congestive HF terms are employed. Once these final stages are reached, they are stratified according to The

8. Source (Yancy et al., 2013)

Interagency registry for Mechanically Assisted Circulatory Support (INTERMACS) classification (Figure 1.12) where profile 7 represents a less advanced stage of congestive HF (included in class III) while profile 1 represents a refractory cardiogenic shock (part of class IV).

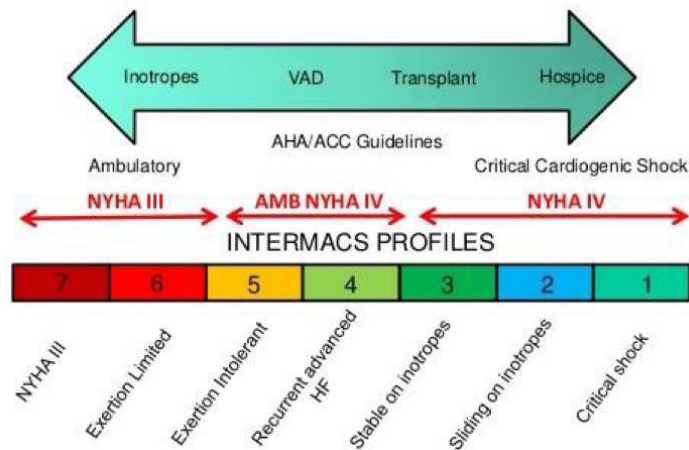


Figure 1.12: INTERMACS classification system compared to NYHA classification.<sup>9</sup>

As HF damages the heart and is usually diagnosed at an advanced stage, for most cases, it cannot be cured. The aims of HF therapy are to:

- Reduce symptoms and improve life quality;
- Slow the pathology progression;
- Reduce emergency and hospitalization rate;
- Increase patients' lifespan.

The treatment choice depends on the type, cause, symptoms, and severity of the pathology. Usually, many treatments are used at once. Since HF results from underlying conditions (coronary disease, diabetes, anaemia, arrhythmia, ...), treating these factors is essential. Treatment also involves lifestyle change such as weight loss, healthy diet low in salt and fat, limitation or interdiction of alcohol consumption, quit smoking and avoid exposure to second-hand smoke, avoid caffeine intake, reduce daily activities in order to avoid stressing the heart; however once the symptoms are stable, a physical rehabilitation program might be recommended. For medication treatment, several classes are available depending on whether the heart requires being strengthened or relaxed. It improves the functioning of the heart muscle by controlling the blood pressure and the heart pumping. Unfortunately, sometimes these treatments might not be sufficient, and a surgical procedure might be required. Depending on the clinical condition, several procedures may be performed (Agnetti et al., 2015; Walter and Hetzer, 2013):

- Coronary Revascularization: It restores the blood flow into the coronary arteries by withdrawing a vein or an artery from another part of the body (leg, arm,

9. Source (Peta, 2018)



or chest) and uses it as a bypass in order to improve the blood flow beyond the coronary stenosis.

- Mitral Valve repair/ replacement: MV might be repaired by removing calcification, extra tissue, fixing the cords or reattaching them. If the valve repair is not possible, it is generally replaced by a mechanical or biological prosthetic. The valve replacement can be performed by an open-heart surgery, a minimally invasive surgery or a cardiac catheterization.
- Ventricular reconstruction: the purpose of this surgery is to reshape the dilated ventricle from its elliptical shape to a spherical shape in order to improve its functioning. It is usually performed with coronary revascularization operation or MV repair.
- Intra-Cardiac Device (ICD) implantation: these devices deliver electrical stimulations to monitor the heart pulse enabling it to pump blood more efficiently. The most known devices are pacemakers (speed the heart rate) and defibrillators (control heart rhythm especially if it reaches dangerous ranges). Defibrillators could also be used as a pacemaker.
- Heart transplant: it consists in replacing the failing heart with a healthy one (donor).
- MCS devices implantation: these devices are implanted into the chest or abdomen of the patient to assist the heart into pumping blood efficiently. Once the end-stage of HF is reached and no alternative treatments are possible, MCS devices are used for patients in need of a Heart Transplant (HT). These patients could be in the waiting list or ineligible for heart transplantation.

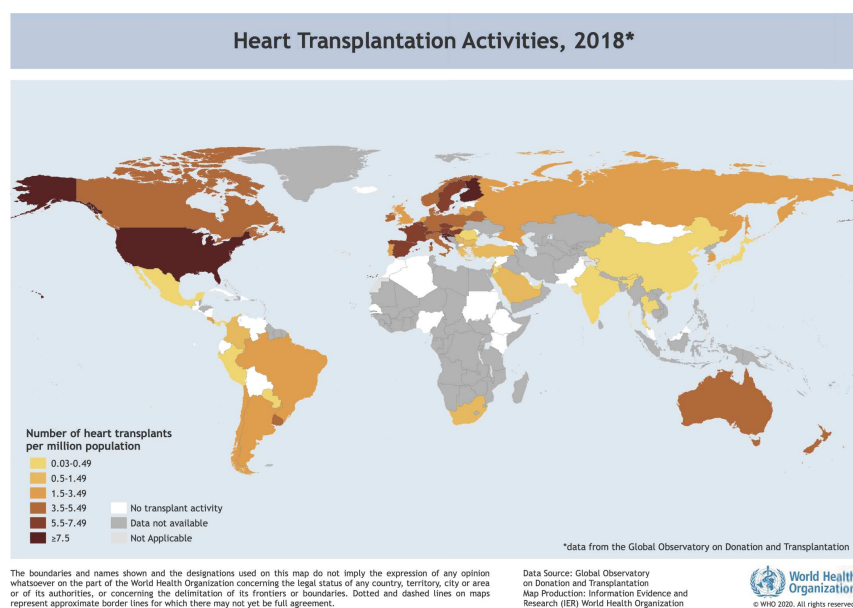


Figure 1.13: Heart transplant Activities in 2018. <sup>10</sup>

10. Source (European Directorate for the Quality of Medicines and Healthcare (EDQM), 2020)

### 1.2.3 End-stage heart failure

The first human HT was performed in 1967 in South Africa with 18 days survival (Brink and Hassoulas, 2009). According to Global Observatory on Donation and Transplantation (GODT), there were 2269 HT in Europe in 2019 and 8311 HT globally in 2018; Figure 1.13 presents the HT activity in 2018 worldwide. Between 2011 and 2013, adults who underwent HT have a 1-year survival rate of 90.3%, a 3-year survival rate of 84.7% and a 5-year survival rate of 79.6% (Colvin et al., 2020).

According to the International Society of heart and Lung Transplant (ISHLT), the number of HT has increased over this century (Figure 1.14). However, it is greatly outweighed by the increase of the waiting list candidates as shown in Figure 1.15. where, the number of candidates was calculated by adding the patients remaining on the waiting list on January 1 of each year with the new registered ones, then by subtracting deaths and those who left the waiting list during the year.

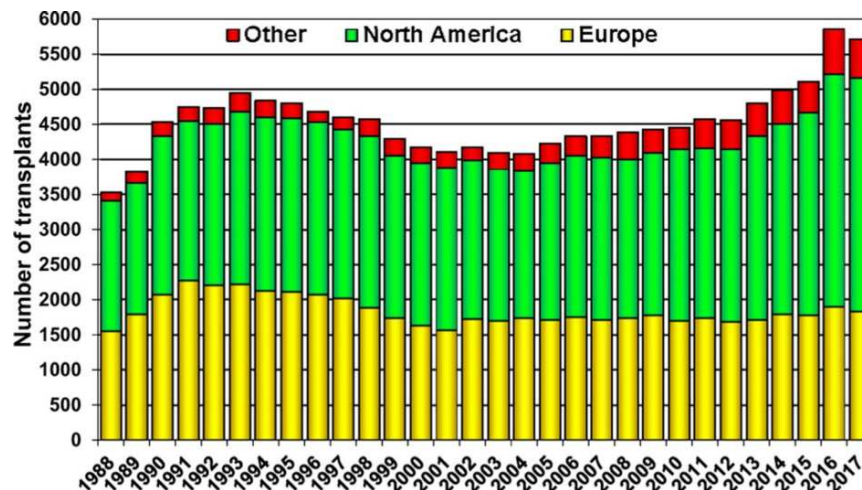
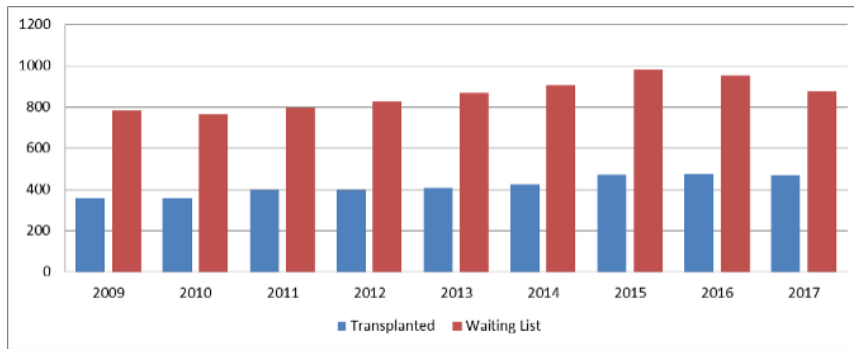


Figure 1.14: Number of heart transplants (adult and pediatric) by year (transplants: 1988–2017) and geographic region.<sup>11</sup>

Facing the graft shortage, the implantation of MCS devices remain the only alternative to HT. As technologies advance steadily, these devices have known a significant improve increasing their use in recent years as they allow patients to wait longer for transplantation. One category of MCS devices is Ventricular Assist Device (VAD) which will be discussed in more details in the following paragraphs. According to the annual data report: heart (2018) of the American Society of Transplant Surgeons (ASTS), the rate of VAD patients on the waiting list, has increased from 11.8% in 2008 to 32.6% in 2018. Between 2013 and 2018, 43.6% of patients receiving any life support prior transplant had a Left Ventricular Assist Device (LVAD) (Colvin et al., 2020). LVAD have aroused a lot of interest and have been proven to be a sustainable alternative to HT.

11. Source (Khush et al., 2019)



**Figure 1.15:** Number of waiting list candidates compared to the number of trans-plantations by year, in France.<sup>12</sup>

### 1.3 Mechanical Circulatory Support (MCS) devices

MCS devices are cardiac pumps that give mechanical assistance to replace partially or totally a failing heart or lungs. They consist of (Figure 1.16):

- Pumping chamber: it replaces or assists the failing ventricle(s) by pumping blood
- External controller: it is connected to the pumping chamber via a drive-line. The controller runs the device and controls operating parameters (alarms, speed, ...). It can be pneumatic or electronic.
- Power supply: it supplies energy to the device. The energy may be pneumatic, hydraulic, electric, or electromagnetic.

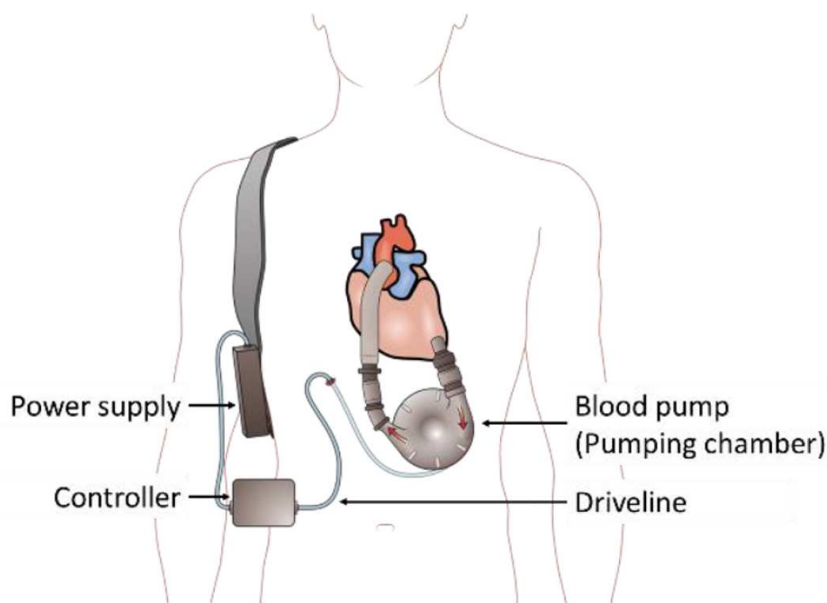


**Figure 1.16:** Mechanical circulatory support components; example of left ventricular assist device.

12. Source (Agence de la biomédecine 2017 : Greffe cardiaque)

MCS devices have four different functions (Stewart and Givertz, 2012):

- Bridge To Transplant (BTT): when the failing heart reaches the last stage and the patient is still waiting for a graft. The device is implanted temporarily to stabilize and maintain the patient condition in order to remain eligible for HT. This strategy may also be used to improve the health of an ineligible patient in order to become eligible.
- Bridge To Recovery (BTR): it is a strategy used rarely when the ventricle, once supported by the VAD for a period of time, is likely to recover and becomes able to function efficiently with only medications. The VAD is then explanted if the pump design allows it, otherwise the pump is deactivated which presents a controversial issue among clinicians and institutions as it may promote important complications.
- Destination Therapy (DT): when the patient is ineligible for HT (age older than 70 years or inadequate health conditions) (Flécher, 2014). The only remaining alternative is to support the failing heart using MCS devices. In these cases, the device is implanted permanently.
- Bridge to Decision (BTD): the device is implanted temporarily till the clinicians decide of a definitive treatment strategy.

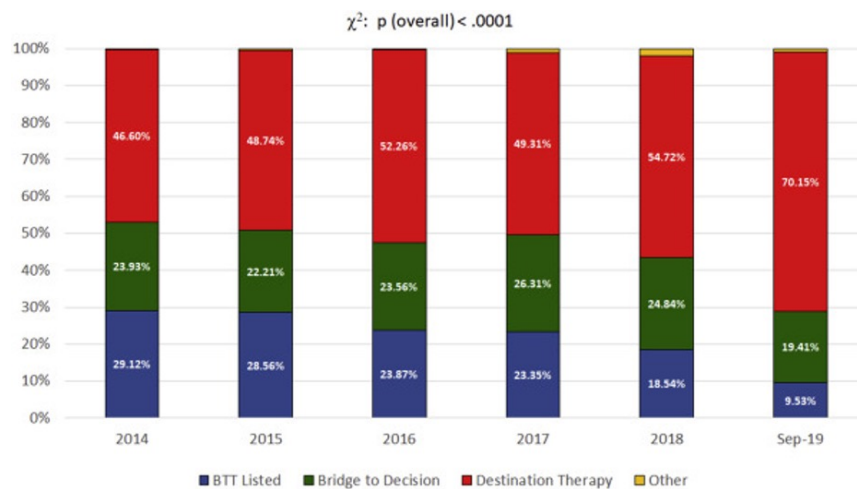


Figure 1.17: Implant strategies by year.<sup>13</sup>

MCS are mostly used as DT, a use that is increasing every year, since they represent the only alternative to HT for non-eligible candidates (Figure 1.17). Thanks to MCS devices, 79% of DT patients had their condition improved from NYHA class III or IV to class I or II within 24 months (Rogers et al., 2010).

Depending on the heart condition, MCS can be divided into two categories: Total Artificial Heart (TAH) and Ventricular Assist Device (VAD). TAH is a transplantation

13. Source (Teuteberg et al., 2020)

of a mechanical heart able to fulfil the heart native functions. While TAH require the removal of the failing heart, VADs are cannulated to the failing ventricle in order to assist its functioning.

MCS devices could also be divided into long-term mechanical support and short-term mechanical support (days or few weeks). As examples of short-term MCS devices, one can cite: extra-corporeal membrane oxygenation, intra-aortic balloon pump, Impella device, Tandem heart, . . . They are, however, beyond the scope of this thesis.

### 1.3.1 Total Artificial Heart (TAH)

TAH pump is a prosthetic heart that is bio-compatible as its external wall is made of titanium, plastic or ceramic. The pump is intra-thoracic, and it replaces the lower native chambers of the heart (RV and LV). These artificial ventricles can be fixed or independent from each other (Figure 1.18). Each is composed of two mechanical valves: an inflow and an outflow valves. They control the blood flow direction: in and out of the ventricle respectively and connect the artificial ventricle to the native heart atrium and the corresponding artery (pulmonary artery for RV and aorta for LV). The monitor-driven pumping system can be hydraulic or pneumatic. Once the TAH is connected, the heart action is duplicated which restores normal blood flow through the body.

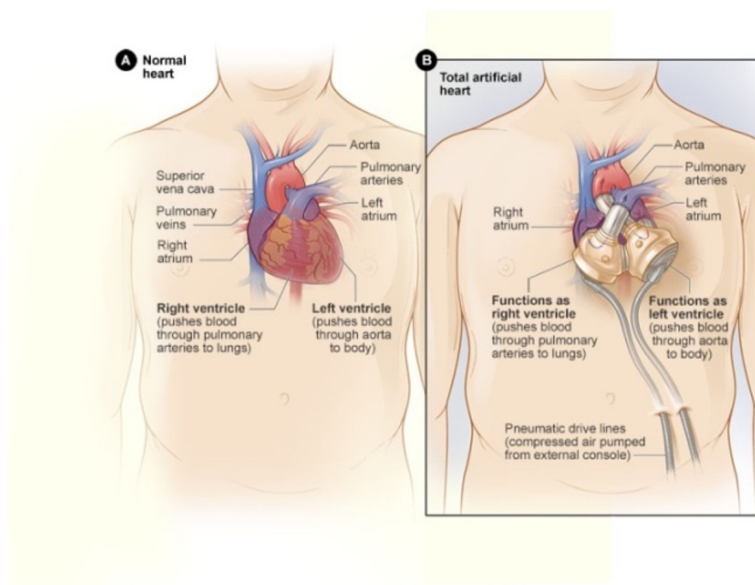


**Figure 1.18:** Normal structure and location of the heart (A) vs total artificial heart, including the tubes that exit the body and connect to a machine that powers and controls the total artificial heart (B).<sup>14</sup>

The first attempt to implant a TAH was performed into an animal (dog) in 1957 with a 90 minutes survival by Kloff and Akutsu (Akutsu and Kolff, 1958). This marked the beginning of the developing of a TAH fully implantable for long-term support

14. Source (National Heart, Lung, and Blood Institute (NHLBI), 2022)

as HT was not a conceivable solution yet. Later, in 1969 occurred the first in-human TAH transplantation (Liotta-Cooley heart) as a BTT at the Texas Heart Institute for 64 hours. Nevertheless, the Liotta-Cooley heart did not receive the approval of the Food and Drug Administration (FDA). Over the years, several artificial hearts have been developed (Cohn et al., 2015; Sunagawa et al., 2016). Recently, a french TAH, CARMAT received FDA approval and was performed its first human implant on July 2021 in the United State. Appendix A presents the nine principal TAH developed. Four did not receive FDA approval, three received it and two future prototypes.

### 1.3.2 Ventricular Assist Devices (VAD)

As the name suggests, VADs are devices that assist the ventricle(s) when failing. They can assist the RV (Right Ventricular Assist Device (RVAD)), the LV (LVAD) or both (Bi-Ventricular Assist Device (BiVAD)). For mono-ventricular assistance, the device is composed of a pump, an Inflow Canula (IC) for the blood inlet, an Outflow Canula (OC) for blood outlet and a drive-line (Figure 1.19). The IC is anastomosed directly to the atrium or at to the ventricular apex while the OC is commonly anastomosed to the main artery of the failing ventricle (pulmonary artery /Aorta). The Bi-ventricular device is a combination of a RVAD and a LVAD.

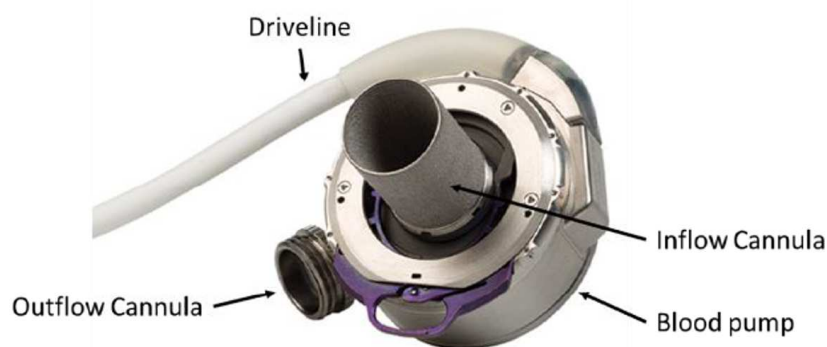


**Figure 1.19:** Ventricular assist device pump: example of left ventricular assist device (HeartMate 3 - Thoratec Inc., pleasanton, CA).

VADs can be divided into three categories as shown in Figure 1.20 (Cuttone et al., 2011)

- Extra-corporeal pump: the pump is external to the body. The blood inlet and outlet are performed via long IC and OC tubes respectively. This device may be connected to an oxygenator.
- Para-corporeal pump: the pump is also external to the body, but the IC and OC tubes are short resulting in a device being in contact with the patient.
- Intra-corporeal pump: the pump is placed in the body (inside the thorax) near the heart. It is also known as intra-thoracic pump.

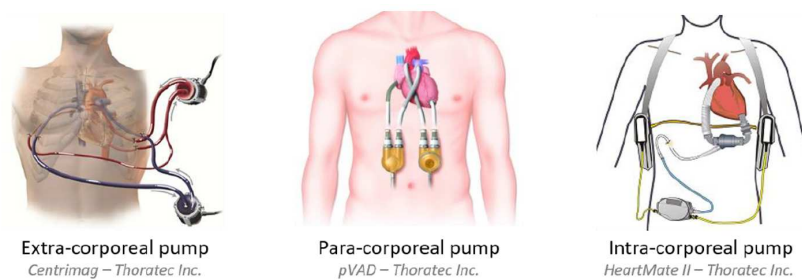


**Figure 1.20:** Ventricular assist devices categories.

The first VAD implantation was in 1966 by Dr. DeBakey. It was a para-corporeal LVAD developed by the Rice-Baylor group (Chair et al., 2016; Hall et al., 1967). As time passed by, VADs have evolved and are classified into three generations. The First generation VADs have two mechanical valves and a pumping action similar to the heart. Indeed, the heart movement is mimicked by a cyclically pressurized sac. The applied pressure may be electrical or pneumatic. These pumps are referred to as Pulsatile-Flow VADs (PFVAD). However, the second and third generations of VADs no longer attempt to mimic the heart functioning and have rotary pumps that produce Continuous-Flow VAD (CFVAD) that increases blood flow and pressure via a rotating impeller. The second generation VADs have mechanical bearing impellers and the pump flow could be axial or centrifugal. The third generation VADs have suspended (hydrodynamic or magnetic levitation) bearing impellers which considerably reduces friction. Some examples of VADs for every generation are presented in Appendix B.

## 1.4 MCS implantation

### 1.4.1 Implantation criteria

Several factors (age, body size, symptoms, and medical condition) have to be taken into account for a patient to be considered as a candidate for MCS device implantation. The current recommendation for patient selection to MCS device implantation are (Wilson et al., 2009) :

- Refractory end-stage ventricular HF (NYHA Class IV)
- Life expectancy inferior to 2 years (for DT only)
- Not a candidate for HT (for DT only)
- Failed to respond to medical management
- Ejection fraction inferior to 25%
- Functional limitation with a peak oxygen consumption (also called Maximal Oxygen uptake  $\text{VO}_2 \text{ max}$ ) equal or inferior to  $14 \text{ ml.kg}^{-1}.\text{min}^{-1}$

Medical therapy has shown to be more efficient than CFVAD implantation on patients with HF classified III NYHA. Indeed, the survival rate at 2 years for medical therapy and CFVAD implantation were 70 – 80% and 58% respectively (Stewart and Stevenson, 2011) which explains why, to date, only patients classified IV on NYHA are recommended as candidates to MCS. However, patients with blood clotting disorders, severe organ disease or infections that cannot be treated with antibiotics are contraindicated for MCS implantation. Alongside with patient condition, psychological distress is also considered in patient management as after MCS implantation, patient experience relatively high levels of psychological distress and they ought to be capable of undergoing it since psychological outcomes have a considerable effect on the treatment efficiency.

Once the decision of a device implantation is made; depending on the expected time for MCS support and the patient condition, the choice of the appropriate type of MCS (TAH, BiVAD, LVAD or RVAD) is then made. The choice of the specific device is less conventional as it is ruled by physical parameters, clinical current practices, and habits.

#### 1.4.2 Surgical procedure

The surgical intervention to implant MCS device require 3 to 6 hours. The surgical process varies depending on the patient and the surgeon. Below, the main steps of the surgical procedure are briefly presented:

**Patient preparation:** The surgical intervention is performed under general anaesthesia. The medicine is delivered by the anaesthesiologist via monitored intravenous lines. The patient is then put on a mechanical ventilator connected to a breathing tube that goes down the patient throat moving the air in and out of the lungs. The surgical site is afterward sterilized, and the patient is finally ready for surgery.

**Thoracic incision:** In order for the heart and the aorta to be accessible, a thoracic incision has to be made. The incision could be done as a median sternotomy or a thoracotomy. The first is the conventional incision that could be performed for all MCS devices (TAH, VADs). It is an invasive approach consisting in sawing surgically the entire sternum (Figure 1.21). The latter is a minimally invasive approach where the incision is made into the chest wall and could be used for VADs devices implantations (Figure 1.22). Even though several thoracotomies were performed in the literature (Hanke et al., 2015), sternotomy remains the most commonly used (Feldman et al., 2013).

**Extra-Corporeal Circulation:** Right after the incision, an Extra-Corporeal Circulation (ECC) is performed with a heart-lung machine also known as cardiopulmonary



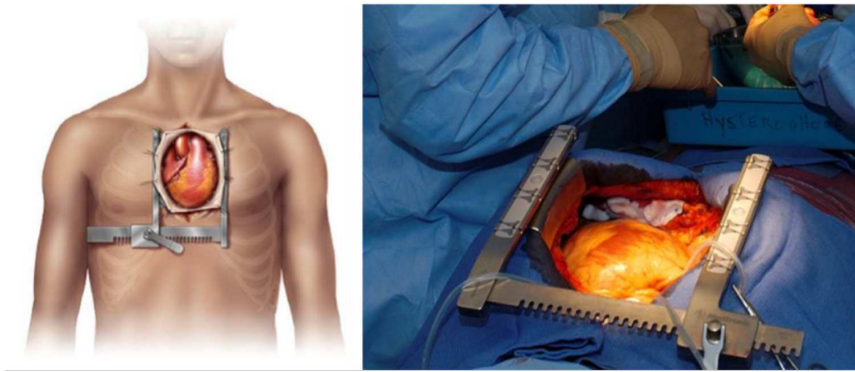


Figure 1.21: Conventional incision - sternotomy.

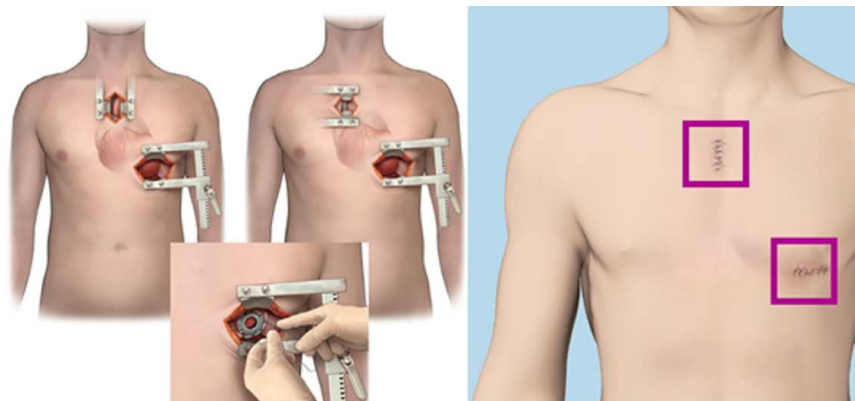


Figure 1.22: Minimal invasive incision - thoracotomy.

bypass pump for TAH and most commonly VADs implantations (Figure 1.23). ECC replaces the heart and the lung functioning throughout the surgery. A tube is firstly anastomosed to the right atrium, vena cava or femoral vein to redirect the blood entering the heart into the machine where the blood is filtered and oxygenated then redistributed to the body via a cannula anastomosed to the ascending aorta or the femoral artery. Once the blood circulation is fully insured by the ECC, the heart is then stopped in order to implant the VAD when associated with further surgical procedure such as aortic valve replacement or to implant the TAH. Otherwise (VAD implantation only), for sternotomy opening, a cardiopulmonary bypass with a beating heart is frequently performed. For thoracotomy opening, the VAD is implanted with a beating heart without cardiopulmonary bypass.

**MCS device implantation:** The MCS device insertion process depends on the type of device implanted. For a TAH implantation (Figure 1.24-1.), the RV is initially incised along the right atrioventricular groove. The incision is carried circumferentially around the RV base ensuring to leave the tricuspid annulus intact. The residual muscle of the ventricle should be thin and 1 cm wide. The same procedure is then performed for the left side of the heart. Afterward, the aorta and the pulmonary arteries are transected just above their respective valves (Figure 1.25-a). Each quick connect



**Figure 1.23:** Extra-Corporeal Circulation (ECC).

is then anastomosed to the annulus of its respective atrioventricular valve (Figure 1.25-b). The LV quick connect is performed first and the RV anastomosis is second (Figure 1.25-b,c). Both ventricles are temporarily inserted; the arteries grafts are measured then anastomosed (Figure 1.25-d). The ventricles and outflow grafts anastomoses are finally leak tested. Once checked, the LV is then permanently inserted first (Figure 1.25-e) and the RV is permanently inserted and positioned second (Figure 1.25-f). Two incisions are added in the left upper abdomen for the drive-lines.

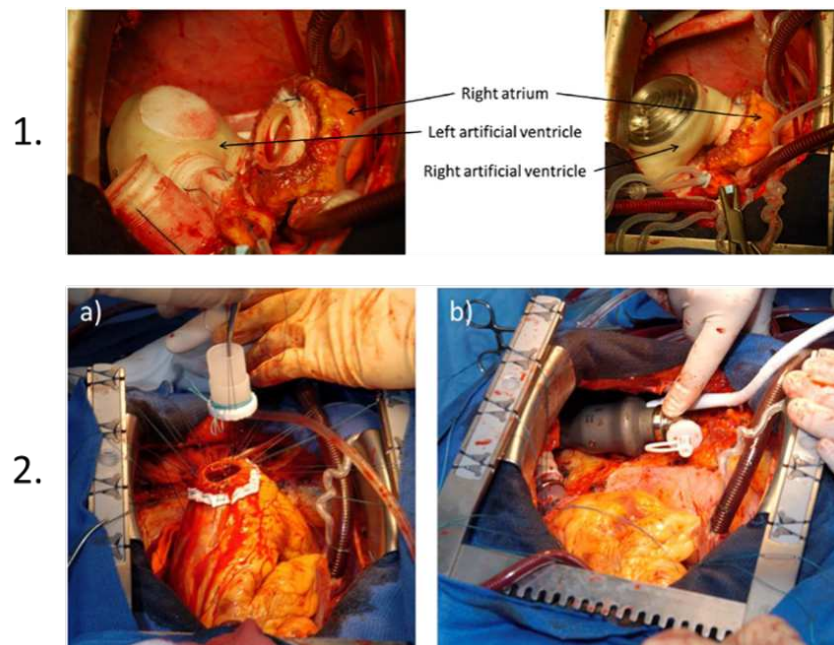


**Figure 1.24:** Mechanical circulatory support implantation - Surgical captures: 1. Total artificial heart implantation (example: Syncardia Total Artificial Heart); 2. Left ventricular assist device implantation with a) insertion of apical cuff, b) insertion of left ventricular assist device within intrathoracic space (example: HM2).

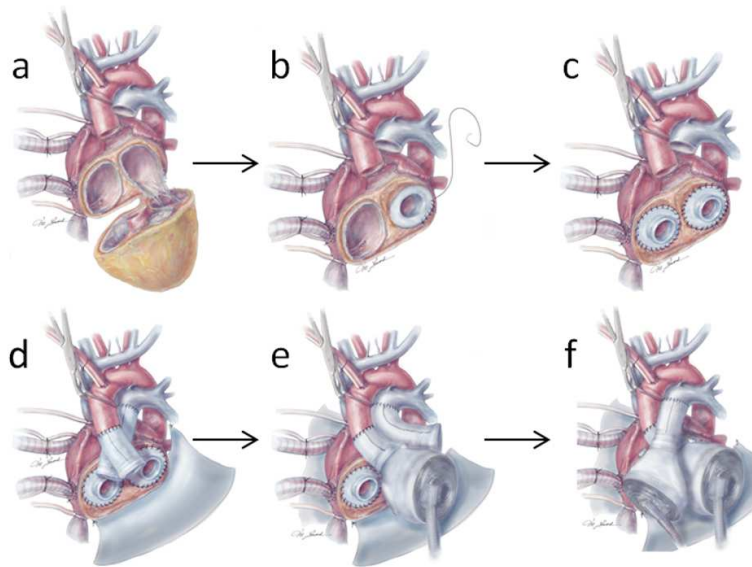


Figure 1.25: Total artificial heart implantation - Surgical steps.<sup>15</sup>

In the case of LVAD implantation (Figure 1.24-2), initially the apex is elevated, located (via a transoesophageal echo-cardiogram) then marked. The apical cuff is positioned then sewn on the LV apex (Figure 1.26-a), afterward, the myocardium is cored inside the swing ring (i.e. “sew-then-core” method; Figure 1.26-b). The coring procedure is specific to the type of the device used. The IC is then inserted in the LV apex, positioned, and secured to the apical cuff; then the apex with the IC attached is returned to its anatomic position (Figure 1.26-c). Once the OC graft is well positioned (lying within the atrioventricular groove between the right atrium and the right ventricle) it is anastomosed to the aorta (Figure 1.26-d).

**Device adjustment and patient closure:** Once the device is implanted and connected to the controller, a purge is performed. The device is turned on and begins to gradually take over the blood circulation till its speed is adjusted to anatomical and physiological parameters. The procedure ends with the removal of the heart-lung machine followed by the closure of the chest.

### 1.4.3 Post-operative follow-up and eventual complications

An INTERMACS study have shown that MCS use have multiple advantages for patients. This prospective analysis is based on data collected from June 23, 2006, to June 30, 2017. In 2017, 168 hospitals participated in INTERMACS and 20,212 patients having MCS device implantation were registered (Kirklin et al., 2017). According to the results, these devices improve the quality of life of the patients as it impacts his “Usual Activities” and “Self-care”. Once some of the HF symptoms are relieved

15. Source (Chung et al., 2020)

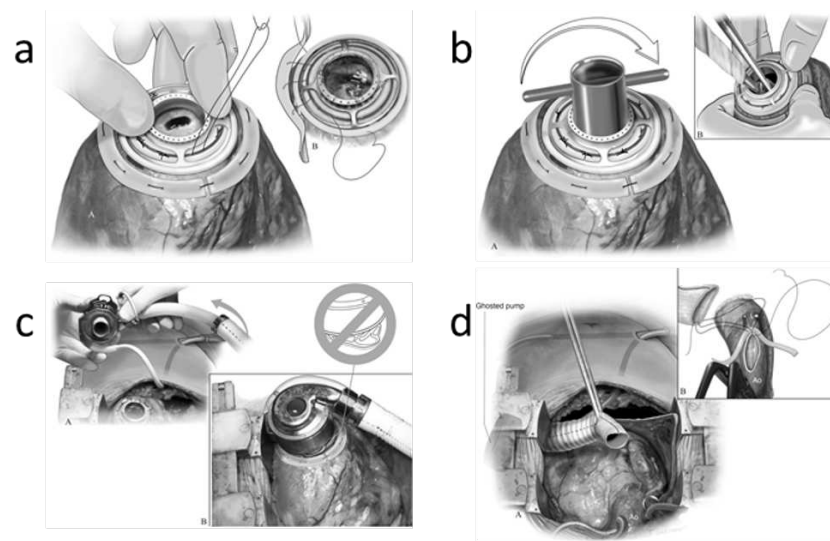


**Figure 1.26:** Left ventricular assist device implantation - Surgical steps (example of HM3).<sup>16</sup>

(short breath, fatigue...), the patient is able to resume several routine activities. According to INTERMACS Quarterly Report – 2017, patient that underwent a MCS implantation have a survival rate of 79.3% and 68.2% for the first and the second years respectively; however it still come with significant postoperative adverse event (Copeland et al., 2012).

**Bleeding** was the major postoperative complication (26.7%) between 2012 and 2014 (Kirklin et al., 2015). The bleeding might be immediate (chest bleeding) or later (internal bleeding). **Infections** come in second place with a percentage of 24.9%. They are usually encountered weeks or months after implantation; nevertheless, they may occur at any time during support; empirical antibiotic treatment is required. Frail patients (immunosuppressed, diabetic, ...) tend to develop infections which may influence the choice of the implanted device (Givertz, 2011). **Cardiac arrhythmia** is a common side effect to MCS implant with a rate of 13.9%. HF promotes atrial arrhythmia, and its prevalence increases with the severity of the disease. Patient with NYHA classification I and II, have a 4% risk factor of developing atrial arrhythmia; however, this risk is nearly 50% once the class IV is reached. Once the LVAD is implanted, patients may present ventricular arrhythmia likely after 30 days. This complication would increase the mortality rate for 9% to 54% (Kadado et al., 2018). **Right HF** is the least likely complication to occur (1.7%). In most cases, this side effect is treated with short-term medication support but for patients that present a severe form, a HT or RVAD is added as a BTT. Right HF complication is rare as prior to LVAD implantation, clinicians assess whether the patient should be implanted with an LVAD or BiVAD / TAH. Their decision is made on the calculation of a “risk score” based on clinical and haemodynamic predictors. Other adverse events may also appear such

16. Source (Beyersdorf et al., 2017)

as **device malfunctioning** which used to be a principal cause of hospitalization and mortality with PFVAD. Nevertheless, this risk was reduced to 3.25% with CFVADs. Malfunctions that are likely to happen are usually minor and pointed with alarms. Rarely, VAD replacement is required.

**Thromboembolic events** are the main complications associated with MCS devices, in the short and long term. they are the main concern of clinicians. They can appear due to high blood pressure, bleeding into the brain or blood clots formed in the LV or the pump and thrown in the aorta. According to INTERMACS data, patients who suffered a stroke within 1 month, 6 months and 1 year are 4%, 9% and 14% , and the incidence of first ischemic stroke within 6 months, 1 year and 2 years are 5%, 8% and 11% respectively (Kirklin et al., 2020). Even though, the stroke rate seems to have decreased with CFVAD along with the administration of anticoagulant, the ongoing risk remains. Thrombosis formation remains a subject to investigations especially since its aftermaths may deteriorate greatly the life quality of the patients and could even be life-threatening.

## 1.5 Summary

Although HT remains the best treatment for HF patients, MCS implantation presents a considerable alternative to graft shortage and transplantation ineligibility. MCS implantation is proven to have improved the condition and survival rate of the patients. Nevertheless, it is associated with adverse events that may be life threatening or heavily impacting the patient quality of life. Some complications, such as thromboembolic events remain a critical issues. These issues are sometimes inevitable especially when their factors remain unknown (Zhang et al., 2019). Next chapter presents the positioning of our work in relation to the state of the art related to LVAD implantation and associated complications.

## State of the art & Work positioning

This chapter provides an overview of the researches issues related to the LVAD implantation, especially to the IC. The first section presents the interaction between LVAD implant and anatomical structure. The second and third sections address the resulting morphological and fluidic constraints, respectively. The fourth section focuses on reported works using Computational Fluid Dynamics (CFD) computation where an overview of the exploit Quantities Of Interest (QOI) and models limitations is presented. The fifth section summarizes the state of the art and highlights the positioning and objectives of our work.

### 2.1 Device-structure interactions

Although LVAD implantation is of therapeutic interest to patients, it significantly impacts their anatomy and physiology. Indeed, the implant affects the blood flow, geometry, behaviour, and properties of many anatomical structures. The interaction between the device and the surrounded anatomical structures (Figure 2.1) may deteriorate the device efficiency or lead to adverse events.

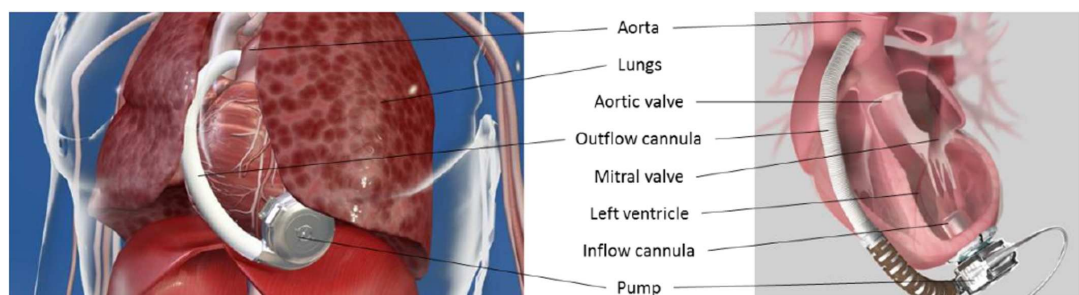


Figure 2.1: Different anatomical structures interacting with the LVAD device.<sup>1</sup>

The LVAD may rub against the thoracic wall resulting in chest pains to the patient or the pump itself may compress the RV affecting its shape and volume. This may

promote geometrical modification and alter RV functioning. The anastomosis of the outflow tract to the ascending aorta may be positioned in front of the right cavity thus interfering with its normal function. In these cases, patients are more likely to develop right heart failure.

The OC anastomosis has several possible configurations for LVAD implantation. During surgery, the surgeon cuts the outflow graft to the length necessary for reaching the aorta making it an influencing parameter of Wall Shear Stress (WSS) and blood velocity. However, this influence has not yet been investigated, and no clinical guidelines have been stated. In fact, the OC could be anastomosed in two distinct sites: the ascending and the descending aorta. The anastomosis site choice depends on the type of surgery performed: when the LVAD implantation is performed through a thoracotomy, the OC is grafted to the descending aorta since accessing the ascending aorta is difficult. During a sternotomy, the OC is grafted to the ascending aorta. (Litwak et al., 2005) observed that a descending aorta anastomosis results in a reduced flow within the aorta arch. Likewise, (Mazzitelli et al., 2013) concluded that ascending aorta graft contributes better in upper arteries. However, (Bonnemain et al., 2013) obtained similar flow rates for both configurations.

The IC of the LVAD may be sutured to two distinct heart structures: in the left ventricle or the left atrium. Current clinical recommendations promote the LV suture despite its drawbacks. The IC suturing puts the apical region under important stress, the intra-thoracic pump speed may be so important that the IC distal end may suck the LV wall (suction event). In this case, a decrease in the pump speed is recommended. Furthermore, the left ventricle is depleted with the device start-up. The decrease in LV volume decreases LV work; the pressure and volume overload are lowered, which reduces LV wall stress and may contribute to reverse modelling (Jhun et al., 2014). LV remodelling also draws the ventricular wall closer to the distal point of the IC which may promote suction events that may enhance device dysfunction and even right heart failure.

IC insertion within the LV impacts also the distribution of blood flow within the ventricle and aorta. Blood flow disorders and turbulence have been found within the aorta. The most important alteration consists in the presence of reverse flow that compromises haemodynamics and may harm the Aortic Valve (AoV) (Alonazi et al., 2015). The LV apex has been pointed out as a region favourable to thromboembolic complications (May-Newman et al., 2017). Moreover, IC obstruction and suction events momentarily alter blood circulation and pump functioning.

In this context, vortices, blood stagnation and recirculation have been also identified within the ventricle. Vortices lessen ventricular work, ease the LV filling, and contribute to LV washout. They also contribute to suction events (Kheradvar et al.,

---

1. Source [heartware.com](http://heartware.com)

2007). Blood stagnation and recirculation are likely to contribute to thrombi formation (Quaini et al., 2011). Blood recirculation may affect the efficiency of the rotor and in worst cases breaks it. A blood clot may also be responsible for an embolic event that may migrate to the brain. Formerly, it was recommended to close the aortic valve to force blood down to the IC. Nevertheless, this approach enhanced thrombus formation around the AoV region (John et al., 2010). The closing of the AoV may also put the patient in a dramatic and fatal condition if the device is damaged as the LV would no longer be able to eject blood in the aorta. Therefore, current recommendations preconize to maintain the aortic valve functioning. However, no recommendation concerning its opening frequency have been explicitly stated to date.

In conclusion, LVAD implants entail various physiological changes that cause post-operative complications. Two distinct types of interactions between the LVAD and anatomical structure may be identified: morphological constraints and fluidic modifications that may result in mechanical repercussions. The following presents different factors that can potentially impact the morphological properties of the LV.

## 2.2 Morphological constraints

LVAD implantation results in morphological alterations that consist of anatomical and geometrical constraints that may lead to chest pain, alterations in blood flow, and even a right HF. Although pre-operative and per-operative recommendations are stated, surgeons continually face morphological constraints. The following presents the main difficulties and the solutions proposed in the literature.

### 2.2.1 Anatomical constraints

Due to atherosclerosis, HF patients tend to suffer from aortic calcifications. For LVAD implantation, OC must be anastomosed to an area free from calcification. Otherwise, a different implantation site must be considered (Ahmed et al., 2014). Investigating the location of the areas of calcification ahead could be helpful to anticipate pre-operatively the site of OC graft which may guide the surgeon and reduces the exploration time during the intervention.

Throughout the surgery, the heart continues its beating. These movements may hinder IC anastomosis resulting in IC malpositioning such as IC apical insertion site, angular deviation or even both. Clinical diagnosis tends to claim that in addition to suction events, these modifications may promote blood stagnation and thrombus formation.

For MCS implantation in general, several significant issues arise from the intra-thoracic space as surgeons may encounter difficulties closing the chest wall at the end of the device implantation. Due to the consequent size, the implanted device could be larger



than the existing intra-thoracic space. The neighbouring organs as well as the chest wall could be compressed or dislodged. For LVAD, the dislodgement enhances potentially the compression of the right ventricle and favours the IC angular deviation. A relationship between IC angular deviation and pump thrombosis have been reported.

While LVAD pumps the blood from the ventricle, the pressure on the LV is reduced, resulting in an important size reduction. The change in LV volume depends on the amount of support provided through the pump speed. Another issue consists of the different motions like ventricular depletion, heart motion and lungs inflation and deflation within the intra-thoracic space. These motions change the volume available within the chest wall that may impact the position of the device and its interactions with the surrounding organs. The choice of a compatible device according to the patient intra-thoracic space is a fundamental step to be performed pre-operatively.

### 2.2.2 Overview of the literature

Several methods have been developed over previous decades to investigate device compatibility to the patient anatomy (Affeld et al., 1983). In the following, reported work related to the intra-thoracic space issue for MCS devices (TAH and LVAD) is presented. Many methods have been attempted, such as implantation on animals, cadavers, measuring the intra-thoracic space on chest radiographs or 3D medical images .... The latter is usually used in the context of intra-thoracic space or cardiovascular system to illustrate structural or functional information which enables the investigation of the relevant pathology within real conditions and organs interactions.

Few works investigated the compatibility of MCS devices with available intra-thoracic space relying on pre-operative images. Figure 2.2 illustrates research that focused on such matter, where three purposes are highlighted: Device design, compatibility and implantation planning. The first purpose is to optimize the MCS design (for industrial use). The second purpose is to develop quantifying criteria based on the patient anatomy to define device compatibility. The third purpose is pre-operative planning to prepare and anticipate the device implantation (for clinical use). For that, except for (Fujimoto et al., 1985) and (Dickstein et al., 2008), who used a general model and an MRI respectively, all other researchers have represented several chest structures based on CT volumes and segmentation.

For MCS designs optimization, (Fujimoto et al., 1985) measured a restriction size and shape TAH criterion for a model with general morphology while (Komoda et al., 1992) have investigated the same issue but for six healthy subjects. (Noecker et al., 2007) evaluated a new VAD pump based on eleven CT while (Fritschi et al., 2013) also used CT images to study the interactions between TAH and mediastinum. (Drum-

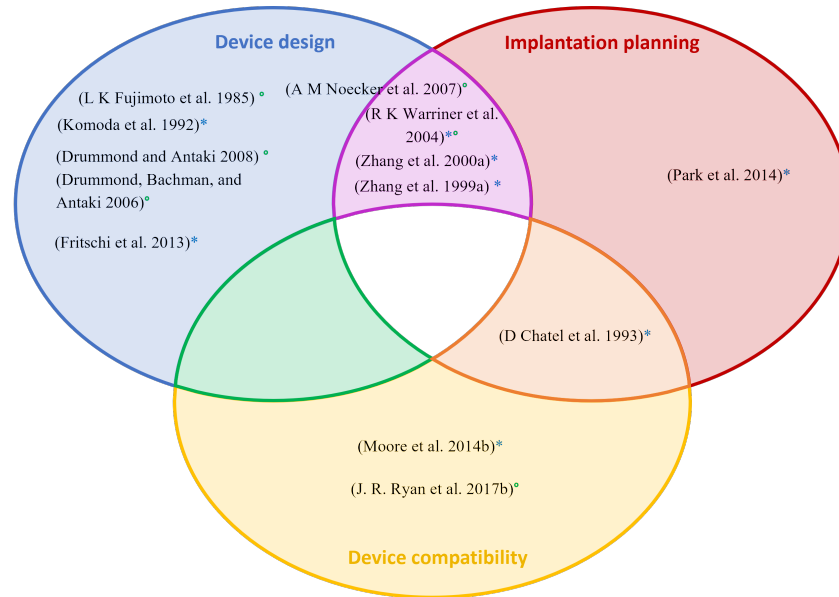


**Figure 2.2:** State of the art of MCS numerical approaches.  
 ° LVAD issues; \* TAH issues

mond and Antaki, 2008; Drummond et al., 2006) developed a paediatric VAD on 3D models also based on CT. Finally, (Affeld et al., 1983) mentioned the idea of testing the compatibility of a TAH pre-operatively. Only (Noecker et al., 2007) referred to the possibility of clinicians to pre-operatively discuss the developed paediatric VAD.

For device compatibility, studies attempted to evaluate the eligibility of patients to TAH implantation as it requires more intra-thoracic space: (Chatel et al., 1993) developed a 3D model of the cardiovascular structures from which they define the shape and intra-thoracic space to measure volume and geometry parameters. (Moore et al., 2014) applied fit criteria developed by (Copeland et al., 1999) to test its reliability on three clinical cases virtually implanted. Then, they compared two TAH designs for paediatric and small patient use (Moore et al., 2016). Only (Ryan et al., 2017) investigated LVAD implantation virtual fit. They virtually implanted small patient and evaluated the minimum size required for paediatric patients for a given device.

For implantation planning, four articles discussed a pre-operative MCS virtual implant to anticipate its fitting with patient anatomy. (Zhang et al., 1999, 2000) established a prototype of environment simulation for TAH implant aiming to optimize the TAH design as well as evaluate its anatomical fit. Similarly, (Warriner et al., 2004) proved that implementing a rapid screening method based on an anatomical fit was feasible. This method could be used pre-operatively as a decision-making tool of candidates for an intra-thoracic mechanical device. As far as we know, (Park et al., 2014) is the only research that specifically focused on planning device implantation by proposing a 3D model based on clinical cases to assess whether the TAH device would fit in the intra-thoracic space using quantitative criteria.

Investigations dealing with intra-thoracic space did not consider the thoracic motions (beating heart and breathing). Most of the research aiming for implantation planning focused on TAH devices and the few of them that took an interest in VAD devices, did not consider the compatibility of the patient anatomy with the IC insertion. (Anselmi et al., 2016a) developed a computer simulation tool that uses CT scan of candidates for LVAD implantation. This tool considers an aligned IC, coaxial to the MV and parallel to Inter Ventricular Septum (IVS), and suggests LVAD and IC implantation's sites in the intra-thoracic space and LV coring location, respectively. Then, the tool illustrates overlap between the device and the chest wall after closure (for clinical use). In another work, (Anselmi et al., 2016b) used also CT segmentation and 3D reconstruction of implanted patients. They attempted to link patients presenting LVAD related complications (thromboembolic events, pump dysfunction, thrombosis) with IC angulation. They observed a correlation when the IC is deviated toward IVS and none when the IC is deviated toward the anterior or posterior wall. Using the same method, (Anselmi et al., 2017) compared the IC angulation toward IVS and toward anterior LV wall between patients implanted with HeartMate 2 (HM2) and Jarvik 2000 LVAD pumps. They concluded that after chest closure, HM2 implantation was more prone to IC angulation than Jarvik 2000, for both angulations. (Sacks et al., 2015) mentioned the use of CT of implanted patients to anticipate eventual adverse outcomes due to IC angulation. They concluded that IC angulation was associated with IC obstruction and adverse event, especially thrombosis.

To conclude, researches attempted to develop device implantation planning tools and compatibility criteria related to the intra-thoracic space. Depending on the patient, the available intra-thoracic space might require to relocate the IC implantation site or during chest closure, the IC may deviate from an hypothetical ideal IC angulation. This angulation of the IC, may influence the haemodynamic within the ventricle. In the following, an overview of how the LV haemodynamic issues are addressed in the literature is presented.

## 2.3 Mechanical and Fluid issues

IC implantation influences the flow within the ventricle. First, the different means available for haemodynamic analysis are presented. Then, a state of the art of works focusing on haemodynamic influencing factors (LVAD pump and IC features) is held.

### 2.3.1 Overview

Clinical methods have been considered to measure physiological data on patients. Cardiac output before and after physical efforts can provide significant information about the efficiency of the pump and the health of patients (Aymami et al., 2016).

Similarly, medical imaging is often used for retrospective studies. Doppler echocardiography is helpful in LVAD therapy (Estep et al., 2010) and is easily available in daily life use to optimise the pump speed, assess MV regurgitation or myocardium recovery. It is more generally used to measure the haemodynamics of both ventricles in patients suffering from cardiovascular disease (Porter et al., 2015). Echocardiography allows the evaluation of different parameters in the ventricle such as chamber dimensions, the velocities of the mitral flow during systolic and diastolic phases, stroke volume, cardiac output, and pressure. Although this technique has the advantage of being non-invasive and provides several measurements, it depends though heavily on the operator. For LVAD patients, echocardiography remains challenging as patients often have poor echogenicity.

Animal experimentation have significantly contributed to the understanding of cardiovascular diseases over the years (Chorro et al., 2009) by providing information on aetiology, pathophysiology or medications efficiency and mechanism (Leong et al., 2015). In-vivo studies are less subject to environmental variations, easier to manage than human studies. Although they are valuable as the anatomy and physiology are similar to humans, obtained results might be unsuitable or too diverse to be compared with humans LVAD. Apart from ethical concerns, experimentation requires major time and resources investment.

In-vitro models are less strict; thus, more eligible for new technologies development, not suited for living beings. Compared to in-vivo model, variable control is greater and experimental time and cost are lower (Ryan et al., 2016). Although the use of biomaterials has significantly developed in-vitro models, it is often necessary to resort to simplified models, that may not always reflect the natural progression of multiple pathologies, especially for cardiovascular system due to its complexity. In the context of LVAD investigations, a mock circulatory loop is usually used.

Different from experimentation, computational methods have more and more been used over the last years. Virtual models are fast, thrifty and avoid high-risk prototyping (Morris et al., 2016). Consequently, these approaches were also operated in the cardiovascular field (HF, congenital heart diseases, valve prosthesis, VAD, etc...). They may be valuable for designing devices, clinical trials and improvement of treatment strategies (Taylor and Draney, 2004). Even though, the prediction of surgical outcomes remains challenging, two techniques are distinguished: CFD modelling and Lumped Parameter Model (LPM). The latter, also known as a zero-dimensional computational model, simplifies a complex physical system into discrete entities using differential equations to describe the components system behaviour. However, it cannot afford three-dimensional information, for example, flow field visualisation. In opposition, CFD modelling provides temporal and spatial resolutions that may not be easily obtained with experimentation, such as constrain visualisation. In the con-

text of LVAD, these different methods have been considered for LV haemodynamic analysis.

To investigate the impact of LVAD implantation on ventricular flow, these different means were used to study the influence of the pump and IC features.

### 2.3.2 Issues related to LV haemodynamic

LVAD support changes blood flow and properties within the ventricle. These changes are due to blood pumping and presence of IC (McCormick et al., 2013) and may lead to thrombosis related complications. (Litwak et al., 2008) performed a retrospective analysis on 141 VAD implanted calves for up to 200 days to analyse adverse events associated with VAD implantation. They investigated different implantation sites (LV apex vs. atrium), with eleven different VAD brands and types (CFVAD vs. PFVAD) and considered all VAD components (IC, OC, pump, connector, cabling and percutaneous line). They recorded 294 adverse events that were associated with the IC and the pump in 56% and 39% of cases, respectively. In the following, an overview of works in the literature related to the influence of the pump and IC on LV haemodynamic.

**Pumps type and setting:** Few studies focused on the impact of continuous vs pulsatile support on LV haemodynamic. A computational model study reported that PFVAD provides higher LV unloading than CFVAD (Gohean et al., 2013). The research, however, did not include flow patterns investigation. Pump speed also impacts the haemodynamic of the ventricle and the pumping efficiency alongside the anatomical configuration. (Addetia et al., 2018) demonstrated that the pump speed modifies the geometry of both ventricles (LV and RV) based on 31 echocardiography images. They observed that increasing pump speed impacts the IVS by reshaping the LV less spherically and more conically. These anatomical modifications result in increasing RV volume while decreasing the LV volume, which enhances the occurrence of suction events. On the one hand, (Li et al., 2002) proved using numerical simulation that the pump loses its efficiency when the support is too important. On the other hand, the increment of the pump speed, reduces the blood stagnation volume (Fraser et al., 2010). Further investigations are thus needed to define the appropriate balance between these effects.

**IC anastomosis:** The anastomosis of the inflow cannula impacts the flow field of blood. As already mentioned, clinical guidelines recommend the insertion of the IC at the LV apex. Only few research investigated the impact of IC anastomosis in different sites. (Korakianitis and Shi, 2007) and (Hsu et al., 2016) used numerical methods to look into the haemodynamic impact for two distinct anastomosis sites : LV atrium and LV apex. The obtained results agreed with clinical recommendations favouring

apical insertion that reduces ventricular wall tension and dilation suitable for LV recovery. (Klotz et al., 2016) conducted an ex-vivo experiment on the same matter using a mock porcine suffering from HF. An analysis of flow patterns and enzyme activation location was also performed. Results tended to favour apical insertion of IC as it reduces potential side effects such as intra-cavity clotting and its aftermath.

**IC features:** Different research focused on different aspects of IC feature and their impact on LV haemodynamic. One of these features is the influence of IC tips. Using an in-vitro study, (Laumen et al., 2010) considered a mock loop of a beating ventricle inserted with two commercialised IC with different tips and evaluated the impact of IC tip geometry on the dynamics flow using Particle Image Velocimetry (PIV) measurements. They concluded that IC tip geometry had small influence on ventricular flow. (Bachman et al., 2011) concentrated on the degree of ventricular decompression and collapse for two different IC forms, using a mock loop of a non-beating bovine heart. They concluded that IC tip geometry may greatly affects suction events which enhances myocardial trauma. Using CFD simulations, (Fraser et al., 2010) studied three available venous cannulas sizes of a commercial paediatric VAD. They observed flow field and shear rate to identify potential stagnation and thrombosis regions, respectively within each cannula. (Tsukiya et al., 2011) conducted a numerical flow analysis for a lantern-like IC tip designed for short-term use. They considered pressure loss, velocity vectors and shear stress to assess hydraulic resistance, potential stagnation and thrombus formation, respectively. Using a generic LV model, (Liu et al., 2012) focused on the influence of tip shape on LV haemodynamic and suction event aiming to design an IC suitable for long-term use. They observed the flow field, static pressure and WSS in four different IC tips to identify potential stagnation and thrombosis regions. Inspired by (Fraser et al., 2010), (Entezari et al., 2021), used CFD simulation to investigate the influence of the number and size of holes in one of the venous cannula previously simulated by (Fraser et al., 2010) by considering LV wall motion. They considered velocity, vorticity and shear rate to attempt to evaluate thrombosis. They observed that the increase of the size or number of holes decreases blood stasis and thrombosis risk and increases hemolysis and platelet activation. However, the increase in size or number of holes, increases also vorticity, due to wall motion, which enhances thrombosis risk. They finally concluded that the standard IC geometry presented, in average better results. Even though investigating the effect of IC tip remains interesting, currently commercialized LVAD have an IC commonly shaped as a cylinder.

Another feature is the impact of the IC length. A long IC may damage the functioning of the MV and AoV since the pressure induced by the aspiration of the LVAD is too important on the leaflets of the valve and chordae. The more the IC is long, the more it is likely to interact with the LV wall which may promote suction events. (Schmid

et al., 2008) carried out a retrospective analysis on 2016 patients and observed that 3.8% of patients implanted with a long IC had thromboembolic events versus 23.3% of patients implanted with a short IC. However, (Laumen et al., 2010) used a beating mock ventricle and concluded that IC length highly impacts blood flow, thus, ventricular washout. (Ong et al., 2013) noticed, through CFD simulations, that the increase of the IC length increases vortices intensities and blood stagnation at the apex that may lead to thrombus formation. (May-Newman et al., 2017) used a mock circulatory loop to demonstrate that flow alteration arises the further the IC is inserted into the LV. (Liao et al., 2018) coupled CFD and LPM models to consider LV motions for four different IC lengths. They observed that a longer IC promotes LV washout and reduces Residence Time (RT), a short IC disturbed vortices near the IC, diminished vortical structure and lowered the peak in kinetic energy, while the same low pulsatility regions and the fluctuation of stagnation regions during the cardiac cycle, were observed regardless of the IC length. They concluded that that optimal IC length depends on LV morphology. (Sonntag et al., 2019) simulated three different IC lengths of the EVAHEART pump. They deduced that IC length does not influence the pumping or the systemic blood flow and a decrease of IC length reduces IC malpositioning risks and increases kinetic energy, the interaction with intra-ventricular vortices and thrombosis risk. (Motomura et al., 2019) experimented on eight bovines implanted with the EVAHEART 2 pump, which has a short IC length. They showed that the short IC tolerates better inflow malposition and may mitigate the risk of thrombus formation and ventricular wall suction. However, (Chivukula et al., 2020) used a CFD approach. They considered RT and shear stress of launched particles to define a High Thrombogenicity (HTh) zone and quantify Thrombogenic Potential (TP) score by simulating a small-sized ventricle suffering from HF. They concluded that a long IC increases the proportion of particles in the HTh zone and the TP score. (Entezari et al., 2021) also took interest in IC length, using CFD simulation. They observed that increasing IC length increases stagnation and reduces thrombosis risk, platelet activation and hemolysis. However, due to LV motion, IC length increases vorticity which enhances thrombosis risk. They finally concluded that the IC standard geometry in average showed better functioning conditions.

To summarise, several IC features issues remain present as and further investigations are required as the results in the literature are controversial. Even though IC is rigid and not adjustable while performing surgery, its diameter and length vary depending on the LVAD brand. It is possible to consider that a specific length or radius of the IC may be recommended depending on the LV anatomy and shape. Such studies may influence surgeons in the choice of the device to be implanted.

**IC angulation:** IC angulation is used to designate the angular deviation of the IC axis from the LV long axis, toward the IVS (Figure 2.3). The terms IC malposition,

IC orientation, IC angular deviation, IC angle and angled IC are also used in the literature. An aligned IC is when the IC long axis is aligned with the LV long axis and directed toward the MV ( $IC = 0^\circ$ ). IC angulation is susceptible to influence pump efficiency and promote suction events and thrombogenic potential, while an aligned IC is an hypothetical ideal angulation assumed to favour blood washout via the IC as well as to limit the suction events. Figure 2.4 presents two postoperative radiography images of LVAD implantation showing two different IC angulations. Few studies have focused on the impact of the IC angulation on the factors of stagnation and the thrombosis risk within the LV. Using in-vitro models, (Laumen et al., 2010) realised a beating mock ventricle. The LV geometry was extracted from MRI images of a dilated LV at end systole and the study investigated an extreme IC angulation, bend toward the outflow tract. They noticed that IC angulation leads to more vortices, resulting in a better washout. (May-Newman et al., 2019a) investigated, through a mock circulatory loop, the impact of two different IC orientations. They suggested that IC angulation tends to decrease regional flow, pulsatility and vortex energy, which may increase thrombosis. Using radiographic images, (Aigner et al., 2021) focused on the correlation between pump thrombosis and IC angulation using chest X-rays and CT scans for patients implanted with HM2 and HeartWare Ventricular Assist Device (HVAD); the study was carried out for 33 patients. There was no correlation between pump thrombosis and IC angulation for HM2 patients. However, IC angulation was associated with pump thrombosis for HVAD patients. (Imamura et al., 2020) and (Schlöghofer et al., 2022) also carried out the same researches on 64 and 42 patients, respectively, implanted with HeartMate 3 (HM3). While the former observed that small IC angulation ( $\leq 28^\circ$ ) presented improved cardiac unloading (lower central venous pressure, lower pulmonary capillary, wedge pressure, smaller LV and RV sizes and better RV functioning) and lower incidence of death or heart failure readmission, the latter, concluded that a small IC angulation ( $< 10^\circ$ ) serves as a risk factor of ischemic stroke and worse survival. Using CFD computations, (Chiu et al., 2017) identified two other angulations present in some LVAD devices. They used CFD simulation to investigate different elbow and circumferential IC angles and evaluated TP through accumulated stress of virtual platelets. (Prisco et al., 2017) compared blood stagnation by introducing a virtual ink for two extreme IC implantations. However, little differences were observed between both configurations. (Chivukula et al., 2018) evaluated IC angulation by defining a TP score based on platelet shear stress history and residence time; the proposed score was, however, unable to assess the risk of thrombosis for IC angulations greater than  $\pm 14^\circ$ . (Ghodrati et al., 2020) simulated two LVAD implanted LV geometries based on CT scans. They simulated two models of two ventricles with different IC angulations implanted at the apex. Their analysis put the focus on the distance of the IC to the lateral and septal wall, rather than the angle of the IC with respect to MV–IC axis. They concluded that the model with central implantation and higher IC angu-



lation had higher blood washout and lower stagnation. Only one study focused on thrombus formation mechanism due to IC insertion. (Rojano et al., 2021) simulated, a dilated LV and introduced a simplified biochemical scheme for thrombin formation. They concluded that platelet activated mechanically predominate the chemical platelet activation. This mechanical activation promote accumulation along the circumference of the inner rim of the IC was coherent with thrombus deposition observed clinically and that the biochemical scheme resulting in a concentration of thrombin occurs in regions with low shear stress and poor wash-out. These regions are due to coagulation reaction of tissue damage rather than mechanical platelet activation, which explains thrombus formed at early stage of LVAD implantation due to surgical procedure but not at the long-term.

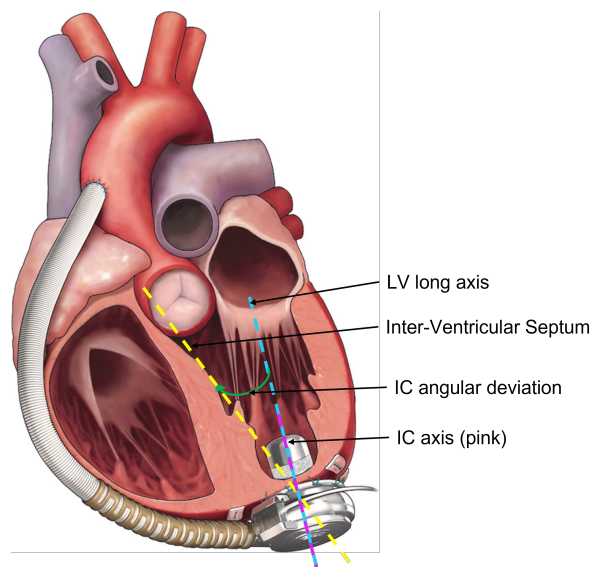


**Figure 2.3:** IC insertion: aligned IC vs. angled IC

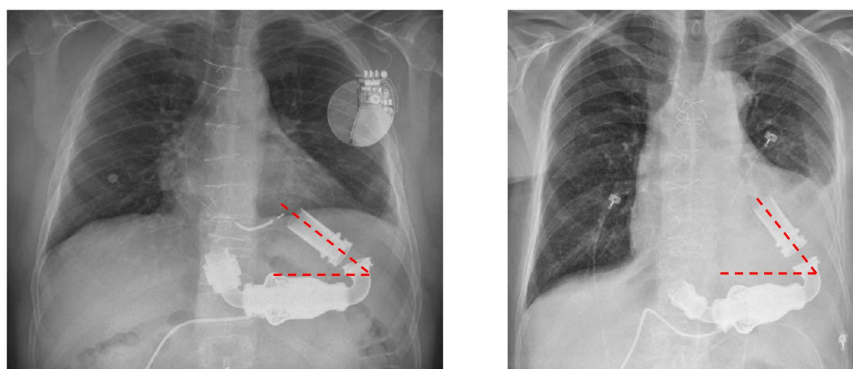


**Figure 2.4:** Postoperative radiographs illustrating two IC angulations of the HM2.

To summarise, pump settings, IC implantation site and especially, IC features (length, angulation, tip shape) seemingly impact pump efficiency and blood flow pattern. Reported work focus mainly on the IC as an influencing factor of anatomical and physiological modifications that may occur during LVAD support.

Figure 2.5 summarises pump and IC influential features and associated anatomical and fluid consequences. Research investigated the influence of IC features on ventricular haemodynamic and attempted to link blood flow alterations with the risk of thrombosis. Nowadays, CFD computation analysis are becoming more used in the research field as they are affordable and allow complex investigations. In the following, we will concentrate on research that investigated the influence of mechanical and fluid alterations of LVAD on ventricular haemodynamic using CFD computation.

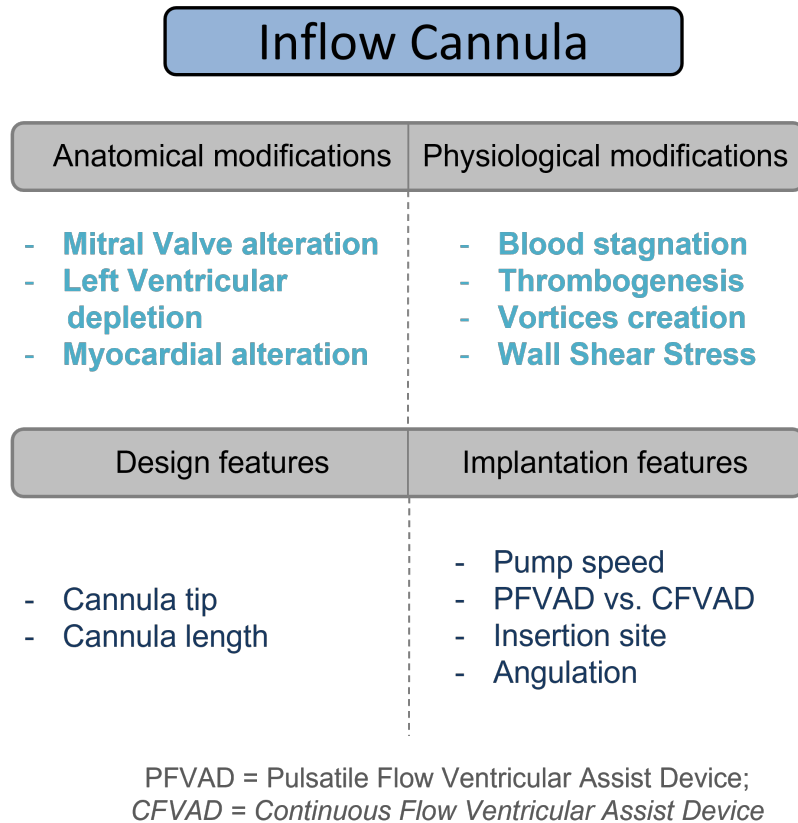


Figure 2.5: Summary of IC influential features and related consequences.

## 2.4 Computational modelling

CFD simulations enable evaluating and visualizing complex physiological entities (such as flow field and constraints distribution) that clinical methodologies may be unable to measure. Its non-invasive character and low cost allow various settings and analysis. Nowadays, in-silico models are exploited for decision support purposes. For CFD simulations, defining the appropriate boundary conditions may present several difficulties due to data sparsity. This section aims to give an overview of the influence of LVAD implantation on LV haemodynamic through CFD computation. QOI, results and model limitations from the literature are presented.

**Quantities of interest:** In order to investigate the influence of LVAD implantation on LV haemodynamic, research considered several QOI. Table 2.1 presents research carried out on factors impacting the ventricular haemodynamic. The first column of the table presents the different subjects of interest, the second column enunciates the influencing factor, and the third column presents the investigated QOI and main results.

Depending on the research interest, several QOI are investigated. They consist mainly in Pressure, Velocity, RT, Shear Stress and Vorticity. While Pressure is used in assessing suction events, the remaining QOI are used to analyse LV haemodynamic, through the risk of thrombosis. Thrombus formation is a complex combination of blood stagnation, platelet activation and chemical reactions, all not fully understood. Only one study considered a simplified version of the chemical aspect alongside with blood stagnation and platelet activation (Rojano et al., 2021). Results revealed that the thrombosis occurring at the long-term of LVAD implantation, was likely associated with the mechanical factors: blood stagnation and platelet activation.

Focusing on IC angulation, reported work attempted to assess these notions by considering different QOI. (Prisco et al., 2017) tried to evaluate blood stagnation by introducing a virtual ink. (Chivukula et al., 2018) qualified the blood stagnation based on the velocity path-line and attempted to develop a TP score based on mass-less platelet accumulated shear stress and RT. (Ghodrati et al., 2020) restricted their interest to the apical region. They qualified LV washout through velocity path-lines and investigated low velocity magnitude and low/high WSS areas seeking to evaluate blood stagnation and platelet activation, respectively.

The evaluation of blood stagnation, platelet activation and thrombosis risk, remains a challenge and although the main QOI involved in their evaluation are more or less known, how to exploit and combine them to develop a thrombosis marker remains an open issue.

**Limitations:** Despite being of real interest, CFD models still have limitations. The main limitations reported in the literature are presented in Table 2.2, where the first column presents the main limitations, the second column enunciates the associated consequences and the third column present the scientific justifications for these assumptions.

Most of the investigations held used 3D models. However, 3D models remain complex and are associated with an imposing computation time. Indeed, all the researches carried out had limited configurations and LV models except for (Ghodrati et al., 2020) and (Liao et al., 2018). They investigated two and six ventricles' shapes respectively. Whether generalised or patient-specific, a single ventricular shape may hinder the generalisation of the obtained results to all LVAD patients.

<b>With vs Without LVAD</b> (Jhun et al., 2014) (McCormick et al., 2013)	<u>With LVAD</u>	Vortex more important ↘ P° and ↗ MV inflow Basal region: Low velocity & important RT Apical region: Low velocity & important RT High WSS at the apex
<b>Amount of support</b> (Fraser et al., 2010) (Jhun et al., 2014) (Prisco et al., 2017)	$WSS_{ED} > WSS_{ES}$ ↗ Pump speed	Proportional ↘ WSS Proportional ↘ LV <sub>Volume</sub> ↘ V <sub>Stagnation</sub>
<b>Implantation site</b> (Prisco et al., 2017) (Ghodrafi et al., 2020)	<u>Apical vs Diaphragmatic</u> <u>Apical (Centred)</u>	virtual ink: Modest difference in stagnation ↘ Stagnation (low velocity area) ↘ WSS ↗ LV washout (velocity pathlines)
<b>IC Angulation</b> (Chivukula et al., 2018)	↗ IC angulation % 0°[-14°, 14°]	↗ velocity pathlines spiralling ↗ RT ↗ WSS ↗ thrombosis risk
<b>Cannula length</b> (Ong et al., 2013) (Fraser et al., 2011) (Sonntag et al., 2019) (Chivukula et al., 2020) (Liao et al., 2018) (Entezari et al., 2021)	↗ Length	Proportional ↗ vortex intensity ↗ Stagnation near the apex ↗ WSS at the basal region ↘ WSS at the apex
<b>Cannula tips</b> (Liu et al., 2012) (Tsukiya et al., 2011) (Fraser et al., 2010) (Entezari et al., 2021)	<u>Trumpet / Caged / Blunt / Beveled</u>  <u>Lantern-like</u>  <u>12F / 16F / 24F (Medtronic)</u> <u>Number / size holes (Medtronic)</u>	Worst: Caged ( <i>turbulent effect</i> ) Best compatibility: Trumpet ( <i>no low velocity, no backflow</i> ) More obstruction: Blunt & Beveled  Potential region of thrombus formation: between the inlet holes & the struts  Worst: 24F (↗ risk of blood clotting within IC)  ↘ stagnation ↗ Paletet Activation (WSS) ↗ hemolysis ↘ thrombosis (shear rate) ↗ thrombosis (vorticity)
<b>VAo opening</b> (Prisco et al., 2017) (Sonntag et al., 2019)	<u>Partially opened</u>	↘ Stagnation
<b>Suction events</b> (Ong et al., 2012)	Suction events promote the alteration of vortex patterns	
<b>Thrombogenesis</b> (Rojano et al., 2021)	The platelets were activated at the cannula tip mainly and slightly at the apex. Thrombin production is more triggered by blood coagulation (stagnation) rather than mechanical platelet activation (WSS).	

**Table 2.1:** Literature summarizing the factors influencing physiological modifications of the hemodynamic in the left ventricle.

P° = Pressure; MV = Mitral Valve; VAo: Aortic Valve; RT = Residence Time; WSS = Wall Shear Stress; LV = Left Ventricle; V = Volume

Limitation	Consequence	Justification
<b>LV rigid</b> (Ghodrati et al., 2020) (Chivukula et al., 2020) (Chivukula et al., 2018) (Prisco et al., 2017) (Ong et al., 2012) (Liu et al., 2012) (Tsukiya et al., 2011) (Fraser et al., 2010) (Rojano et al., 2021)	<ul style="list-style-type: none"> <li>– Flow dynamics are simplified</li> </ul>	<ul style="list-style-type: none"> <li>– Patients implanted with VAD suffers from severe systolic dysfunction:               <ul style="list-style-type: none"> <li>→ Important impaired contractile reverse</li> <li>→ Minimal ventricular motion</li> </ul> </li> </ul>
<b>Blood : the laminar assumption</b> (Ghodrati et al., 2020) (Chivukula et al., 2020) (Liao et al., 2018) (Prisco et al., 2017) (Ong et al., 2013) (Fraser et al., 2010)	<ul style="list-style-type: none"> <li>– Blood circulates more orderly                → Flow turbulence is reduced</li> </ul>	<ul style="list-style-type: none"> <li>– Recent research investigated the intra-ventricular flow during LVAD support by comparing a measured flow pattern using particle image velocimetry with different flow patterns obtained from simulation. The obtained results suggest that the laminar model presented acceptable similarity to experimental data and showed the best transient behaviour (Ghodrati et al., 2021)</li> </ul>
<b>AoV closed or not modelled</b> (Chivukula et al., 2020) (Chivukula et al., 2018) (Sonntag et al., 2019) (McCormick et al., 2013) (Ong et al., 2013) (Liu et al., 2012) (Fraser et al., 2010) (Rojano et al., 2021)	<ul style="list-style-type: none"> <li>– Sub-aortic region becomes potentially a stagnation zone</li> <li>– Sub-aortic dynamics and its influence on the ventricle are neglected</li> </ul>	<p>The region of interest: apical region of the ventricle (near the IC)</p>
<b>Geometry: single patient/ healthy LV / idealized/simplified</b> (Chivukula et al., 2020) (Chivukula et al., 2018) (Liao et al., 2018) (Prisco et al., 2017) (McCormick et al., 2013) (Ong et al., 2013) (Ong et al., 2012) (Liu et al., 2012) (Tsukiya et al., 2011) (McCormick et al., 2011) (Fraser et al., 2010) (McCormick et al., 2009) (Rojano et al., 2021)	<ul style="list-style-type: none"> <li>– No statistical data</li> <li>– No generalisation to all VAD patients</li> <li>– Localized stress distribution neglected</li> </ul>	<ul style="list-style-type: none"> <li>– Clinical data available</li> <li>– Computation time and resources</li> </ul>
<b>Model not validated</b> (Chivukula et al., 2020) (Ghodrati et al., 2020) (Sonntag et al., 2019) (Liao et al., 2018) (Chivukula et al., 2018) (Prisco et al., 2017) (McCormick et al., 2013) (Ong et al., 2013) (Ong et al., 2012) (Liu et al., 2012) (Tsukiya et al., 2011) (Fraser et al., 2010) (McCormick et al., 2009) (Rojano et al., 2021)	<ul style="list-style-type: none"> <li>– Not relevance of the obtained results</li> </ul>	<p>Validation could be done by comparing the obtained results to clinical data which is not always possible.</p>

**Table 2.2:** Overview of the main CFD models limitations encountered in the literature.

LV = Left Ventricle; AoV = Aortic Valve; IC = Inflow Cannula; VAD = Ventricular Assist Device; LVAD = Left Ventricular Assist Device

## 2.5 Summary and Work positioning

In the context of MCS implantation, VAD is cannulated to the ventricle to assist its functioning. The most commonly implanted VAD are the LVAD. LVAD implantation implies morphological, fluid and mechanical changes. These physiological changes are caused by the interaction of the device with the ventricular and arteries haemodynamics and the surrounding organs. It should be noted that if our analysis focuses on LVAD, the same logic can be applied on RVAD and BiVAD as well.

In the literature, the influence of LVAD devices on blood flow considered three main topics: i) the impact of inflow cannula insertion on ventricular haemodynamic, ii) the impact of outflow cannula insertion on the arteries haemodynamic, iii) the pump efficiency. We focus on the IC since related works are limited and surgeons have less information about this part of the device. The interaction of IC features (tip, angulation and length) with the ventricle, may alter LV haemodynamic. Reported works, attempted to link this ventricular alteration to thromboembolic complications. Hence, Researches took interest in the impact of IC features on the LV haemodynamic and attempted to evaluate the associated thrombosis risk.

Thrombus formation is a complex phenomenon involving blood stagnation and platelet activation, not fully understood. Using CFD computation, reported work considered several QOI to analyse the influence of IC features on LV haemodynamic and attempted to assess blood stagnation, platelet activation and thrombosis risk. Yet, their evaluations and the impact of IC angulation on LV haemodynamic remain challenging; the question to how should these QOI be exploited to evaluate thrombosis risk, remain unanswered.

Among IC features, IC angulation is the main focus of our investigation. Unlike IC tip and IC length that depend on the LVAD design, a deviation of the IC toward the IVS may occur at one point of the surgical procedure. Since some LVAD brands propose two different IC lengths, IC length will also be considered in our work.

This Ph.D. dissertation aims to understand the haemodynamic changes that occur due to IC features (angulation and length) and to develop a thrombogenic marker able to evaluate thrombosis risk related to a specific configuration. Our work positioning is depicted in Figure 2.6.

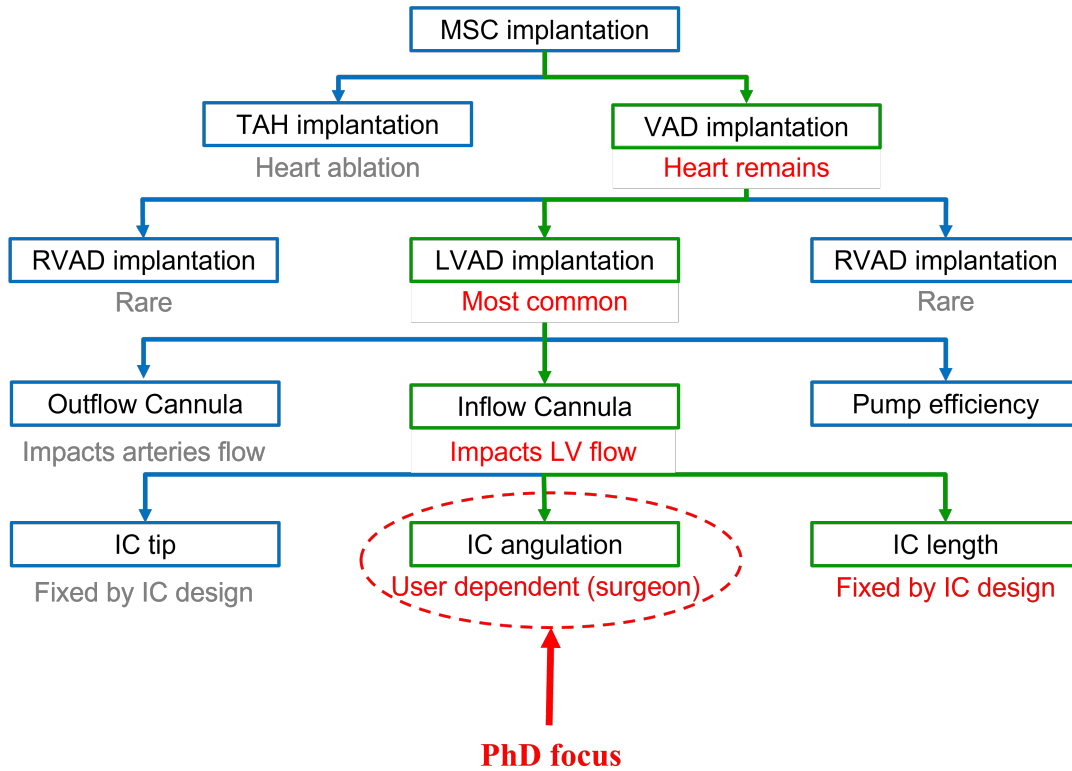


Figure 2.6: Work positioning.

# Model definition for haemodynamics analysis

In this chapter, a simplified CFD model is proposed to investigate the influence of IC features (IC angulation and length) on LV haemodynamic aiming to identify the main factors involved with thrombosis.

The chapter is composed of three sections. In the first section, a 3D approach is held as a reference to the 2D approach introduced in the second section. In the third section, a 2D model is proposed and used to investigate the influence of different IC features on the LV haemodynamic.

## 3.1 3D approach

The main purpose of the 3D approach is to be used as a first step and a reference to the elaboration of the proposed model.

### 3.1.1 Model Presentation

In order to evaluate the influence of IC angulation on LV haemodynamic, blood stagnation, platelet activation and thrombosis risk, a simplified 3D model is developed and implemented. The geometrical, numerical models and the QOI are presented in the following.

**Geometrical Model:** This 3D approach focuses on the haemodynamics changes that occur within the LV due to IC angulation. A generic 3D approach is considered. When investigating the ventricular haemodynamic, reported studies did not represent the AoV or considered it closed (Chivukula et al., 2020, 2018; Fraser et al., 2010; Liu et al., 2012; McCormick et al., 2013; Ong et al., 2013; Rojano et al., 2021; Sonntag



et al., 2019). Since most HF patients are diagnosed with reduced ejection fraction HF, the amount of blood ejected from the LV through the AoV is reduced. In this model, the AoV is not represented and a simplified representation of the regions of interest (MV, LV and IC) is considered. Since the LV geometry is simplified, and mechanical valves prostheses have a circular shape, the MV was represented by a circle.

The proposed geometrical model is defined as follows (Figure 3.1). The LV is depicted as a prolate ellipsoid of revolution, the MV as a circle and the IC as a cylinder. The LV is defined by the short axis, Left Ventricle - Diameter (LV-D) and the long axis, Left Ventricle - Height (LV-H). The MV is defined by the Mitral Valve long Diameter (MV-D). The IC is defined by the Inflow Canula Diameter (IC-D), the Inflow Canula Length (IC-L), the Inflow Canula Angular Deviation (IC-AD) from the LV long axis and the IC surface, an IC tip at the cross-section, where the blood exits the LV and enters the IC. Thereafter, we will use the term IC angulation to refer to IC-AD.

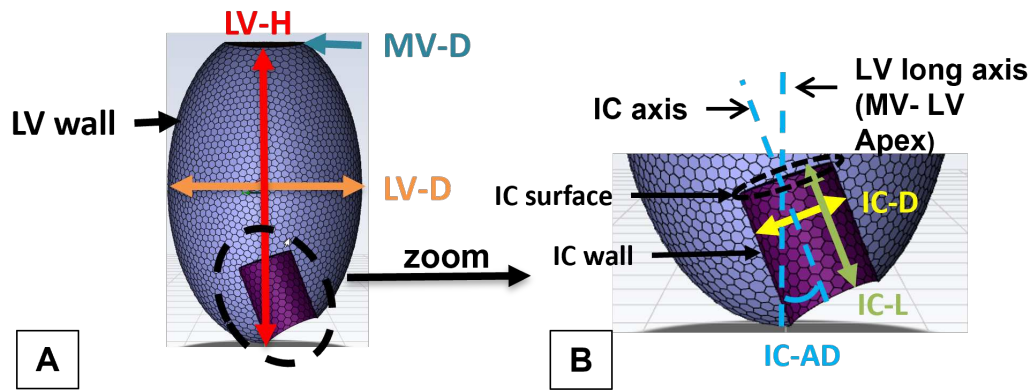


Figure 3.1: Model definition, with LV features (A) and IC features (B).

For the LV geometrical model, two cases (C3 and C14) are considered (Table 3.1). These cases are selected based on their LV features. Both ventricles are not dilated ( $LV-D < 55 \text{ mm}$ ). Both ventricular shapes ( $LV-D/LV-H$  ratio) are similar ( $\approx 0.58$ ) and the Flow Rate ( $Q$ ) of both pumps are similar and considered average  $Q$  used for LVAD patients. The main difference between these two cases lies in a significant volume difference (almost doubled).

Case	LV-D (mm)	LV-H (mm)	VM-D (mm)	LV volume ( $10^{-5} \text{ m}^3$ )	$Q$ ( $\text{L} \cdot \text{min}^{-1}$ )
C3	50	87	34	11.95	5
C14	42.2	71.9	27.5	6.73	5.2

Table 3.1: Investigated cases.

For the IC geometrical model, we considered the IC of the HM2 LVAD (Table 3.2). For each investigated case, two IC angulations are considered:

- IC0: where the IC is facing the MV as recommended by the clinical guidelines

(IC-AD = 0°).

- IC20: where the IC has a 20° deviation from the MV toward the IVS (IC-AD = 20°). This is a plausible deviation that is likely to occur during LVAD implantation.

Pump	IC-D (mm)	IC-L (mm)
HM2	18	20

**Table 3.2:** HM2 pump properties.

**Numerical model:** Once the geometry is designed then meshed, the following step consists of defining the boundary conditions and the physiological parameters. The IC wall is considered a rigid material. Analyses of LV wall motion confirm minimal changes in typical patients with LVAD devices suffering from severe systolic dysfunction and markedly impaired contractile reserve (Chivukula et al., 2018). Hence, the LV wall is assumed to be a rigid material. A uniform velocity inlet is prescribed at the MV (corresponding to a constant  $Q \text{ L} \cdot \text{min}^{-1}$ ; mathematical details are available in Appendix C). A constant static pressure (0 Pa) outlet is set at the IC surface. Blood is modelled as a Newtonian fluid with a density of  $1060 \text{ kg} \cdot \text{m}^{-3}$  and a viscosity of  $0.004 \text{ kg} \cdot \text{m}^{-1} \cdot \text{s}^{-1}$  (Herman, 2010).

The flow within the ventricle is known to be turbulent. Since a turbulent flow is not obvious to simulate, most recent works considered the laminar assumption (Chivukula et al., 2020; Entezari et al., 2021; Ghodrati et al., 2020; Liao et al., 2018; Prisco et al., 2017). In this context, (Ghodrati et al., 2021) took interest in the flow pattern within the ventricle during LVAD support. They compared experimental measures of the intraventricular flow patterns using particle image velocimetry, with CFD simulation results of laminar and different turbulent flow regimes. Although all simulations results under-predicted the velocity variations over time, the laminar flow regime showed the most similar behaviour to experimental measures. In our work, the flow is assumed laminar.

We introduced a virtual blood dye within the ventricle as an indicator of LV wash-out. This technique consists in filling completely the LV volume with a virtual ink that dyes the blood. The dye is washed-out from the LV volume during a specific period, the remaining dye is expressed via a variable called Remaining Ink Concentration (RIC). In CFD simulation, the transport of virtual ink is described via a passive scalar with zero flux at the walls. It is governed by the underlying blood flow patterns and does not influence the blood flow. The diffusion of the virtual ink is disabled, so that its clearance is determined purely by advection (Prisco et al., 2017). The dying technique is divided into 3 phases (Figure 3.2):

- Initialization phase (Ip): is a fixed time-period during which the ventricle is filled with blood. This phase aims to guarantee a fully developed flow field.
- Filling phase (Fp): This phase aims to fill the ventricle with the virtual ink till its concentration reaches 1, meaning that the LV volume is 100% filled with dyed blood. This time-period depends on the LV shape and boundary conditions.
- Clearing phase (Cp): This phase aims to washout the virtual dye from the ventricle. Depending on the investigation interest, the choice of this time-period can be fixed at a given value or a value proportional to the Fp.

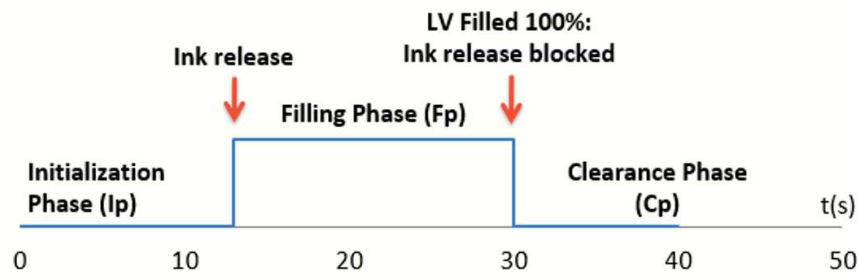


Figure 3.2: Phases of virtual ink technique.

For virtual ink phases,  $I_p$  is set empirically to 13 s. In this section, as RIC is used to compare ventricular washout between two IC angulations (IC0 and IC20),  $C_p$  is empirically set to a fixed value of 4 s.

In CFD simulations, the Navier-Stokes equations are solved at each iteration. The number of iterations is set by the Time step ( $T_s$ ) as one iteration represents one increment of  $T_s$ . The choice of the time step is crucial as it directly influences the computation time: the lower the time step, the higher the computation time.  $T_s$  value depends on the size of the mesh elements: the finer the mesh, the higher the time step. The time step is set according to the Courant-Friedrichs-Lewy (CFL) condition:

$$c = \frac{v\Delta t}{\Delta x} \leq 1 \quad (3.1)$$

where  $c$  is called the courant number,  $v$  is the velocity magnitude,  $\Delta t$  is the  $T_s$  and  $\Delta x$  is the cells size.

Before defining  $T_s$ , a mesh independence study was performed. It is held to ensure that the simulation results are independent of the underlying mesh. Progressively finer mesh of 22 k, 32 k and 155 k polyhedral cells corresponding to meshes with elements sizes of 3 mm, 2 mm and 1 mm respectively, were investigated. The used metrics were the max and mean values of velocity magnitude as velocity is a main feature to evaluate flow within the LV. According to the study results, the analysis had indicated that the mesh independence was reached for a mesh with 2 mm ele-

ment size with a  $Ts$  of  $10^{-5}$  s, according to CFL condition. The mesh independence study is detailed in Appendix D.

The CFD simulation is performed using a second order implicit transient formulation, and a Pressure Implicit with Splitting of Operators (PISO) solver with a pressure-velocity coupling. A second order spatial discretization is set for the pressure, momentum, and continuity equations. Convergence was achieved in each time-step, when the residuals are below  $10^{-6}$  for continuity, x, y, z velocities and the virtual ink as required by the pressure-based solver. Figure 3.3 summarizes all the numerical settings of the CFD simulation. Simulations were performed using ANSYS FLUENT 2021 R2.

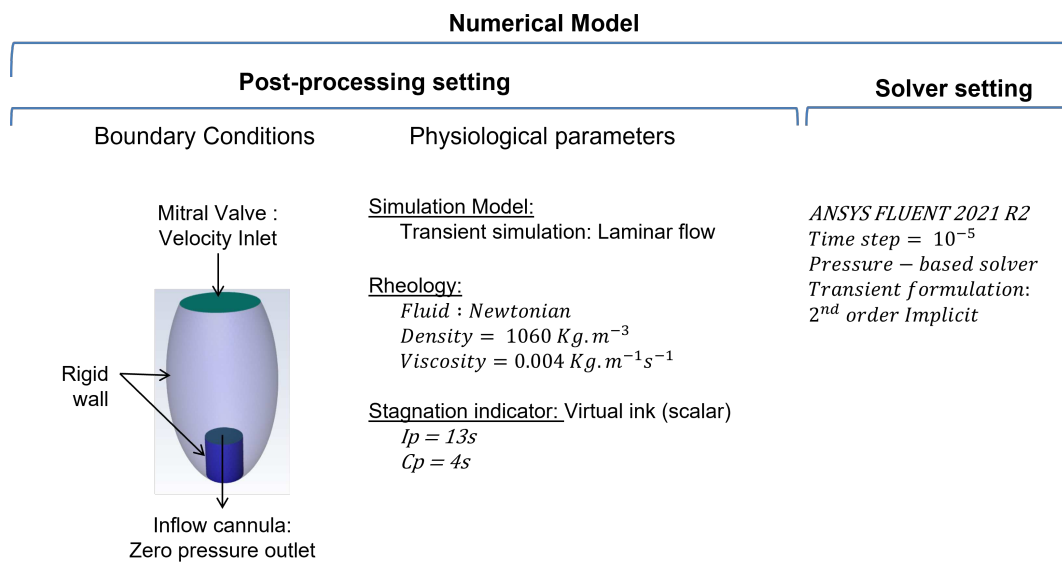


Figure 3.3: 3D approach: Numerical Model.

**Thrombogenic analysis:** CFD simulations are used to analyse the influence of IC angulation on LV haemodynamic. This analysis is performed through Quantities Of Interest (QOI) likely to be involved in the risk of thrombosis.

In the following, we propose an analysis grid of thrombogenic factors, where QOI used to evaluate blood stagnation and platelet activation are based on previously reported work. Table 3.3 illustrates the analysis grid for interpreting the QOI with regard to the risk of thrombosis. It is composed of QOI coloured in red or in green according to their potential to favour (+) or not (-) blood stagnation and platelet activation. The grid is illustrated for previously presented configurations (LV shapes and IC angulations).

Blood stagnation is identified by low velocity regions with high RIC. Velocity path-lines and magnitude are used to identify low velocity regions. They are considered as low velocity re-circulation regions with low velocity magnitude. No explicit low

				Thrombogenic analysis	
				Least	More
Thrombogenic factors	Blood Stagnation	Velocity pathlines		More direct (-)	Spiralling (+)
		Low velocity regions		Narrow regions (-)	Extended regions (+)
		RIC	Maximal Value	$\leq 0.5(-)$	$\geq 0.5(+)$
			Distribution	Local (-)	Wide (+)
	Platelet Activation	WSS maximal value		$\leq 3.5 \text{ Pa} (-)$	$[3.5, 5] \text{ Pa} (+)$ $> 5 \text{ Pa} (++)$
		WSS Distribution		Low values around stagnation regions (-)	High values not around stagnation regions (+) High values around stagnation regions (++)

**Table 3.3:** QOI reading grid for thrombogenic analysis.

velocity threshold is defined in the literature. It could be defined by considering a threshold relative to the maximal value to take into account the variability between different ventricles. A relative value of 5% is considered. RIC is assessed by its distribution, qualified as local or wide, and its maximal values considered high when it is equal to or higher than 50% of its initial concentration ( $\text{RIC} \geq 0.5$ ) as advocated by (Prisco et al., 2017).

Platelet activation is stimulated via Von Willebrand Factor (vWF) multimers under a high shear stress:  $\tau \geq 3.5 - 5[\text{Pa}]$  (Hellmuth et al., 2016). WSS is assessed by its maximal value and distribution. In the analysis grid, WSS maximal value could be noted with (+) or (++) signs when its maximal value is within or above the platelet activation interval ( $[3.5 - 5]\text{Pa}$ ), respectively. When WSS is above the platelet activation range, activated platelet might aggregate and the size of the aggregated platelet is regulated through shear intensity (Hellmuth et al., 2016). The distribution of the WSS is also noted with (+) and (++) signs depending on whether the high values of the WSS are found around blood stagnation regions or not, as stagnation regions enhances activated platelet deposition and accumulation.

### 3.1.2 Results

Figure 3.4 presents the simulation results for C3 and C14 for both IC angulations. For both cases, the velocity profile is laminar at the centre of the LV. The highest velocity is found within the cannula tip. The velocity is slightly higher when the IC is deviated (IC20). Outside the central jet, low velocity and recirculating flow are observed where the blood spirals slowly around the inflow cannula before exiting the ventricle, especially for IC20, this characterises low velocity regions.

RIC is located at the apex and along LV wall, for C14. Its maximal values are low for

		IC0	IC20	
Thrombogenic factors	Blood Stagnation	Velocity pathlines	-	+
		Low velocity regions	+	+
	RIC	Maximal Value	+	-
		Distribution	+	-
	Platelet Activation	WSS maximal value	++	++
		WSS distribution	++	+
Qualitative score		+	+	

**Table 3.4:** QOI reading grid of both IC angulations for C3.

both IC angulations, especially for IC20. For C3, RIC is high for IC0, it is located at the apex and especially along LV wall where low velocity regions are formed. In this configuration, low velocity regions with high RIC are considered blood stagnation regions, as defined previously. For IC20, RIC is low and is located mainly along the LV wall. For both cases, IC20 has a better washout than IC0.

WSS is located at the MV, the IC wall and the LV wall around the IC region. For both cases, it reaches locally high values. For C14, WSS is within the platelet activation interval for both IC angulations. For IC0, high values of WSS are observed around the MV. WSS is low around apical region. For IC20, areas where the WSS is high are observed around the MV and the IC tip. For C3, high values WSS, above the platelet activation interval, are located around the MV and the IC tip. For IC0, WSS reaches higher values than for IC20. These high values are located at the IC tip, around blood stagnation region. This might enhance activated platelet deposition and accumulation. For IC20, areas where WSS is high are located especially around the IC tip.

A summary of the QOI analysis for C3 and C14, respectively, is illustrated in Table 3.4 and Table 3.5. For C14, IC angulation influences velocity path-lines and WSS distribution. Velocity path-lines become spiraling around the IC before exiting the LV which may have enhanced the constraints at the IC tip. For C3, IC angulation influences velocity path-lines, RIC and WSS distribution. Although velocity path-lines are spiraling around the IC for IC20, the ventricle has a better washout of the virtual ink. This reflects a lower residence time of blood particles within the ventricle, thus less exposure time to high constraints at the IC tip.

### 3.1.3 Discussion

The influence of IC angulation on LV haemodynamic can be analysed by considering several QOI. In this preliminary study, we noticed that the influence of IC on ventricular haemodynamic was more significant for C3 than for C14.

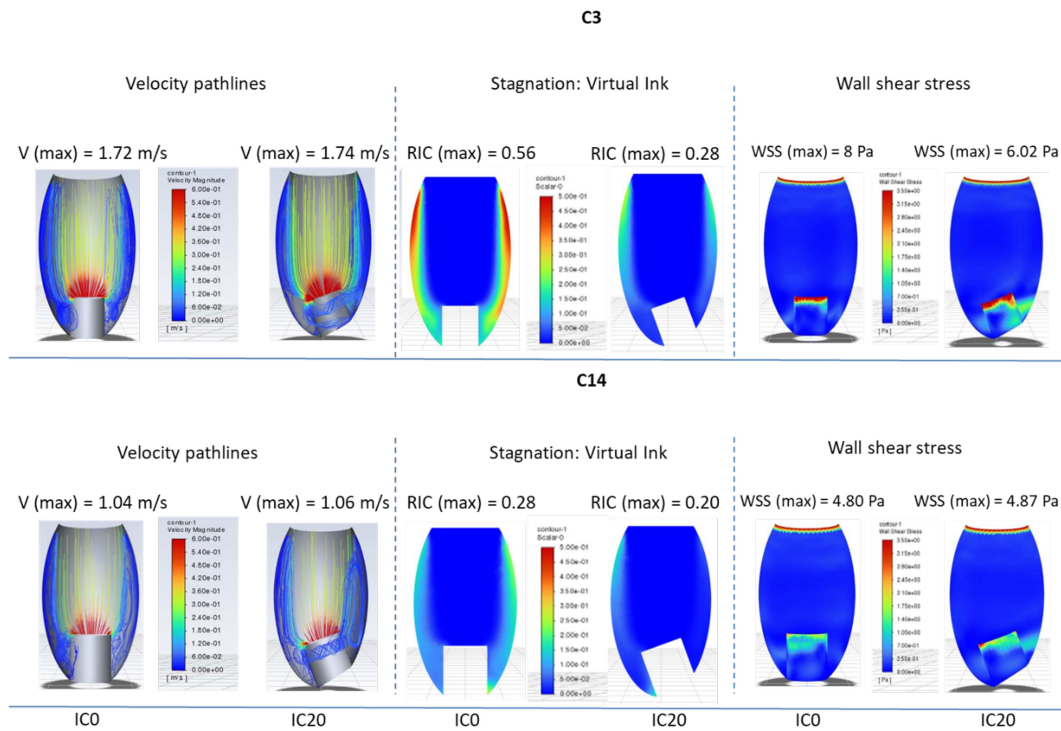


**Figure 3.4:** CFD simulation results for C3 (top) and C14 (bottom) for both IC angulation 0° (IC0) and 20° (IC20).

For C3, QOI analysis suggested that IC0 configuration enhanced blood stagnation regions. These regions were also exposed to high shear stress which might favour activated platelet deposition and accumulation. For IC20, no such regions were identified and RIC results suggested a better ventricular washout. For C14, blood stagnation analysis revealed no specific region where blood is likely to stagnate for both angulations and platelet activation analysis tended to favour IC0 as no high WSS values were observed around the apical region which is claimed to be a stagnation region.

The grid analysis showed differences between the configurations. At this level of analysis, it would be interesting to study several QOI, especially as they seem influenced by IC angulations. Since this influence provides additional information, their analysis is relevant and might help to understand LV haemodynamic which is the main interest of this chapter. Nevertheless, this grid is not sufficient to evaluate thrombosis risk, as the distributions of the QOI were sensitive to qualify resulting in a subjective qualitative score.

Despite limitations, obtained results allowed to observe the influence of IC angulation on LV haemodynamic by considering several QOI. Yet, this influence did not affect the ventricular haemodynamic within both investigated LV shapes (C3 and C14) equally. IC angulation influenced differently the QOI for both ventricular shapes that resulted in favouring different IC angulations. LV shape appears to be an influenc-

			IC0	IC20	
Thrombogenic factors	Blood Stagnation	Velocity pathlines	-	+	
		Low velocity regions	-	+	
		RIC	Maximal Value	-	-
			Distribution	-	-
	Platelet Activation	WSS maximal value	+	+	
		WSS distribution	-	+	
Qualitative score			-	+	

**Table 3.5:** QOI reading grid of both IC angulations for C14.

ing factor of LV haemodynamic that ought to be considered while investigating the influence of IC angulation. Although results allowed to observe that IC angulation does influence the QOI behaviour, only two angulations are not sufficient to understand the behavior and evolution of the QOI according to IC angulations as well as their impact on LV haemodynamic. The main limitation comes from the 3D models that require high resources and computation time (around 21 days with an Intel(R) Xeon(R) Gold 5220 CPU @ 2.20 GHz and 2.19 GHz , respectively (2 processors), RAM: 64 Gb and NVIDIA Quadro P400) which prevents the investigation of a wide range of IC angulations and LV shapes. In the next section, the assumption of using 2D models to investigate LV haemodynamic is carried out.

## 3.2 2D assumption

Although they have limitations, 2D models have the potential to reduce the complexity of the analysis. They also have the advantage of an easy implementation and a fast computation time, allowing a wide ranging investigations. This may allow a better understanding of the influence of the IC angulation on the LV haemodynamic and on the QOI behaviour.

2D approach might be interesting, the assumption that a 2D model is able to grasp the impact of IC angulation on ventricular haemodynamic ought to be checked. This is the focus of this section. This investigation consists in proposing a 2D geometry, then, analysing whether the evolution of QOI regarding IC angulation have the same tendency for 2D compared to 3D models.

### 3.2.1 Model presentation

In the following, a 2D model is presented. The geometrical model details the developed geometry and the investigated cases while the numerical model details the



settings and boundary conditions of the CFD simulation. To evaluate LV haemodynamics, we used the QOI defined in the previous section: velocity path-lines, velocity magnitude, RIC and WSS.

**Geometrical Model:** The proposed 2D geometry is a simplified representation of the anatomical regions of interest. It is obtained at the centre plan of the 3D geometry (Figure 3.5). The LV is represented by an ellipse cropped by the MV and the IC is represented by a rectangle (Figure 3.6). The LV is defined by its short axis (LV-D) and its long axis (LV-H). The MV is defined by its long diameter (MV-D). The IC is defined by its diameter (IC-D), length (IC-L), angular deviation from the LV long axis (IC-AD) and its IC surface. Although, named IC surface, it is defined by a segment at the upper short side of the rectangle, where blood exits the LV and enters the IC. More details will be presented in the following.

Both LV and IC properties as defined in (Table 3.1) and (Table 3.2) are adapted to the 2D model definition. For each investigated case (C3 and C14), two IC angulations were also considered (IC0 and IC20).

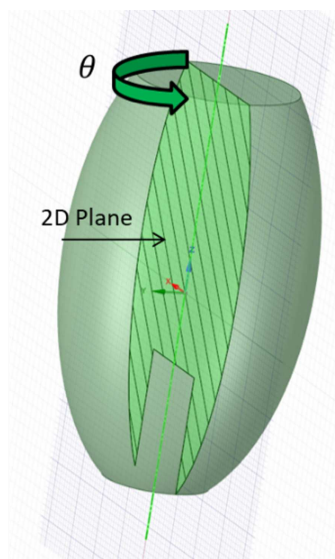


**Figure 3.5:** Relationship between 2D and 3D models.

**Numerical Model:** Once the geometry is designed then meshed, the boundary conditions and the physiological parameters are also defined identically to the 3D approach. The LV and the IC walls are considered rigid materials. A uniform velocity inlet is prescribed at the MV (corresponding to a constant flow rate  $Q$  [ $\text{L}\cdot\text{min}^{-1}$ ]; Appendix C). A constant static pressure ( $0 \text{ Pa}$ ) outlet is set at the IC surface. Blood was modelled as a Newtonian fluid with a density of  $1060 \text{ kg}\cdot\text{m}^{-3}$  and a viscosity of  $0.004 \text{ kg}\cdot\text{m}^{-1}\text{s}^{-1}$  (Herman, 2010) and flow is considered laminar.

Concerning the virtual ink phases,  $I_p$  is set to 13 s. Since we aim to compare the 2D

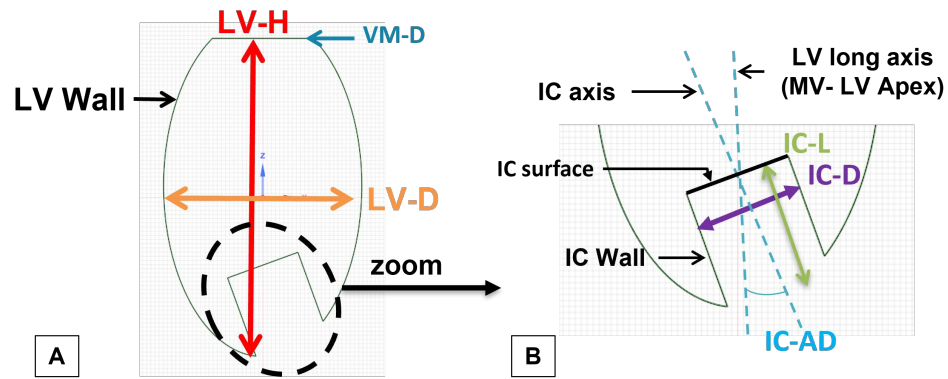


Figure 3.6: Model definition with LV features (A) and IC features (B).

and 3D approaches to check whether the impact of IC angulation on LV haemodynamics has the same tendencies,  $C_p$  is set proportionally to the filling time  $F_p$  ( $C_p = 20\%$  of  $F_p$ ) to ensure that both approaches are compared in the same condition.

Regarding the simulation parameters, the time step used in the simulation is  $10^{-3}$ s which ensured  $CFL < 1$  condition. A mesh independence study was performed on a progressively finer mesh of 0.8k, 1.8k and 7k, 27k nodes corresponding to a mesh with elements sizes of 3 mm, 2 mm, 1 mm and 0.5 mm, respectively. As for the previous mesh independence study, the investigated metrics are the max and mean velocity magnitude. This study indicated that a mesh with elements size of 2 mm is considered sufficient to achieve a balance between accuracy and computational cost. The mesh independence study is detailed in Appendix E.

For 2D simulations, the software imposes a definition of the model thickness to achieve computations (specific to the software) such as areas and flow rate computations. Since the IC is the main focus of this study, we defined a thickness that allows to reproduce the IC cross-section surface in order to approach a more realistic output flow rate. It is important to note that even if a thickness is specified, the simulation remains two dimensional. More details concerning the thickness choice and definition are presented in Appendix F.

A second order implicit transient formulation, and a PISO solver with a pressure-velocity coupling is also chosen. A second order spatial discretization is performed for the pressure, momentum, and continuity equations. Convergence was achieved in each time-step ( $10^{-3}$  s) when the residuals are below  $10^{-6}$  for continuity, x, y velocities and the virtual ink as required by the pressure-based solver. Figure 3.7 summarizes all the numerical setting of the CFD simulation.

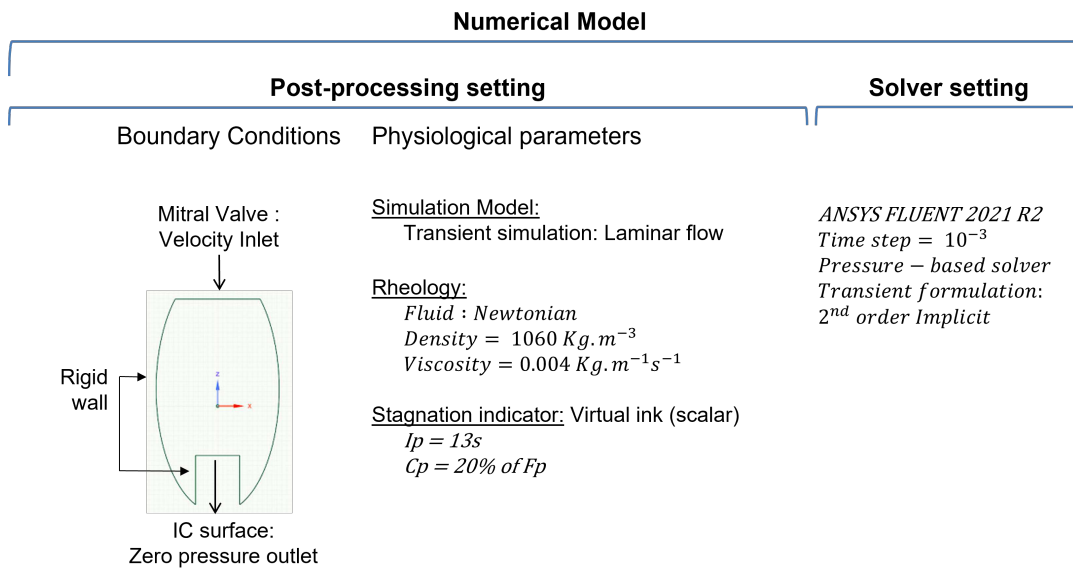


Figure 3.7: 2D assumption: Numerical model.

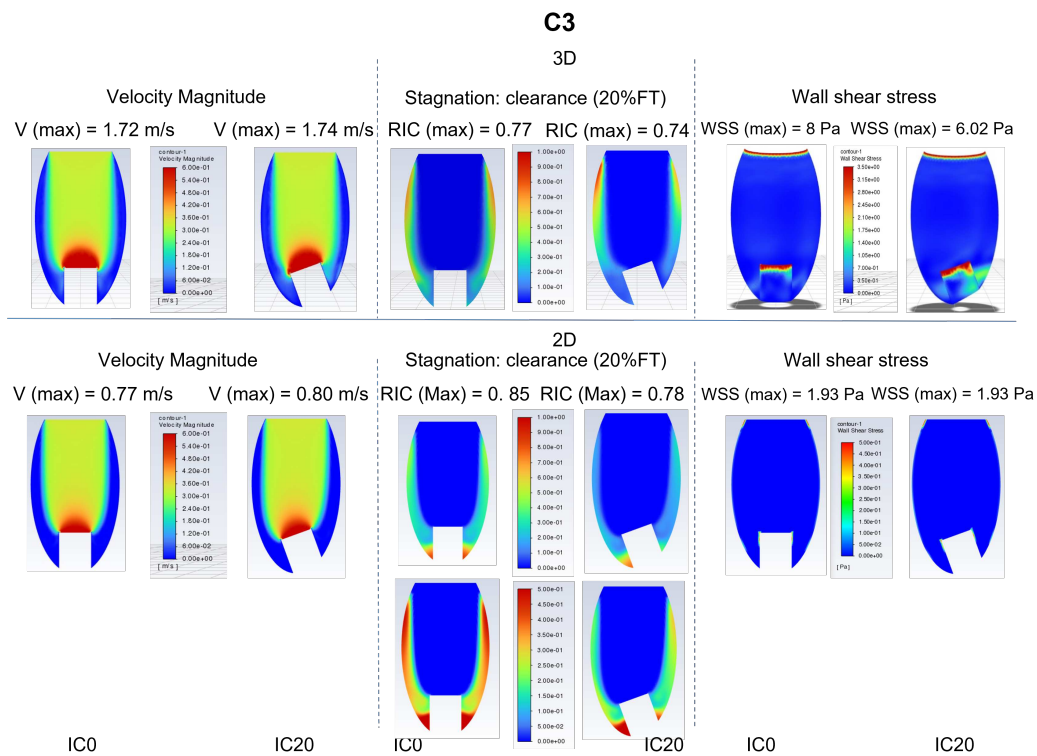


Figure 3.8: Simulation results for C3 in 3D (top) and 2D (bottom).

### 3.2.2 Results and discussion

Figure 3.8 and Figure 3.9 illustrate the comparison between the 3D and 2D results for both configurations (IC0 and IC20) for C3 and C14 respectively. For 2D and 3D simulations, the velocity profile is laminar with a mean velocity of 34 m.s<sup>-1</sup> in the central jet and a reduced velocity within the LV wall and apex. The velocity mag-

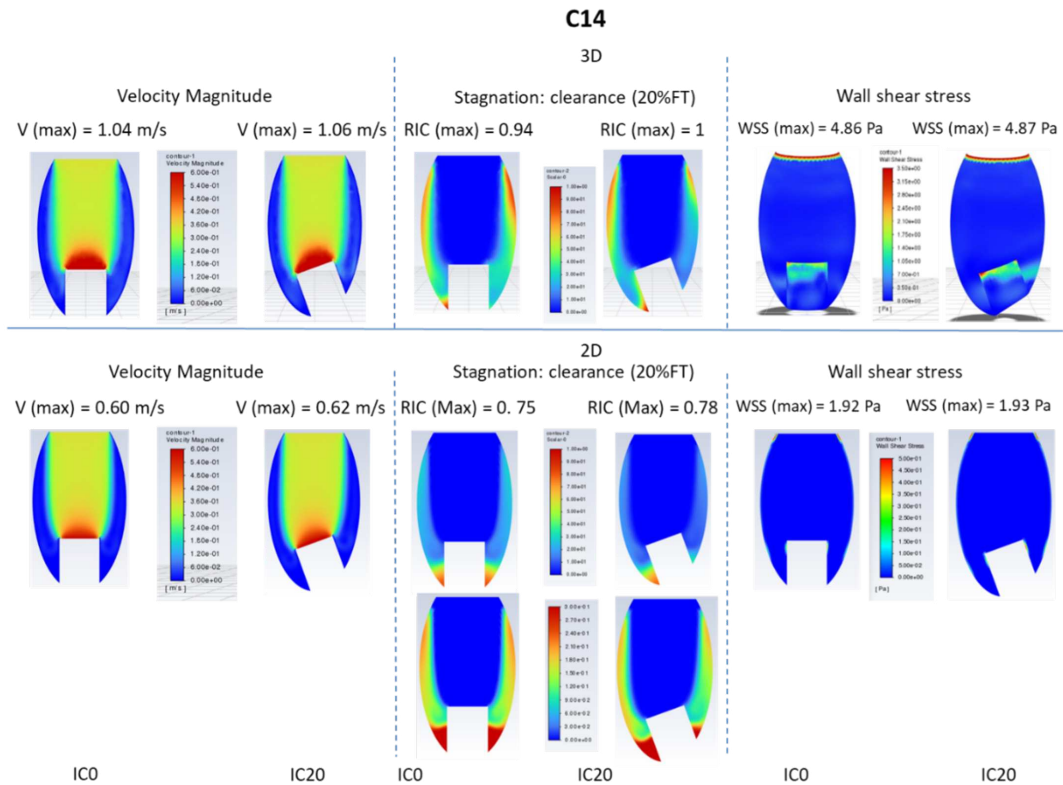


Figure 3.9: Simulation results for C14 in 3D (top) and 2D (bottom).

nitude reaches its maximum around the IC. The velocity is slightly higher for IC20 ( $+0.02 \text{ m}\cdot\text{s}^{-1}$ ). Vortices along LV wall till the apex are observed, on both sides of the IC. In these vortices, blood hits the apex and then flows upward along the ventricular wall (surrounding the IC for IC20) for 3D simulations. This phenomenon is absent in 2D simulation due to the lack of depth. Nevertheless, these vortices are still present on both side of IC for 2D models. The same low velocity regions (recirculation regions with low velocity) could also be observed in 3D and 2D models. They are located at the apex and along LV wall. These regions may be formed due to the central jet that prevent blood within these regions from being drawn into the IC.

For 3D and 2D simulations, the RIC is located at the apex and within the LV walls. However, its concentration is more present close to the LV walls for 3D simulations and at the apex for the 2D simulations. This could be explained by the lack of depth (the 3<sup>rd</sup> dimension) that prevents the virtual ink from being distributed and flow upward along the LV wall, hence the virtual ink tends to concentrate in the apical region due to its narrowness. One can observe that at a reduced scale, similarities could be observed in RIC distribution between 3D and 2D models. Concerning RIC maximal values, although maximal values are reduced for 2D models, RIC behaviour regarding IC angulation have the same tendency as 3D models where the RIC is higher for IC0 for C3 and for IC20 for C14. High RIC values are located within low velocity

regions where blood eventually stagnates. These regions are present in 3D and 2D models, where the apical region represent a common region prone to stagnation for 2D and 3D models, except for C3 with IC20 in 3D model. These observations are consistent with results found in the literature (Ghodrati et al., 2020; Prisco et al., 2017).

WSS distribution in 2D simulations is similar to the one obtained in 3D simulations for a reduced scale. WSS is located at the MV, the IC tip and the LV wall, especially around the IC. Higher values of WSS present in 3D model could be explained by the flow constraints: the flow is enclosed within the ventricle for 3D models.

2D models tend to underestimate WSS. Nevertheless, the WSS distribution has the same tendency for 3D and 2D models. For instance, for C14, WSS distribution between both angulations, especially at the cannula tip is coherent between both models.

### 3.2.3 Conclusion

In order to investigate the 2D assumption, we compared the QOI behaviour regarding IC angulation for two 3D models and their corresponding 2D models.

Although 2D models have limitations, the behaviour of the QOI obtained for both IC angulations show similar trends for 2D and 3D simulations. The use of 2D models is interesting as analysing the behaviour of QOI regarding a wide range of IC angulation may allow a better understanding of the LV haemodynamic. The advantage of a fast computation, allows to expend the investigations to another feature such as IC length. In the next section, the influence of IC features (IC angulation and length) are investigated using 2D models.

## 3.3 2D proposed approach

The focus of this study is the influence of IC angulation and length on LV haemodynamic. This analysis considers a wide range of IC angulation and IC length combined with a slight angulation for two ventricular shapes. For that a straightforward analysis of QOI is performed. Since our main focus is the IC, an adaptation of the boundary conditions of the 2D model is proposed to more accurately represent the interaction of the device with the ventricle.

### 3.3.1 Numerical model: inlet / outlet

The numerical model presented in the following is applied to the 2D geometrical model proposed in the previous section. Blood is considered as a Newtonian fluid with a density of  $1060 \text{ kg}\cdot\text{m}^{-3}$  and a viscosity of  $0.004 \text{ kg}\cdot\text{m}^{-1}\cdot\text{s}^{-1}$ , the flow is laminar, and LV and IC walls are considered rigid. Concerning the virtual ink phases,  $I_p$  is empirically set to 13 s and  $C_p$  is set to 12 s as proposed by (Prisco et al., 2017). In

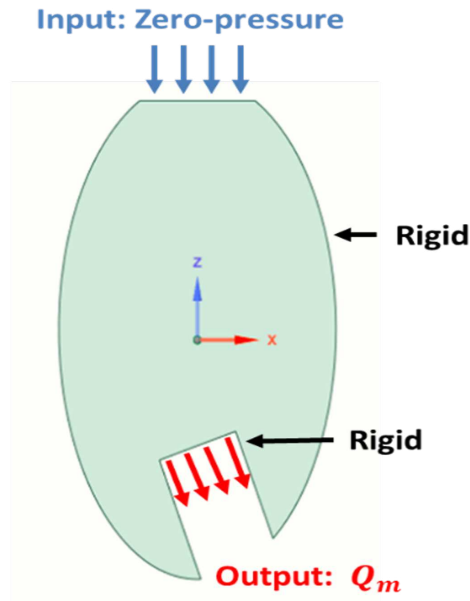


Figure 3.10: 2D model: Input / output.

this section, the boundary conditions were adapted to impose an output condition on the IC surface. The imposed output is a mass flux ( $\text{kg}\cdot\text{m}^{-2}\cdot\text{s}^{-1}$ ) that reflects the pump flow rate  $Q$  ( $\text{L}\cdot\text{min}^{-1}$ ) which is the only parameter that could be monitored by clinicians once the LVAD is implanted. The conversion from flow rate to mass flux is obtained according to the equation 3.2. The input is imposed as a zero-pressure inlet at the MV. A summary of the model boundary conditions is illustrated in Figure 3.10.

$$Q_m[\text{kg}\cdot\text{m}^{-2}\cdot\text{s}^{-1}] = \frac{\varphi \times Q}{60 \times 1000 \times s} \quad (3.2)$$

where  $\varphi$  is the blood density  $\text{kg}\cdot\text{m}^{-3}$ ,  $Q$  is the flow rate of the pump  $\text{L}\cdot\text{min}^{-1}$  and  $s$  is the surface of the IC output  $\text{m}^2$ .

The solver settings remain unchanged. The time step is  $10^{-3}$  s. A second order implicit transient formulation, a PISO solver with a pressure-velocity coupling were also chosen. A second order spatial discretization was performed for the pressure, momentum, and continuity equations. Convergence was achieved in each time-step when the residuals were below  $10^{-6}$  for continuity, x, y velocities and the virtual ink. Figure 3.11 summarizes all the numerical settings of the CFD simulation. This proposed 2D approach is used from this point onward.

### 3.3.2 Influence of inflow cannula angulation

The aim of this section is to have a better understanding of the influence of IC angulation on LV haemodynamic. A wide range of IC angulation is considered:  $[0^\circ, 90^\circ]$

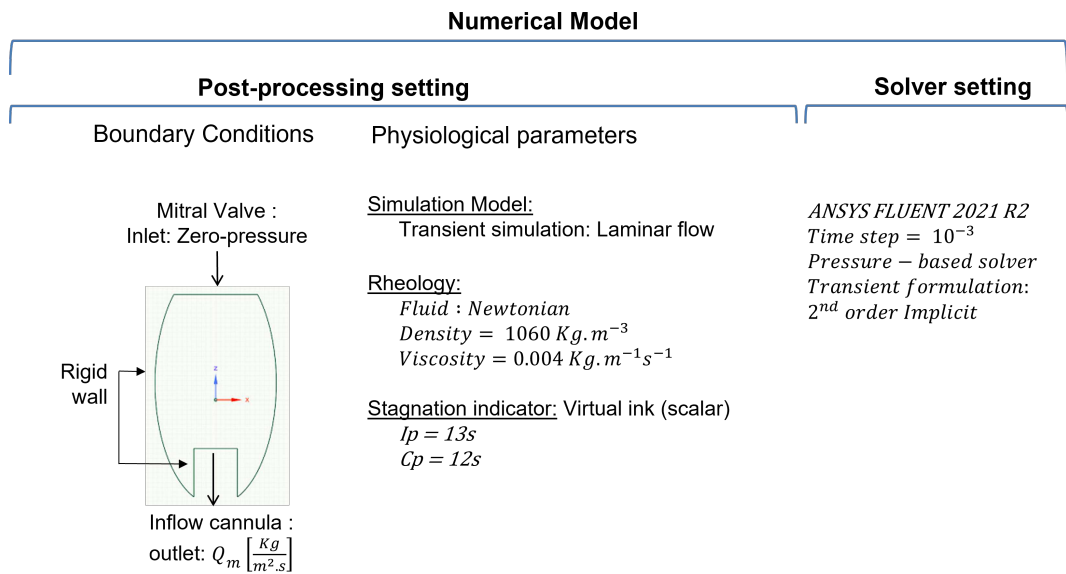


Figure 3.11: Proposed Numerical Model.

where the IC is progressively deviated toward the IVS with a step of  $10^\circ$ . This investigation is held on two distinct cases (C3 and C14), previously presented in Table 3.1.

Figure 3.12 and Figure 3.13 present the velocity path-lines for C3 and C14 respectively where the velocity magnitude within the ventricle is higher for C14 than for C3. For both LV shapes, as the IC angulation increases, the maximum velocity within the ventricle, especially close to the IC, increases. We can notice that the region, where the flow is drawn into the IC and the velocity reaches its peak, extends and the velocity within increases as the IC angulation increases. An example of this region is represented by a dashed circle in Figure 3.12. Vortices of reduced velocity ( $< 5\% V_{\max}$ ) are identified on both sides of IC for all configurations and the extent of these vortices also increases with the increase of IC angulation.

Figure 3.14 and Figure 3.15 present the RIC for C3 and C14 respectively where the RIC maxima are overall higher ( $\text{RIC} \geq 0.5$ ) for C3 than for C14. Wide ranging investigation allowed to distinguish three angulations ranges for both LV shapes (Ben Abid et al., 2019). These ranges are illustrated in Figure 3.16 and divided as follows:

- Apical angulations  $[0^\circ, 40^\circ]$
- Inter-Ventricular Septum (IVS) angulations  $[70^\circ, 90^\circ]$ .
- Intermediate angulations  $[50^\circ, 60^\circ]$ .

For apical angulations range, RIC is high and increases with IC angulation suggesting that LV washout is enhanced with an aligned IC ( $0^\circ$ ). For intermediate angulations range, RIC behaviour regarding IC angulation changes.

### C3

Max = 0.41 m/s   Max = 0.43 m/s   Max = 0.45 m/s   Max = 0.47 m/s   Max = 0.50 m/s

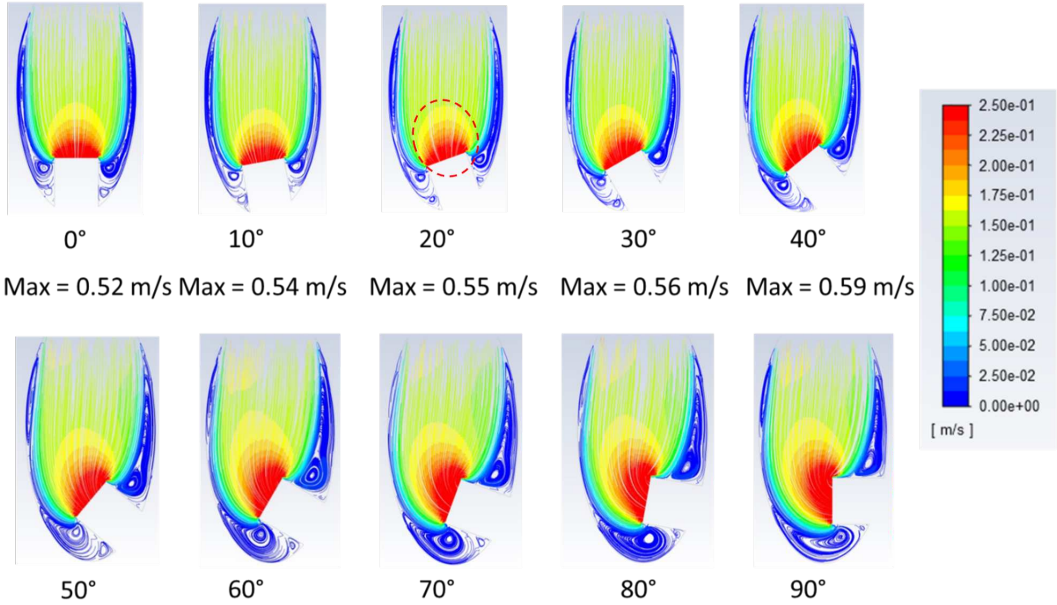


Figure 3.12: IC angulation: Velocity path-lines for case C3. The dashed circle points to region where the blood is drawn into the IC .

### C14

Max = 0.41 m/s   Max = 0.43 m/s   Max = 0.45 m/s   Max = 0.49 m/s   Max = 0.52 m/s

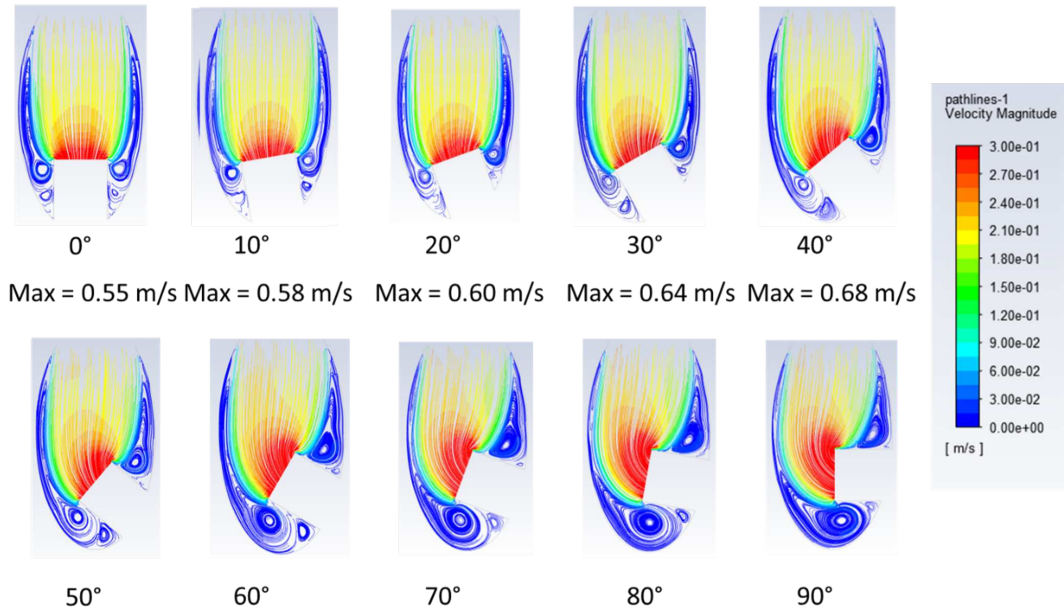
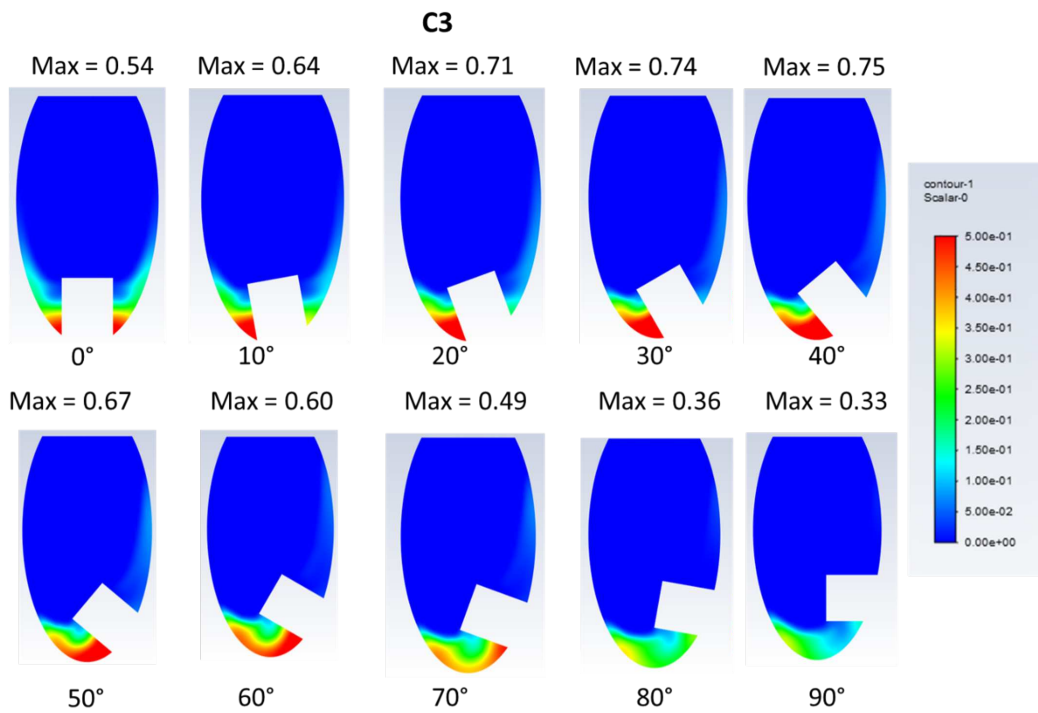
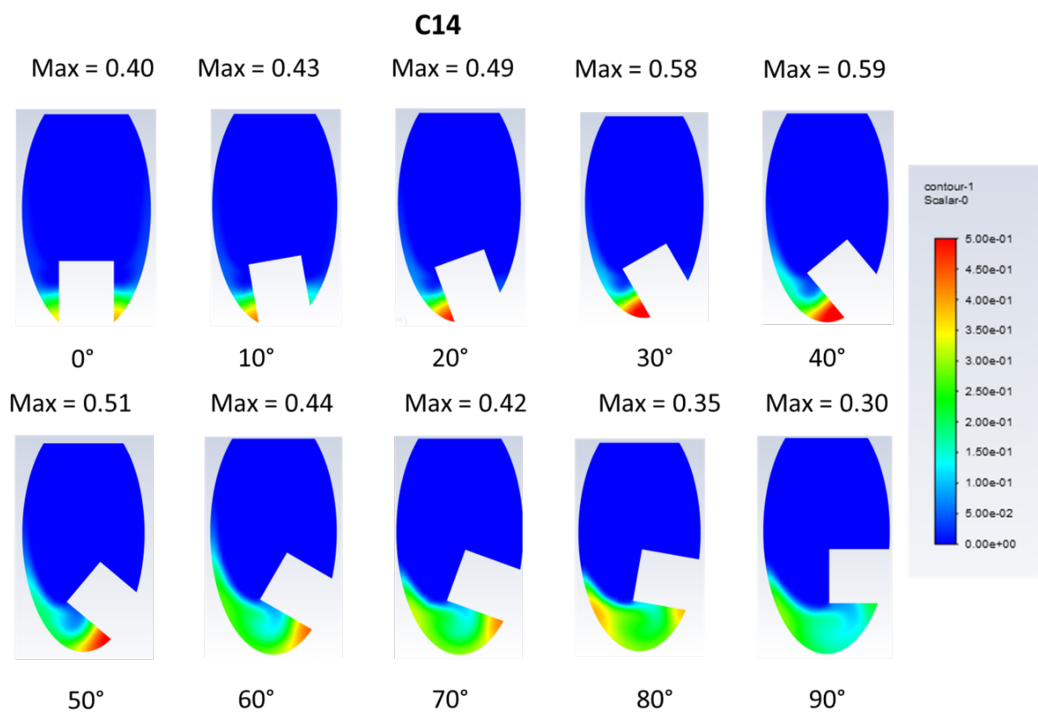


Figure 3.13: IC angulation: Velocity path-lines for case C14.





**Figure 3.14:** IC angulation: RIC for case C3. Areas coloured in red when the RIC is 50% of the initial red ink concentration or more.



**Figure 3.15:** IC angulation: RIC for case C14. Areas coloured in red when the RIC is 50% of the initial red ink concentration or more.

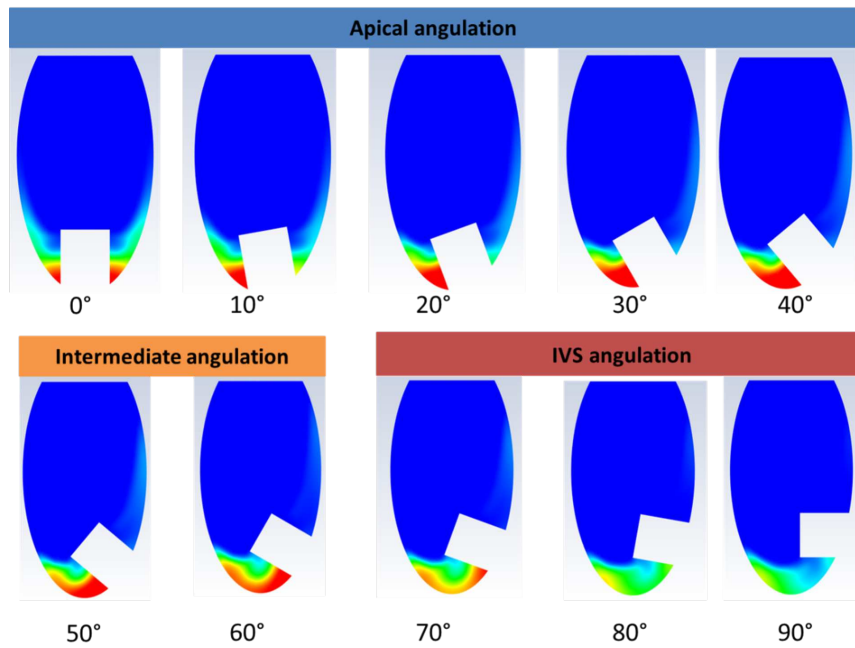


Figure 3.16: Angulation ranges based on the RIC distribution.

RIC is high and decreases as the IC angulation increases suggesting that LV washout is enhanced by the IC angulation. For IVS angulations range, RIC is low and continues to decrease with the increase of IC angulation, continuing to suggest that LV washout is enhanced with IC angulation. These results are due to vortices that are extended over larger areas (observed previously). The dye remaining in these low velocity vortices is distributed over the entire surface of the vortex which reduces its concentration. In fact, when analysing velocity streamlines and RIC figures of each case, one can notice that areas, where the dye remains, coincide with areas of vortices with reduced velocity. When RIC is high, these low velocity regions can be considered as potential stagnation regions.

For apical angulations range, potential stagnation regions are likely to increase with IC angulation, while for IVS angulations range, the potential stagnation regions are likely to decrease with IC angulations. Although these results seems quite surprising, finding a higher ink concentration for  $0^\circ$  than for  $90^\circ$  is aligned with the ink concentration results obtained by (Prisco et al., 2017).

WSS increases as the IC angulation increases (Table 3.6). For all configurations, WSS is under the interval where platelet activation is stimulated  $[3.5; 5] \text{ Pa}$  (Hellmuth et al., 2016). Nevertheless, for  $80^\circ$  and  $90^\circ$  for both cases the maximal value of WSS closely approaches the interval of platelet activation ( $3.31 \text{ Pa}$  and  $3.36 \text{ Pa}$  for C3 and  $3.35 \text{ Pa}$  and  $3.45 \text{ Pa}$  for C14, respectively). We can also notice that WSS increases consequently starting from intermediate angulations range:  $50^\circ$  for C3 and  $60^\circ$  for C14 (Figure 3.17).

Max WSS (Pa)	0°	10°	20°	30°	40°	50°	60°	70°	80°	90°
C3	1.72	1.73	1.74	1.75	1.86	2.21	2.84	3.23	3.31	3.36
C14	1.86	1.88	1.89	1.89	1.92	1.95	2	2.9	3.35	3.45

**Table 3.6:** Impact of IC angulation on WSS maximal value for both cases.

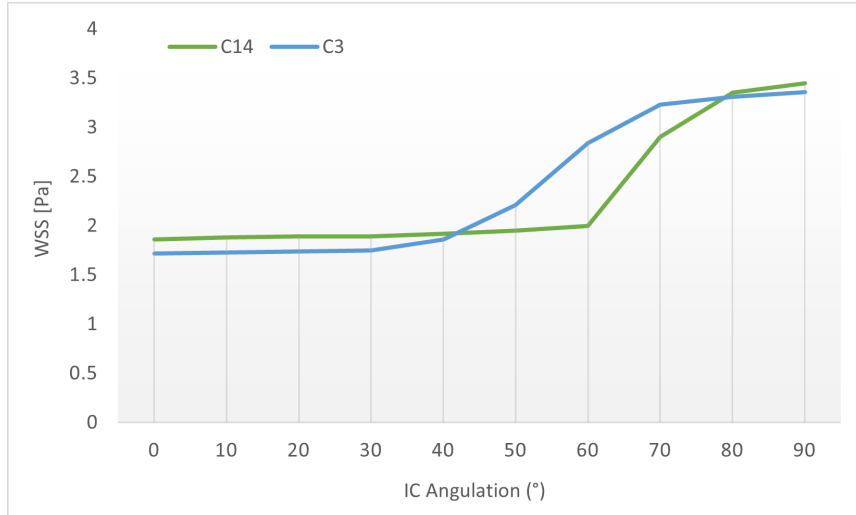


**Figure 3.17:** WSS max as a function of IC angulations, for C3 and C14.

In summary, simulating a wide range of IC angulations allowed to identify vortices formation within the ventricle, not explicitly observed in 3D models. These vortices highlighted that the analysis of low velocity magnitude and RIC within vortices allowed a better understanding of LV haemodynamic. Same tendencies in QOI behaviour (including WSS) between both LV shapes were observed.

### 3.3.3 Influence of inflow cannula length

In this section, the influence of IC length on LV haemodynamic is investigated on two distinct cases (C3 and C14), previously presented in Table 3.6. Three IC lengths are considered:

- IC-L: 34 mm corresponding to the IC length of Berlin INCOR LVAD: Long
- IC-L: 20 mm corresponding to the IC length of HM2 and HM3
- IC-L: 10 mm which is an empirical value for analysis purpose.

Figure 3.18 and Figure 3.19 illustrate the influence of IC length on LV haemodynamic, considering two IC angulations  $[0^\circ, 10^\circ]$  for C3 and C14, respectively. For both cases, the laminar profile located at the central jet is equivalent for the different IC lengths. The maximum velocities are similar with a slight increase when the IC the IC angulation is  $10^\circ$ . One can observe that the increase of IC length, increases the extend of

the low velocity vortices, located at the apex, on either side of IC. The increase of the IC length alters the flow within the ventricle. This observation was also pointed by (May-Newman et al., 2017).

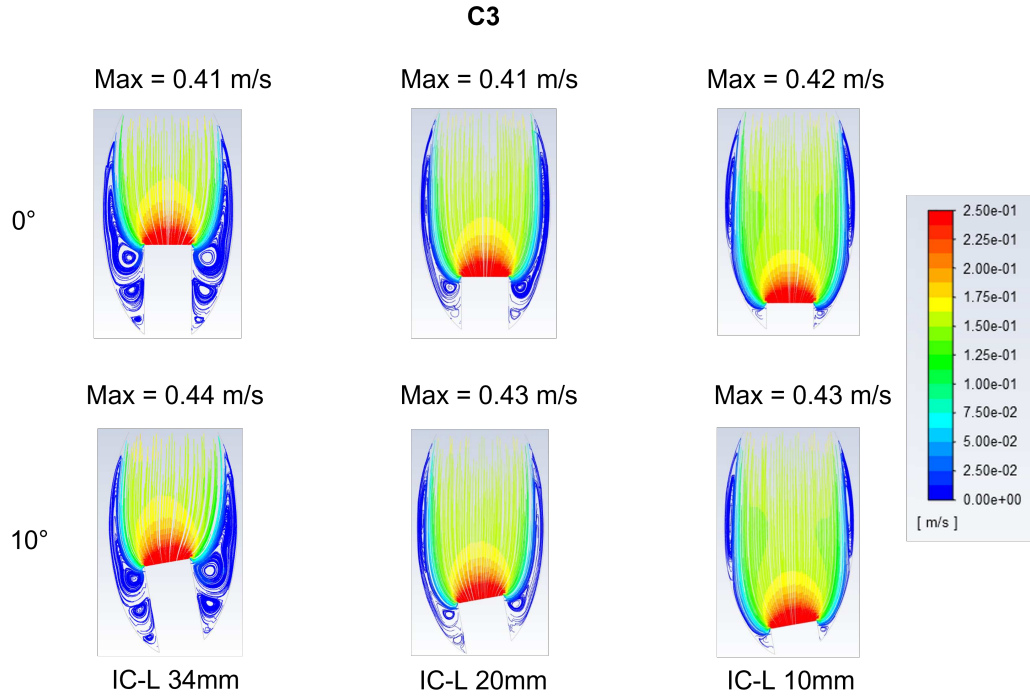


Figure 3.18: IC length: Velocity pathlines for case C3.

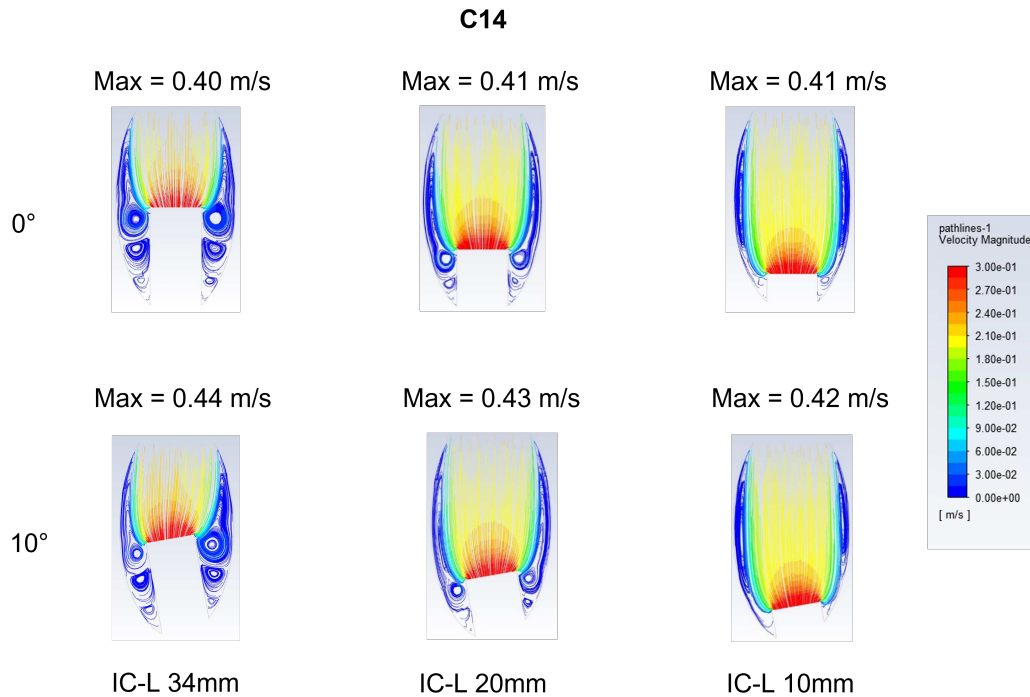
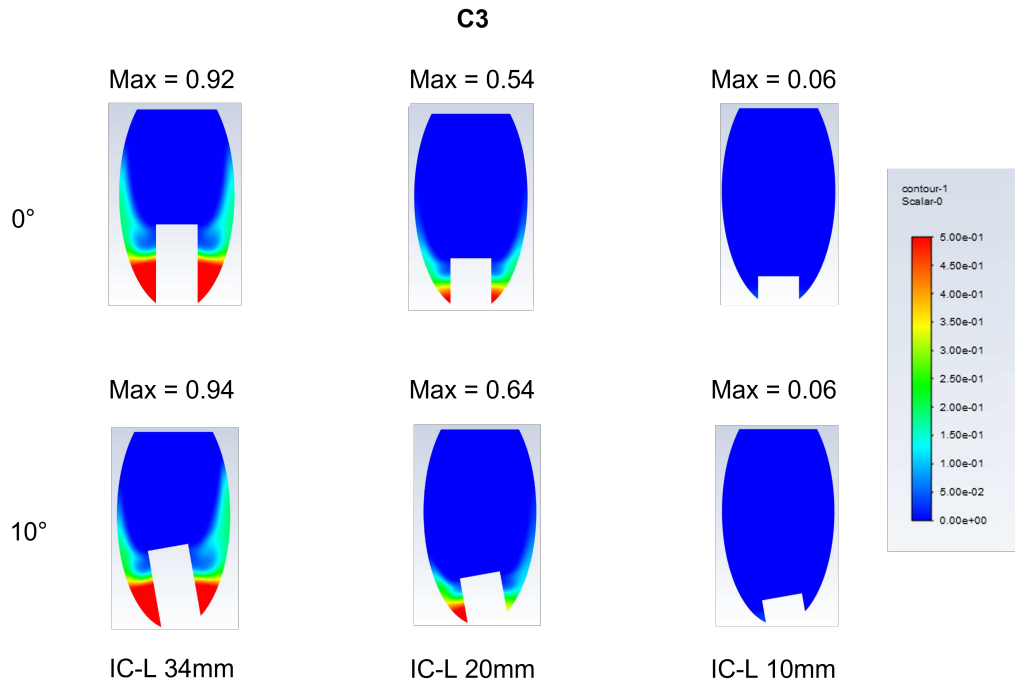
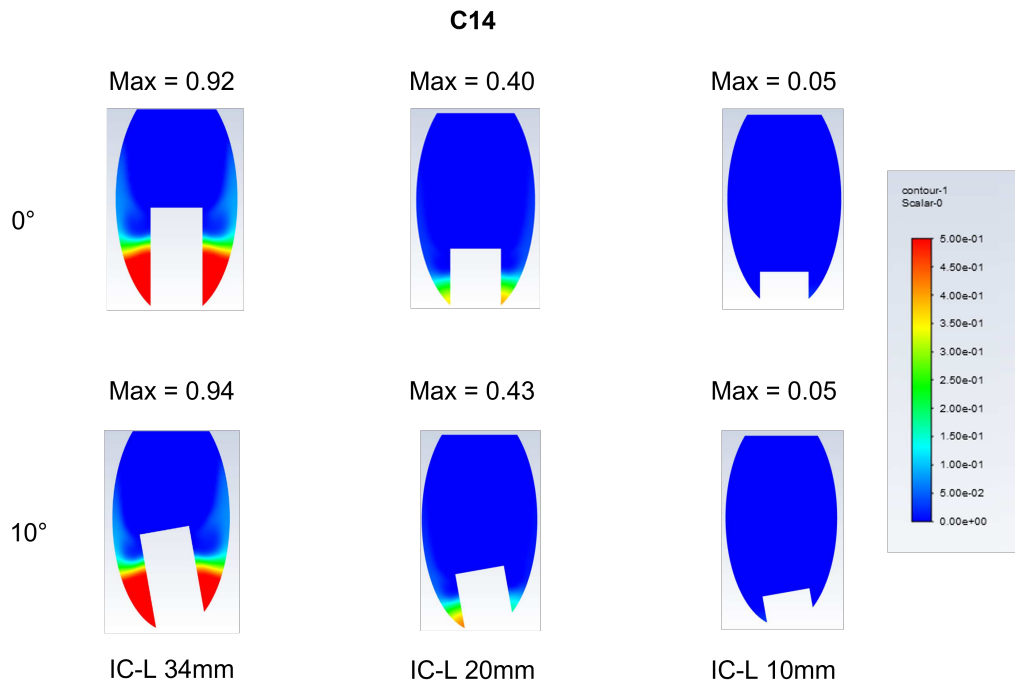


Figure 3.19: IC length: Velocity pathlines for case C14.

Figure 3.20 and Figure 3.21 illustrate the impact of IC length combined with IC angulation on RIC for both C3 and C14, respectively. RIC is slightly higher for configurations with an IC angulation of 10°.



**Figure 3.20:** IC length: RIC for case C3. Areas coloured in red when the RIC is 50% of the initial red ink concentration or more.



**Figure 3.21:** IC length: RIC for case C14. Areas coloured in red when the RIC is 50% of the initial red ink concentration or more.

As the IC length decreases, the RIC decreases significantly. This could be explained by the decrease of low velocity vortices around the inflow cannula region due to IC length decrease. Hence, a long IC may promote blood likely to stagnate within the LV apex. Nevertheless, it should be noted that a reduced IC-L may lead the unclipping of the IC from the ventricle.

Table 3.7 illustrates the influence of IC length on WSS maximal values. WSS is low for all configurations. The variation of WSS in regard to IC angulation is more significant for the longest IC (34 mm). When IC-AD = 0°, WSS decreases as IC length increases. However, when IC-AD = 10°, WSS increases as the IC length increases. For IC lengths of 10 mm and 20 mm, WSS maximal values are close for both angulations.

To summarise, IC length influences LV haemodynamic, this influence is enhanced with IC angulations. The influence on QOI behaviour, especially WSS is greater as the IC length increases. As for IC angulation, Same tendencies in QOI behaviour were identified for both LV shapes.

Max WSS (Pa)	C3		C14	
	0°	10°	0°	10°
IC-L 34mm	1.69	1.77	1.84	1.97
IC-L 20mm	1.72	1.73	1.86	1.88
IC-L 10mm	1.71	1.73	1.87	1.89

**Table 3.7:** Impact of IC angulation on WSS maximal value for both cases.

### 3.4 Conclusion

The aim of this chapter was to propose a simplified model able to give a better understanding of the influence of IC features, especially IC angulation on LV haemodynamic and to identified the relevant QOI.

A 3D approach concluded that investigating several QOI is relevant and a wide ranging investigations would allow a better understanding of LV haemodynamic and QOI behaviour regarding IC angulation. Since the time computation of 3D models is high, the analysis of 2D models was considered and the 2D assumption was verified. Despite limitations, 2D models was able to grasp the same QOI tendencies regarding IC angulation. 2D models revealed to be interesting as their analysis was more simple and QOI analysis seemed relevant. 2D approach was proposed and used to investigate a wide range of IC angulations and length for two different LV shapes.

Results allowed to identify some tendencies in QOI behaviours regarding IC features for both cases. These behaviours identified vortices formation that highlighted the need to combine some QOI (velocity and RIC) with vortices to allow a better understanding of blood stagnation. However, a straightforward analysis of the different QOI is not sufficient to be used and interpreted directly for clinical decision-support. A marker able to evaluate the thrombosis risk associated with a specific configuration (LV shape and IC feature) is required. In the next chapter, a Personalised Thrombogenic Potential Marker is proposed.

# A personalised thrombogenic potential marker

The flow analysis revealed that QOI are able to evaluate blood stagnation and platelet activation. In this chapter, the combination of these QOI (velocity, vortices, RIC, WSS and LV shape) allowed to define a digital marker able to estimate the thrombogenic potential related to a specific LV and IC configuration.

In the first section, blood stagnation and thrombus formation influencing factors are presented. In the second section, available methods for vortices identification and quantification are presented. In the third section, the personalised thrombogenic potential marker or PTPM is defined and a pipeline is proposed. In the fourth section, a study on clinical cases is carried out to define the Personalised Thrombogenic Potential Marker (PTPM) settings. Once fully defined, the PTPM is then used to investigate the impact of different features (IC angulation, IC length, LV diameter) on thrombogenic potential. Finally, a limitation study of the pipeline is held.

## 4.1 Blood stagnation and thrombus formation

As already pointed out, thrombus formation is a complex phenomenon that is not fully understood. It is associated with coagulation and platelet aggregation which are two intertwined processes that are strongly affected by blood dynamics in ways that are yet not fully understood (Carrascal et al., 2017). As a matter of fact, hemostasis (thrombus formation factor according to Virchow's triad) occurs in two phases: the primary hemostasis consists of activated platelet forming a static plug and the secondary phase consists of a stabilization of this plug through coagulation cascade (Saad et al., 2022). Platelet activation can be induced either chemically through the combined effect of Adenosine DiPhosphate (ADP), thrombin, and thromboxane A<sub>2</sub>, or mechanically, through exposure to high level shear stress (Rojano et al., 2021).



Moreover, the multimers of vWF present in the plasma are activated instantaneously under high shear stress ( $\tau \geq 3.5-5$  [Pa]) and bind to platelet GPIIb/IIIa receptor leading to platelet activation, then adhesion and finally aggregation (Peyvandi et al., 2011). The size of the aggregated platelet are regulated through the shear intensity (Hellmuth et al., 2016).

A recent study (Rojano et al., 2021) attempted to simulate thrombus formation. It included platelet activity and simplified coagulation reactions, due to the computational cost. They applied the numerical model proposed by (Wu et al., 2017) for blood vessel on LVAD patient. Authors concluded that thrombin production is more triggered by blood coagulation, hence, blood stagnation rather than mechanical platelet activation (WSS) which is concordant with criteria used in previous CFD studies. Moreover, they observed that the main source of thrombin formation is the tissue damage associated with early stage of VAD implantation. Their results explain thromboembolic events associated with LVAD implantation in the short-term due to the surgical procedure but not long-term complications due to LVAD implantation. In the light of their findings, we consider only mechanical triggers of platelet activation (high WSS) and blood stagnation involved with thrombus formation in this chapter.

Apart from chemical aspect, thrombus formation may be influenced by haemodynamic features such as fluid stresses, residence time in stagnation zones, and blood flow rate (Sukavaneshvar et al., 2000). Based on the obtained results in the literature and simulations in the previous chapter, blood stagnation zones are recirculating areas with low velocity. These re-circulation areas are vortices formed within the ventricle. Vortices have a major role in LV haemodynamic and washout. However, their formation within the LV during diastole significantly contributes to the efficiency of the blood pumping function, while altered vortex formation has been associated with ventricular pathologies (Elbaz et al., 2014; Kheradvar and Pedrizzetti, 2012). Indeed, the global diastolic function of LV can be revealed by the intra-ventricular vortices formed by the morphology and function of the cardiovascular system (Zhou et al., 2017). Previous studies qualified vortices formation to evaluate LV haemodynamic, washout and blood stagnation. As a matter of fact, (McCormick et al., 2013) simulated a healthy heart implanted with BerlinHeart LVAD and observed that the presence of IC resulted in a more complex vortex structure. In this sense, (Ong et al., 2013) simulated a 2D ellipsoid for three different IC lengths and noticed obvious changes in the vortices distributions and intensity when the primary vortex ring comes into contact with the cannula. (May-Newman et al., 2019a) and (May-Newman et al., 2019b) held an in vitro mock loop of a dilated ventricle of a HF patient to investigate the effect of inflow cannula angle and length, respectively, on thrombus formation for two pump speeds. Their analysis of thrombogenic potential was mainly based on observations of vortices formation and circulation. (Töger et al., 2012) studied vor-

tices based on MRI images and Lagrangian coherent structures and concluded that vortex ring accounted for 51% of diastolic ventricular volume for healthy patients vs. 21% for patients suffering from ischemic cardiomyopathy. (Carlhäll and Bolger, 2010) carried out multidimensional flow-based investigations of HF using dynamic 4D images. They observed that in HF, vertical structures are persistent and that vortical extend may indicate a dysfunctional heart. (Evin et al., 2019) reported that focusing on coherent structure detection in cardio-vascular systems reliably detects abnormal or inefficient flow patterns compared to normal ones as well as flow conditions that may lead to secondary pathological processes that are thought to play a critical role in avoiding stasis by washing out the left ventricle.

Vortices formed within the ventricle are a significant indicator of blood stagnation. Quantitative measurements of vortices attributes may provide additional understanding to diastolic function and dysfunction.

To develop a personalised thrombogenic potential marker, we will rely on platelet activation, blood stagnation and LV shape, as influencing features of LV haemodynamic. Platelet activation is evaluated based on high shear stress. Blood stagnation is evaluated based on vortices formation, through velocity magnitude and RIC as a high concentration ink level reflects a low blood clearance (washout) thus a high residence time of blood particles within the ventricle. However, vortices are complex to define, and their identification may be challenging. In the next section, vortices definition and different identification methods are presented.

## 4.2 Vortices definitions and identification

Although the concept of a vortex is known to all from its presence in nature, it is challenging to find a clear and a precise mathematical definition. A vortex can be described as a group of fluid particles with a swirling motion around a common axis. Among all the existing types of vortices, vortex rings (also known as toroidal vortices) are abundant in nature due to their compactness and stability (a tornado or a siphon). However, there is no consensus to mark out the extent of a vortex from its rotation centre. Due to viscosity, it is difficult to define a beginning or an end to the structure. Even though vortices are usually associated with turbulent flow, they also occur in laminar flow. Since observing these turbulent structures, several mathematical methods have been developed based on velocity fields to identify them. A few of them are detailed in the next section.

### 4.2.1 Coherent structures

As for vortices, coherent structures also do not have a strict definition. A coherent structure represents any shape or pattern that can affect the movement of a fluid.

Originally, the notion of the coherent structure was introduced during the discussion on turbulence. For a given velocity field, coherent structure identifies the zones where the fluid's mixing or movement is less important than expected, meaning that a portion of the fluid roughly stays together (coherent) while moving through the fluid. The significant difference between a vortex and a coherent structure is that the former requires vortical motions while the latter does not. Therefore, a vortex is a coherent structure; however, a coherent structure does not necessarily imply a vortex (Jeong and Hussain, 1995; Shadden et al., 2005).

The definition of coherent structures aims to classify the movement of the fluid, of chaotic appearance, into a multitude of elementary movements which will persist spatially and temporally. Several definitions have been proposed in the literature, linking vortices and coherent structures to identify them.

#### 4.2.2 Vorticity

Fluid vorticity may be directly obtained from the rotational of the velocity fields ( $\overrightarrow{\text{rot}}(\mathbf{u})$ ), where  $\overrightarrow{\text{rot}}$  is the rotational or curl vector operator used to describe the infinitesimal circulation of a vector field in an Euclidian space. This approach is suited to visualize vortices but is not sufficient to identify them (Kida and Miura, 1998; Moin and Kim, 1985). Vorticity is unable to differentiate between pure shearing motions and actual swirling motion of vortices (Kida and Miura (1998)). Local methods (point by point) are developed to decompose vorticity into two parts of distinct nature, known as shear and residual which is a direct measure of the vortical swirling motion (Kolář, 2007). This decomposition methods are called vortices identification methods. Different methods are proposed, among them, we will focus on vortices identification methods based on the velocity field gradient tensor.

#### 4.2.3 Vortices identification methods

In 3 dimensions, the gradient  $\nabla \mathbf{u}$  of the velocity field  $\mathbf{u}$  is a second-order Cartesian tensor  $A$  defined according to the orientations  $i, j, k$  of an orthonormal basis:

$$A = \begin{pmatrix} \frac{\delta u_i}{\delta x_i} & \frac{\delta u_i}{\delta x_j} & \frac{\delta u_i}{\delta x_k} \\ \frac{\delta u_j}{\delta x_i} & \frac{\delta u_j}{\delta x_j} & \frac{\delta u_j}{\delta x_k} \\ \frac{\delta u_k}{\delta x_i} & \frac{\delta u_k}{\delta x_j} & \frac{\delta u_k}{\delta x_k} \end{pmatrix} \quad (4.1)$$

where  $u_i$  is a velocity component and  $\delta x_i$  is the distance along the orthogonal axis  $i$ , respectively. This Cartesian tensor can be divided into a symmetric part  $S$  and an anti-symmetric part  $\Omega$  (also referred as skew-symmetric):

$$\mathbf{A} = \mathbf{S} + \boldsymbol{\Omega} \quad (4.2)$$

$\mathbf{S}$  and  $\boldsymbol{\Omega}$  are respectively known as the rate of strain and vorticity tensors. Using their symmetric properties, they can be defined using  $\mathbf{A}$  as such:

$$\mathbf{S} = \frac{1}{2}(\mathbf{A} + \mathbf{A}^T) \quad (4.3)$$

$$\boldsymbol{\Omega} = \frac{1}{2}(\mathbf{A} - \mathbf{A}^T) \quad (4.4)$$

Since  $\mathbf{A}$  is a  $3 \times 3$  matrix, the Cayley Hamilton theorem can be used to express it as a characteristic polynomial of third-degree. The characteristic polynomial for the velocity field gradient is given by (4.5), where  $P$ ,  $Q$  and  $R$  are its three invariants. These invariants are then decomposed into symmetric and anti-symmetric parts (4.6), (4.7) and (4.8).

$$\lambda^3 + P\lambda^2 + Q\lambda + R = 0 \quad (4.5)$$

$$P = -\text{Tr}\{\mathbf{A}\} \quad (4.6)$$

$$\begin{aligned} Q &= \frac{1}{2}(\text{Tr}\{\mathbf{A}\}^2 - \text{Tr}\{\mathbf{A}^2\}) \\ &= \frac{1}{2}(\|\boldsymbol{\Omega}\|_{\mathbb{F}}^2 - \|\mathbf{S}\|_{\mathbb{F}}^2) \end{aligned} \quad (4.7)$$

$$R = -\det(\mathbf{A}) \quad (4.8)$$

when the flow is considered incompressible, the invariant  $P = 0$ . The vortices identification methods are based on these notions and rely on the study of the remaining invariants and tensors. Those methods are presented below.

**$Q$ -criterion:** In this method, a vortex is defined as a "*connected fluid region with a positive second invariant of  $\nabla\mathbf{u}$* " (Kolář, 2007). A positive value of  $Q$  means that the vorticity tensor overcomes the strain tensor, ensuring a vortex structure. An important value of  $Q$  reflects an important difference between the internal vorticity and the deformation rate within a vortex (Zhang et al., 2018). Therefore, a normalized  $Q$ -criterion (4.9) is usually used where  $Q_{max}$  is the maximum value of  $Q$ .

$$Q_n = \sqrt{\frac{Q}{Q_{max}}} \quad (4.9)$$

This identification method is suitable for large-scale vortices in turbulent flow and incompressible fluid.

**$\Delta$ -criterion:** This criterion defines a vortex as “the regions in which the eigenvalues of  $\nabla \mathbf{u}$  are complex, and the streamline pattern is spiralling or closed” (Kolář, 2007). In order to obtain complex conjugated eigenvalues, the discriminant of the characteristic equation must be positive (4.10).

$$\Delta = \left(\frac{Q}{3}\right)^3 + \left(\frac{R}{2}\right)^2 > 0 \quad (4.10)$$

This identification method is only valid when the flow is incompressible ( $P = 0$ ). A high value  $\Delta$  reflects a strong spiralling within the vortex region. However, this criterion is less restrictive than the  $Q$ -criterion. Indeed, since  $\left(\frac{R}{2}\right)^2$  is always positive, then, a positive  $Q$  implies a positive discriminant ( $\Delta > 0$ ), while a negative  $Q$  does not necessarily imply a negative discriminant (i.e., in case  $\left(\frac{R}{2}\right)^2 > \left(\frac{Q}{3}\right)^3$ ).

**$\lambda_2$ -criterion:** In a vortex, the pressure tends to have a local minimum on the axis of a circular motion. However, the proposed criterion (Jeong and Hussain, 1995) neglects two effects that influence vortex detection: the first is the unstable flow strain which can create a minimum of pressure without causing a vortex or swirling movement, the second is the viscous effect which can eliminate this pressure minimum that occurs in flows with a vortex motion. The gradient of the Navier-Stokes equation is expressed as follows:

$$a_{i,j} = -\frac{1}{\varphi} p_{i,j} + v u_{i,jkk} \quad (4.11)$$

where  $a_{i,j}$  is the acceleration gradient and  $p_{i,j}$  is the local pressure extremum. Since  $p_{i,j}$  is symmetric, the acceleration gradient can also be decomposed into symmetric and anti-symmetric components. While the anti-symmetric part is known as the transport equation, the symmetric part is expressed as follows:

$$\frac{DS_{i,j}}{Dt} - v S_{ij,kk} + \Omega_{ik} \Omega_{jk} + S_{ik} S_{kj} = -\frac{1}{\varphi} p_{i,j} \quad (4.12)$$

The first term of this equation (4.12) refers to the unsteady irrotational straining, while the second term refers to the viscous effects. Therefore, only the terms  $S^2 + \Omega^2$  will be taken into account to assess the existence of a local pressure minimum. A

vortex core is defined as "a connected region with two negative eigenvalues of  $\mathbf{S}^2 + \boldsymbol{\Omega}^2$ ". Knowing that  $\mathbf{S}^2 + \boldsymbol{\Omega}^2$  being symmetric allows real eigenvalues only. If  $\lambda_1 \leq \lambda_2 \leq \lambda_3$ , the criterion requires that  $\lambda_2 < 0$ . However, the vortex core lines identified by this criterion may not be continuous since the lines define a set of segments of the vortex core.

**The Swirling Strength criterion:** The swirling strength criterion relies on the imaginary eigenvalues of the velocity gradient to identify a vortex region. It considers that the velocity gradient tensor can be expressed in Cartesian coordinates as follows:

$$\nabla \mathbf{u} = \begin{pmatrix} \bar{v}_r & \bar{v}_{cr} & \bar{v}_{ci} \end{pmatrix} \begin{pmatrix} \lambda_r & 0 & 0 \\ 0 & \lambda_{cr} & \lambda_{ci} \\ 0 & -\lambda_{ci} & \lambda_{cr} \end{pmatrix} \begin{pmatrix} \bar{v}_r \\ \bar{v}_{cr} \\ \bar{v}_{ci} \end{pmatrix} \quad (4.13)$$

where  $\lambda_r$  is the real eigenvalue associated with the eigenvector  $\bar{v}_r$  and the complex conjugate pair of complex eigenvalues ( $\lambda_{cr} \pm i\lambda_{ci}$ ) is associated with the corresponding eigenvectors ( $\bar{v}_{cr} \pm i\bar{v}_{ci}$ ). When the local streamlines are expressed in a coordinate system generated by the eigenvectors, the first eigenvector  $\bar{v}_r$  indicates whether the local flow is compressed or stretched along the axis ( $\bar{v}_r$ ) while the plan defined by  $\bar{v}_{cr}$  and  $\bar{v}_{ci}$  indicates whether the flow is locally swirling (Zhou et al., 1999).

The distinctive characteristic of this criterion is its ability to identify and quantify the vortex. Indeed, the local swirling strength rate inside a vortex is given by  $\lambda_{ci}$  and the strength of the compression or stretching of the vortex is measured by  $\lambda_r$ . The threshold for  $\lambda_{ci}$  is not clearly defined. Theoretically, it is supposed to be fixed at zero; however, the obtained results were smoother when the threshold ( $\epsilon$ ) was fixed at a positive value (Zhou et al., 1999) (4.14). The time-period for completing one revolution of the streamline is given by (4.15).

$$\lambda_{ci} \geq \epsilon > 0 \quad (4.14)$$

$$\frac{2\pi}{\lambda_{ci}} \quad (4.15)$$

**The Enhanced Swirling Strength criterion:** The swirling strength criterion is based on a local analysis of  $\nabla \mathbf{u}$ . However, a vortex is defined as a coherent structure. This definition implies the concept of small and bounded flow regions where the vorticity varies spatially, and the fluid motion remains temporally and spatially coherent. These concepts suggest a non-local aspect of vortical structures. Hence, the

Enhanced Swirling Strength criterion is based on the idea to subset a local swirling region for which a non-local criterion is verified. This non-local criterion is inspired by (Cucitore et al., 1999) analysis. The introduced definition is the inverse spiralling compactness  $\frac{\lambda_{cr}}{\lambda_{ci}}$ . This ratio, also called the local orbital compactness in a vortex, measures the spatial extent of the local spiraling motion. For an incompressible flow, the orbital compactness could be ensured on the vortex plane and along the vortex axis only if these requirements are respected:

$$\begin{aligned} \text{(i)} \quad & \lambda_{ci} \geq \epsilon > 0 \\ \text{(ii)} \quad & -\kappa \geq \frac{\lambda_{cr}}{\lambda_{ci}} \geq \delta \end{aligned} \tag{4.16}$$

where  $\epsilon$  is the swirling strength threshold that ensures smooth results,  $\kappa$  is a positive value that ensures the orbital compactness in the vortex plane, and  $\delta$  is a positive value that ensures the orbital compactness along the vortex axis (Chakraborty et al., 2005). Moreover, orbital compactness also describes the circulation of the vortex spiralling path in the plane as follows:

$$\begin{aligned} \text{(i)} \quad & \frac{\lambda_{cr}}{\lambda_{ci}} < 0 \quad : \text{inward} \\ \text{(ii)} \quad & \frac{\lambda_{cr}}{\lambda_{ci}} = 0 \quad : \text{perfect circular} \\ \text{(iii)} \quad & \frac{\lambda_{cr}}{\lambda_{ci}} > 0 \quad : \text{outward} \end{aligned} \tag{4.17}$$

To conclude, different methods are available to identify vortices. Within these methods only two are able to identify and quantify vortices. These methods are the swirling strength criterion and the enhanced swirling strength criterion. The latter, as its name suggests, is complementary to the former and propose a more global definition of vortices. Moreover, the enhanced swirling strength criterion considers vortices strength and extension within the vortical plane, and the third dimension assesses whether the vortex is stretched or compressed. Hence, this method is suitable for 2D and 3D applications.

### 4.3 Personalised Thrombogenic Potential Marker: A Novel Digital Marker

In this section, a Personalised Thrombogenic Potential Marker is proposed. It is a digital marker able to estimate the TP related to a defined configuration. This estimation aims to determine the optimal configuration, especially IC angulation related to a specific LV shape that suggests the least thrombosis risk for LVAD implanted patient. This section consists in defining the marker where each of its components are

detailed, proposing a pipeline of simulation.

### 4.3.1 Personalised Thrombogenic Potential Marker: definition

As mentioned before, thrombus formation is a multi-factorial phenomenon involving a complex cascade of reactions triggered chemically and mechanically. Its main factor is the platelet activation and aggregation that might be triggered then enhanced by fluid properties. These properties are likely to be high shear stress, RT, blood stagnation and LV dynamics expressed through vortices. Another crucial factor is LV anatomy since it greatly influences LV haemodynamics.

We propose a new marker that not only considers but also combines these 3 identified factors of thrombogenic potential: **the platelet activation** which is the main factor of thrombus formation. **The blood stagnation** which considers factors enhancing platelet deposition and accumulation, these factors consist of blood stasis and RT of blood particles. Finally, **the anatomical factor** which is proper to each patient, reflects the condition of the failing ventricle and impacts LV haemodynamic.

The proposed PTPM is defined as follows:

$$PTPM = P_{WSS} \cdot s_B \cdot F_{AC} \quad (4.18)$$

where  $P_{WSS}$  is the platelet activation potential,  $s_B$  is the blood stagnation score, and  $F_{AC}$  is the anatomical correction factor. The marker is dimensionless, positive and does not exceed 1.

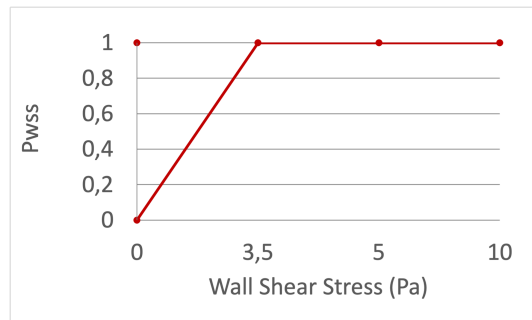


Figure 4.1: Transfer function of the Platelet Activation Potential ( $P_{WSS}$ ).

### 4.3.2 Platelet Activation Potential

Several studies have evaluated the thrombogenic risk via shear stress (Chivukula et al., 2020, 2018; Entezari et al., 2021; Fraser et al., 2010; Hellmuth et al., 2016; Ong et al., 2013; Ruggeri et al., 2006). Indeed, a high shear stress ( $[3.5, 5]$  Pa) applied to the blood particles can lead to platelet activation then aggregation via vWF (Hellmuth et al., 2016). The platelet activation potential ( $P_{WSS}$ ) is estimated by evaluating the



mean value of the WSS within the ventricle to the activation interval [3.5, 5] Pa using a transfer function defined in Figure 4.1.

For extreme cases where  $P_{WSS}$  is null, PTPM could not be also null as the TP within a ventricle could not be non-existent. Indeed, suppose that for an extreme case, the platelet activation potential is null and blood stagnation areas are presents within the ventricle, a chemical platelet activation may still occur due to coagulation factors and stasis areas may promote their aggregation enhancing even slightly the thrombosis risk. Therefore, a condition ought to be added to the  $P_{WSS}$  computation without influencing the final score, this condition is formulated as follows:

---

**Algorithm 1** Pseudo-code for  $P_{WSS}$  computation

---

```

1: if  $P_{WSS} = 0$  then
2:    $P_{WSS} = 1$ 
3: end if

```

---

### 4.3.3 Blood Stagnation score

Blood Stagnation score ( $s_B$ ) evaluates blood stasis and residence time within the ventricle through its clearing ability. Furthermore, vortices are a significant indicator to the efficiency of the blood pumping function. Depending on vortices properties such as swirling motion and extend, they are recirculating areas where the blood is likely to remain the longest in the ventricle. Blood stagnation score is evaluated within vortices. Thus, vortices identification is required.

Vortices identification was performed based on the enhanced swirling strength criterion. It is the only criterion based on velocity gradient tensor that is able to identify and quantify vortices through their orbital compactness and their swirling motion, respectively. Depending on vortices swirling strength, velocity magnitude and clearing ability, vortices might be considered as stagnation areas (Ben Abid et al., 2021). The clearing ability is expressed via the RIC, which reflects the time residence of blood in the ventricle.

The blood stagnation score is defined as follows:

$$s_B = \frac{1}{N} \sum_{n=1}^N \mathbf{a}^T p_n \quad (4.19)$$

where  $N$  is the number of vortices present within the ventricle,  $\mathbf{a}$  is the weight vector, and  $p_n$  is the blood stagnation risk vector associated with the  $n^{th}$  vortex.

### Blood Stagnation risk vector $p$ : Definition

Blood stagnation risk vector quantifies stagnation within each vortex formed in the ventricle. Vortices are identified based on the enhanced swirling strength criterion. Each identified vortex is delimited according to its orbital compactness map, governed by the orbital compactness equation (4.16-(ii)). Once the boundary of each vortex is obtained, potential vortical regions are defined. These regions are evaluated based on the swirling strength map governed by the swirling strength equation (4.16-(i)). Potential vortical regions with a sufficient orbital compactness ( $p_C$ ) and swirling strength are vortical regions. Once these regions are identified, each one of them is quantified based on the weighted average values of swirling strength, velocity magnitude, and RIC to evaluate blood stagnation regions within the ventricle. The main steps to evaluate the blood stagnation regions are summarised in Figure 4.2.

Swirling Strength ( $p_{SW}$ ), Velocity Magnitude ( $p_V$ ) and RIC ( $p_{RIC}$ ) are the attributes of the blood stagnation risk vector ( $p$ ). According to the literature, none of these attributes seems to have a more significant impact on blood stagnation, thus, these attributes are equally weighted ( $a = \frac{1}{3}$ ). To summarise, vortical region are identified according to the enhanced swirling strength criterion governed by equation (4.16). This equation is transcribed through  $p_C$  and  $p_{SW}$  attributes. Finally, the number of vortices identified ( $N$ ) and their associated blood risk vectors ( $p_n$ ) are evaluated according to the following algorithm:

---

**Algorithm 2** Pseudo-code for blood stagnation regions evaluations

---

```
 $n = 0$ 
2: for  $i \leftarrow 1, X$  do
    if  $p_{C_i} \neq 0$  and  $p_{SW_i} \neq 0$  then
4:      $n = n + 1$ 
         $p_n = \begin{bmatrix} p_{SW_i} & p_{RIC_i} & p_{V_i} \end{bmatrix}^T$ 
6:     end if
     $N = n$ 
8: end for
```

---

where  $p_{C_i}$ ,  $p_{SW_i}$ ,  $p_{RIC_i}$  and  $p_{V_i}$  are the attributes of the stagnation risk vector  $p$  at the potential vortical region  $i$ ,  $X$  is the number of potential vortical regions identified,  $N$  is the number of identified vortices,  $n$  and  $i$  are increment variables.

### Blood Stagnation risk vector $p_n$ : attributes

The blood stagnation risk vector attributes defined as follows:

**Orbital Compactness attribute ( $p_C$ ):** As mentioned before, the orbital compactness map is used to define stagnation regions. Therefore, a segmentation is required. The orbital compactness map values and their respective coordinates are extracted.

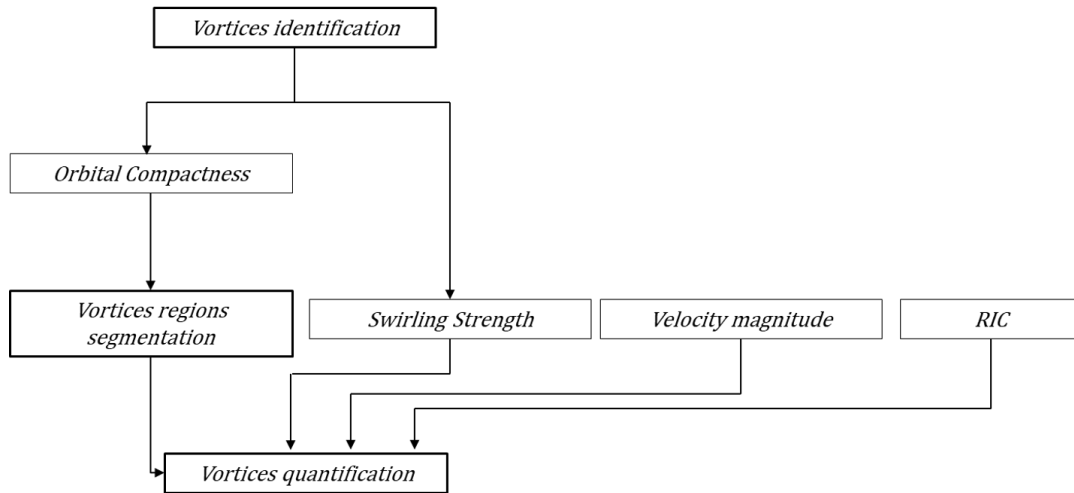


**Figure 4.2:** Summary of the main steps to evaluate blood stagnation regions.

According to the enhanced swirling strength criterion, vortices with high values of orbital compactness could not be considered as vortices. In order to exclude non-compact vortices from compact vortices as required by the criterion (4.20), two thresholds  $\kappa$  and  $\delta$  are empirically applied to the data. Their values are defined through observations to 10 and -10 respectively and are deemed sufficient for a first criteria proposal. After thresholding, the orbital compactness matrix is converted to a greyscale image then binarized using the Otsu's method (Otsu, 1979) as an automated threshold selection method. In short, the threshold value is selected to maximize the separability of the resultant classes in grey level. After that, region boundaries of the binary image are detected according to Moore-Neighbour tracing algorithm modified by Jacob's stopping criteria (Gonzalez et al., 2003). Boundaries coordinates are used to create a polygon in order to define regions (boundaries points are then excluded from the obtained regions). These regions are defined as potential vortical regions

$$-10 \leq \frac{\lambda_{cr}}{\lambda_{ci}} \leq 10 \quad (4.20)$$

Once the potential vortical regions are obtained, the orbital compactness of each vortex is transcribed to a compactness attributed ( $p_C$ ) via a transfer function defined in Figure 4.4-(a).

**Swirling Strength attribute ( $p_{SW}$ ):** Once the potential vortical regions are identified, the swirling strength of these regions is evaluated. The vortex swirling strength ( $\lambda_{ci}$ ) is used for both vortices identification and quantification. As seen in equation (4.14), smoother results are obtained when a non-zero threshold is applied to  $\lambda_{ci}$  (Zhou et al., 1999). However, the choice of the threshold could be quite challenging and different threshold values were proposed. A quite recent research investigated

the choice of the swirling strength threshold for 2D applications and concluded that a value of  $1.5 \text{ s}^{-1}$  is deemed appropriate regardless of the application (Chen et al., 2018). Since we are also proposing a 2D model, the value of  $1.5 \text{ s}^{-1}$  is selected for the swirling strength threshold (4.21).

$$\lambda_{ci} \geq 1.5 \quad (4.21)$$

The potential vortical regions that satisfy the second condition of the enhanced swirling strength criterion (4.21) are vortical regions. These regions are transposed on the swirling strength, RIC and velocity magnitude images in order to quantify the stagnation risk within each vortical region (Figure 4.3).

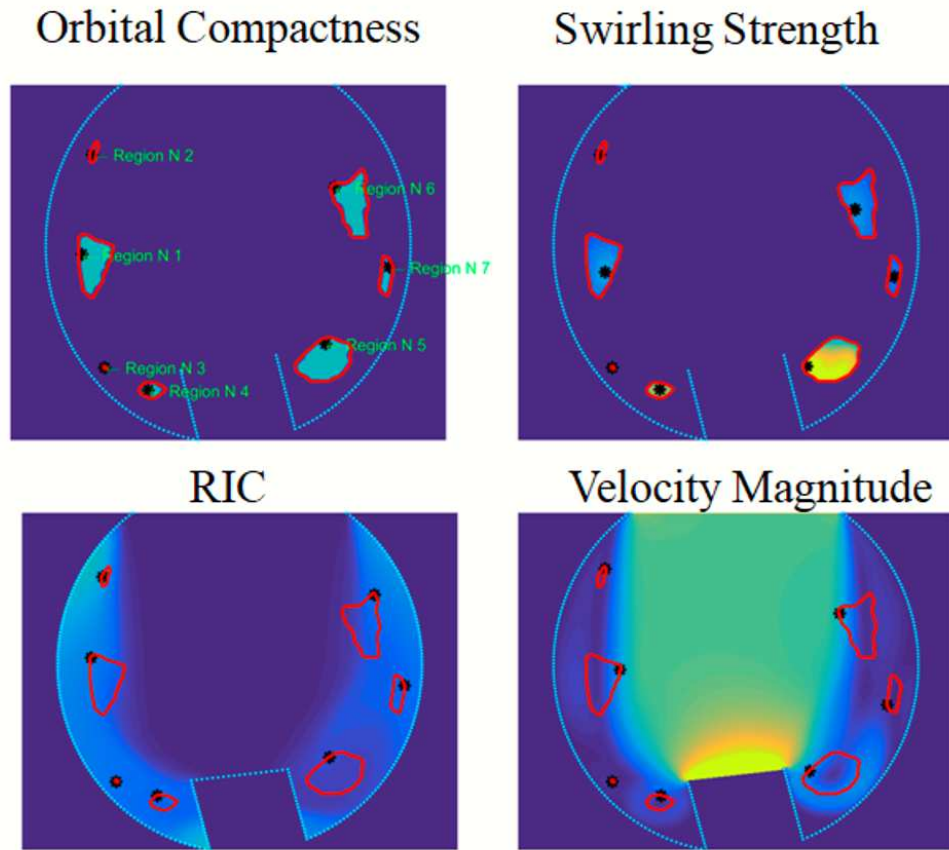


**Figure 4.3:** Image segmentation process based on vortices identification.  
\* define the maximum values positions of each region.

Since the swirling strength is also used for vortices quantification, the mean value of the swirling strength is attributed to ( $p_{SW}$ ) via a transfer function defined in Figure 4.4-(b) where  $p_{SW}$  is considered maximal starting from  $10 \text{ s}^{-1}$ .

**RIC attribute ( $p_{RIC}$ ):** The Enhanced Swirling Strength criterion is able to indicate the time period for one revolution within the vortex plane (4.15). However, the num-

ber of periods required for a fluid particle to leave the vortex is not available. For that reason, the RIC is an indicator of the vortex's ability to clear blood particles. Within each identified vortex, the mean value of the RIC is attributed to  $p_{RIC}$  via a transfer function defined in Figure 4.4-(c).

**Velocity Magnitude ( $p_V$ ):** A low-velocity magnitude implies a high risk of blood stasis. The velocity is considered low if it is under 10% of the maximum velocity. As for ( $p_{RIC}$ ), the mean value of the velocity magnitude (within each identified vortex) is attributed to  $p_V$  via a transfer function defined in Figure 4.4-(d).

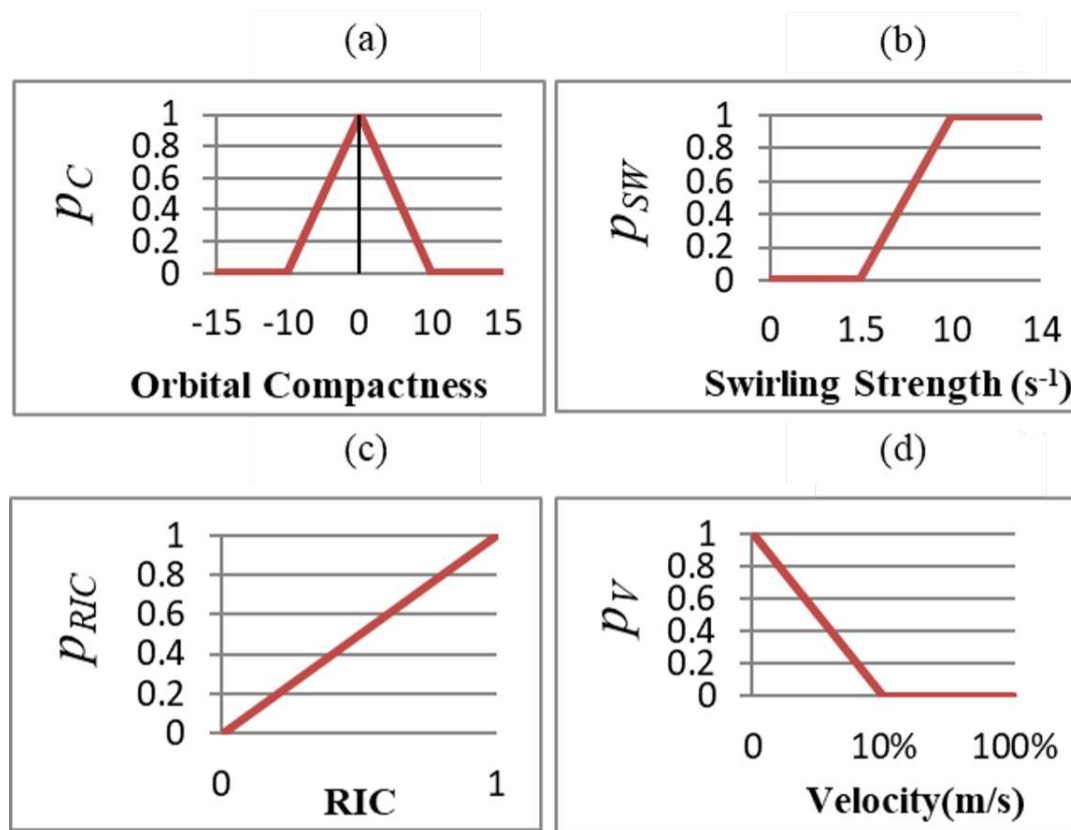


Figure 4.4: Transfer functions associated with the blood stagnation attributes.

#### 4.3.4 Anatomical Correction Factor

The anatomical factor of the ventricle is crucial to consider since it influences LV haemodynamics. The anatomical factor is usually taken into account by the ventricle geometry simulated in its diastolic phase (often in a static state). Nevertheless, no further information concerning the LV systolic state are considered. Yet, depending on its contractility during systolic phase, the LV may help ejecting blood stagnation areas (often at the apex) from LV which may reduce platelet activation (by reducing RT), deposition (in stasis areas) and aggregation reducing thus TP.

Therefore LV geometries in diastolic and systolic phases are compared to estimate LV

contractility. This concept is known as Left Ventricular Sphericity Index (LVSI). It is often used by clinicians as a marker of left ventricular remodelling. LVSI definition differs in the literature. Thus, the definition used in this marker was derived from a recent research (Khanna et al., 2020).

Before that, a Sphericity Index (SI) evaluating the LV geometry during a specific phase (diastolic or systolic phase) is needed. The required measures are obtained from standard echocardiographic images. The SI computation is defined as follows:

$$SI = \frac{1}{N} \sum_{n=1}^N \frac{LVD(n)}{LVL(n)} \quad (4.22)$$

where LVD is the greater cross-sectional diameter of the left ventricle, LVL is the longitudinal length of the left ventricle (Figure 4.5), and  $N$  is the number of measurements. Clinicians perform several measurements of LVD and LVL in both the apical 4/2-chamber views during a specific phase (diastole or systole).

To capture the ventricular remodelling, the SI is computed during diastolic and systolic phases for two cardiac cycles each ( $SI_{ED}$  and  $SI_{ES}$ , respectively). Afterward, the LVSI, used as a geometrical correction factor, is calculated to grasp the mean geometrical change of the ventricle during both phases. This correction factor (LVSI) is called the Anatomical Correction Factor ( $F_{AC}$ ) and is defined as follows:

$$F_{AC} = \frac{SI_{ED} + SI_{ES}}{2} \quad (4.23)$$

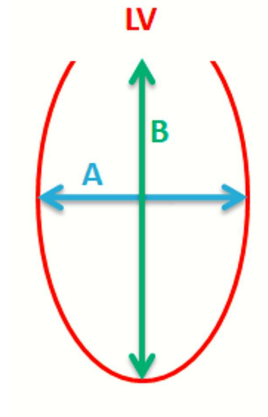


**Figure 4.5:** Representation of the sphericity index computation of the left ventricle. LV is the left ventricle at a specific phase (diastole/systole); A is LVD and B is LVL.

### 4.3.5 Proposed Pipeline

The PTPM is obtained by going through different steps. The proposed pipeline is depicted below.

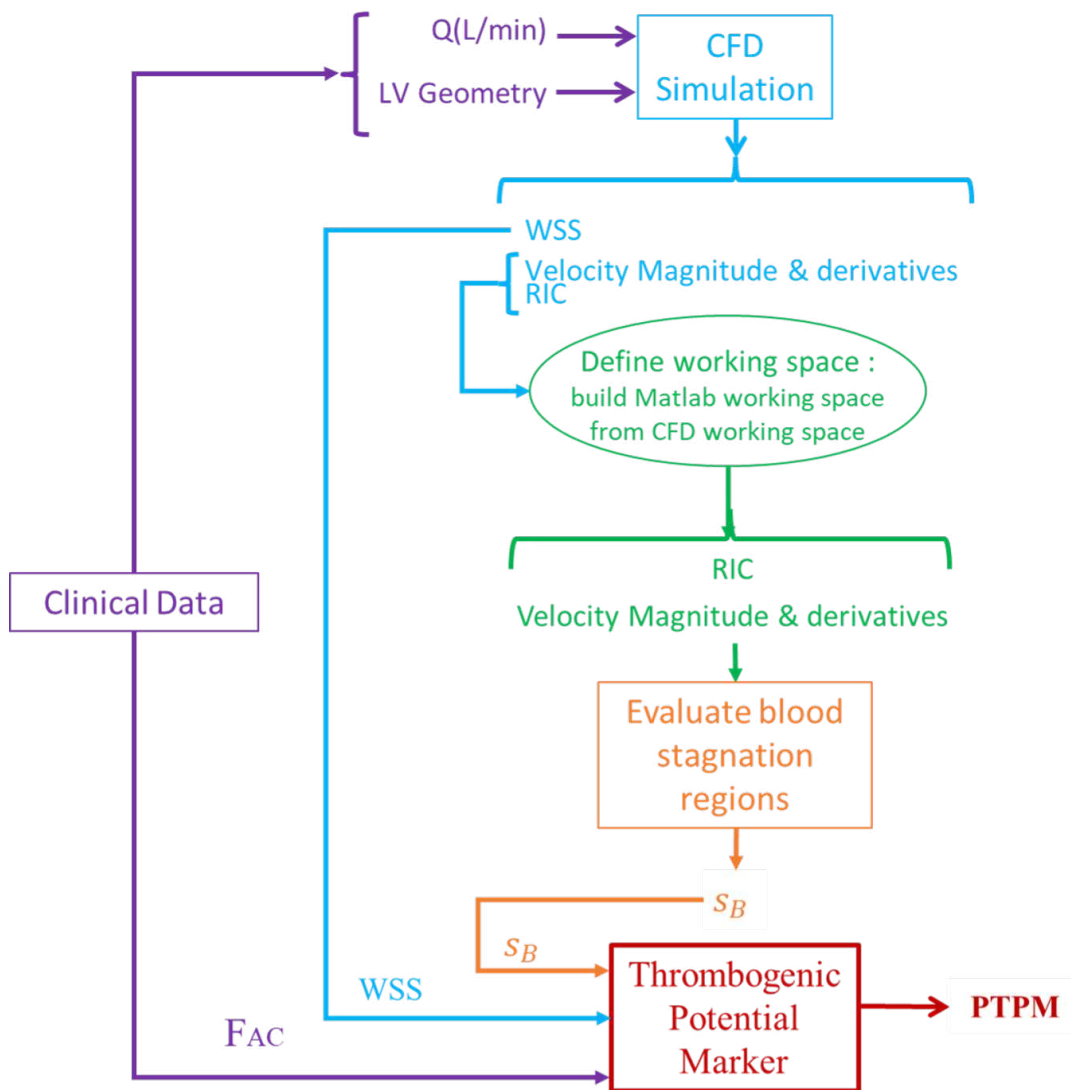


Figure 4.6: Personalised Thrombogenic Potential Marker pipeline.

During **Clinical data**, clinical measurements specific to each patient are collected. These measurements consist of:

- Ventricular measures: Mitral Valve (MV-D) as well as ventricular short (LV-D) and long (LV-H) axis during diastolic and systolic phases.
- Inflow cannula related data: type of LVAD device (IC geometry), measures of IC implanted angulation (IC-AD) and flow rate (Q).

**CFD simulation** uses IC geometry and ventricular diastolic measurements obtained from clinical data to create the corresponding LVAD implanted ventricle and the IC flow rate to define the LVAD pump flow. Details of the CFD model description have been presented in section (3.3.1) of the previous chapter.

**Defining a working space** is an intermediate step aiming to reshape FLUENT work-

space into a regular grid-shaped workspace on MATLAB. This operation is done by interpolating CFD data using natural neighbour methods (Amidror (2002)). It is a local approach based on the Voronoï tessellation of a scattered point set. According to the tessellation, the plane is partitioned into areas defined through an exhaustive and separated set of polygons that encloses each one of the point set. Two points of the set are considered natural neighbours when their respective areas have a common edge or contact point. This is a robust interpolation method that is weighted depending on the area of influence of the surrounding scatter point resulting in a first regular grid definition. Nevertheless, some artefact can be detected outside the model due to the limitation of the interpolation as the scattered point set used for Voronoï tessellation are defined only within the geometry (not outside). To be consistent with the simulation, a mask image is created from the modelled geometry file and applied to isolate the geometry-related data.

Some of CFD output data are converted to the new workspace and used to **evaluate blood stagnation regions**. **PTPM** is obtained by combining the  $F_{AC}$ , the  $P_{WSS}$  and  $s_B$  obtained from the previous steps.

## 4.4 Personalised Thrombogenic Potential Marker: settings

The proposed PTPM depends on different parameters. While most of them are intrinsic and proper to the investigated case such as LV geometry and IC flow rate ( $Q$ ) as well as CFD simulation results (velocity magnitude, its derivatives and WSS), RIC settings (filling and clearing phases) are extrinsic and might be an influencing parameter of the marker. The influence of RIC settings on the PTPM performance is investigated and a thrombogenic threshold of the PTPM is then defined. The final PTPM is used for configurations of two different clinical data sets (patients implanted with HM2 and HM3) and obtained results are compared with clinical outcome.

### 4.4.1 Clinical database

In the university hospital of Rennes, 88 patients were implanted with either LVAD or a total artificial heart between 2007 and 2021. Patients implanted with HM2 and HM3 were selected since they are the most implanted devices, 38 patients and 22 patients for HM2 and HM3, respectively. Due to the bad echogenicity of most HF patients (Figure 4.7) and the lack of data for others (after LVAD implantation, the follow up of some patients was performed in other hospitals), the number of patients selected for the study was 14 for HM2 and 5 for HM3.

Given the user-dependent nature of measurements made on ultrasound images, data measures were performed by two clinical experts. Ventricle features were clinically obtained from ultrasound images (Figure 4.8). For the geometry creation, LV-D was



measured from a long axis parasternal view while MV-D and LV-H were measured from apical four-chamber view (LV-H being the distance for MV plan to LV apex) during the diastole phase. For  $F_{AC}$  attribute computation, LV-D and LV-H were measured from apical 4/2-chamber views during diastolic and systolic phases during two consecutive cardiac cycles (Figure 4.7). IC measurements were obtained from Abbott laboratories and IC implanted angulation (IC-AD) related to each patient was measured from CT-Scans (Figure 4.10). To the extent of possible, all clinical data related to each patient (LV measures, IC angulation and flow rate (Q) were measured around the same time-period for two reasons. First, the flow rate varies throughout the implantation which may impact LV shape and second, to prevent an eventual evolution of the pathology that may exacerbate the ventricular remodelling.

Table 4.1 and Table 4.2 present the patients' conditions and outcomes as well as the clinical information related to the LV and IC features with HM2 and HM3 respectively. In both tables, IC implanted angle column represent the IC-AD measured for each patient. These measures are user-dependent (Figure 4.10), hence, IC-AD angles were rounded to the nearest  $5^\circ$  for CFD simulations. For confidentiality purpose, Patients ID matches those within the clinical data base. According to clinician, a ventricle is considered dilated when its diameter is superior to 55 mm (LV-D > 55).

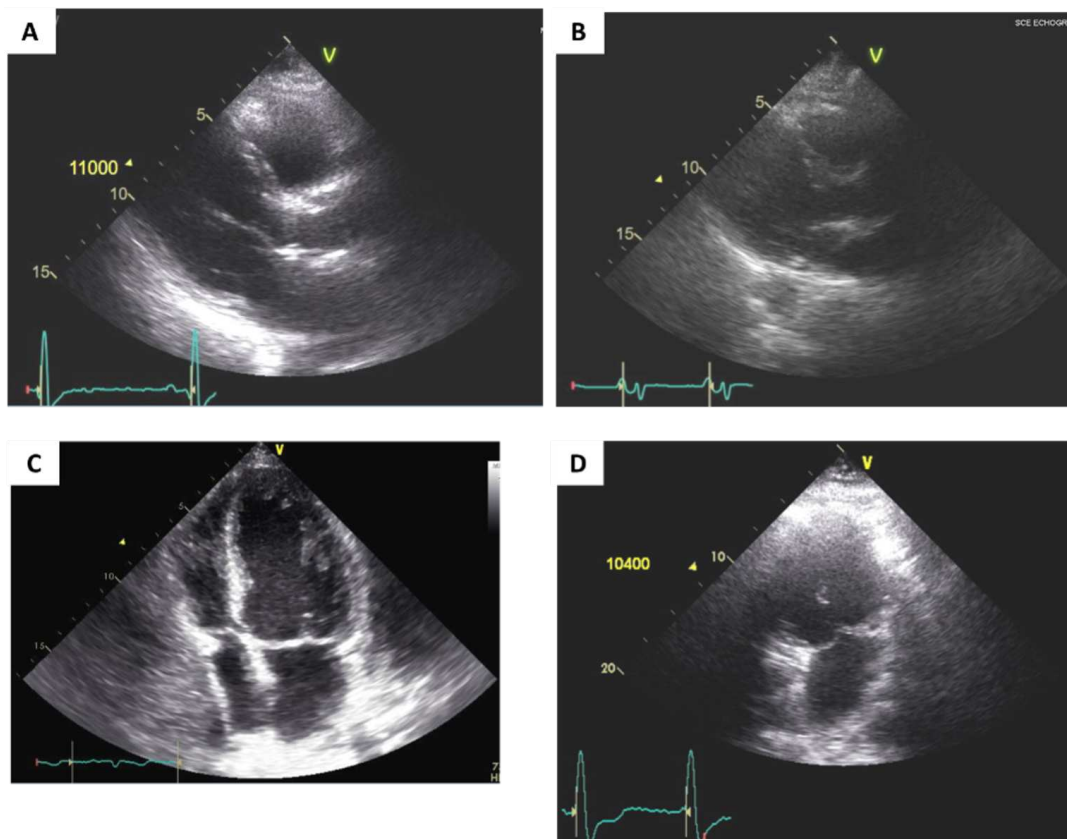


**Figure 4.7:** Ultrasound images in long axis parasternal (above: A/B) and 4-chamber (below: C/D) views during diastolic phase for patients with bad (right: B/D) vs. good (left: A/C) echogenicity.

Patient ID	Ventricular Features					LVAD Features		Complication occurred after LVAD implantation
	LV Condition	VD (mm)	VL (mm)	MV (mm)	F <sub>LVSI</sub>	IC Implanted Angle (°)	Q (L/min)	
P1	Dilated (severe)	67	95.6	40	0.930	60	6.2	Pump thrombosis 4 years
P3	Not Dilated	50	87	34	0.531	45	5	None 9 years
P4	Not Dilated	46	75	36	0.694	30	4.8	Pump thrombosis 2 years
P5	Not Dilated	52	86	41	0.711	30	5.9	Stroke (post LVAD) 4 years
P8	Not Dilated	47	86.7	33.2	0.580	21.4	4.2	None 2 years
P9	Dilated	67	70	35	0.697	54	5	None 4.5 years
P10	Not Dilated	45	95	38	0.719	65	5.5	Pump Thrombosis 4 years
P11	Dilated	50	51.9	31	0.703	18	4.4	None 2 years
P12	Not Dilated	41.8	70.2	23.7	0.584	0	4.9	None 2 years
P13	Dilated	47.7	76.4	24.2	0.639	27.6	3.8	None 2 years
P14	Not Dilated	42.2	71.9	27.5	0.555	0	5.2	None 2 years
P15	Dilated	60.6	74.1	38	0.733	34.1	5.5	None 2.5 years
P16	Dilated	64.4	70.6	33	0.823	15	4.6	None 3 years
P17	Not Dilated	42	47.7	25.5	0.630	33.4	4.7	None 1 year
P22	Dilated	61	73	36.7	0.630	0	4.8	None 3 years

**Table 4.1:** Patient conditions and HM2 LVAD implantation features.

Patient ID	Ventricular Features					LVAD Features		Complication occurred after LVAD implantation
	LV Condition	VD (mm)	VL (mm)	MV (mm)	F <sub>LVSI</sub>	IC Implanted Angle (°)	Q (L/min)	
P2	Not Dilated	45	62.9	29.5	0.700	25	5.3	stroke 8 months
P18	Dilated	61	73	36.7	0.800	31	6	None 3 years
P19	Not Dilated	53.7	60	31.6	0.785	21.	3.6	None 1.5 years
P20	Dilated	59.5	70.1	33	0.645	16.4	4.8	None 3 years
P23	Dilated	56.4	86.9	34.4	0.788	15	4.4	None 3.5 years

**Table 4.2:** Patient conditions and HM3 LVAD implantation features.

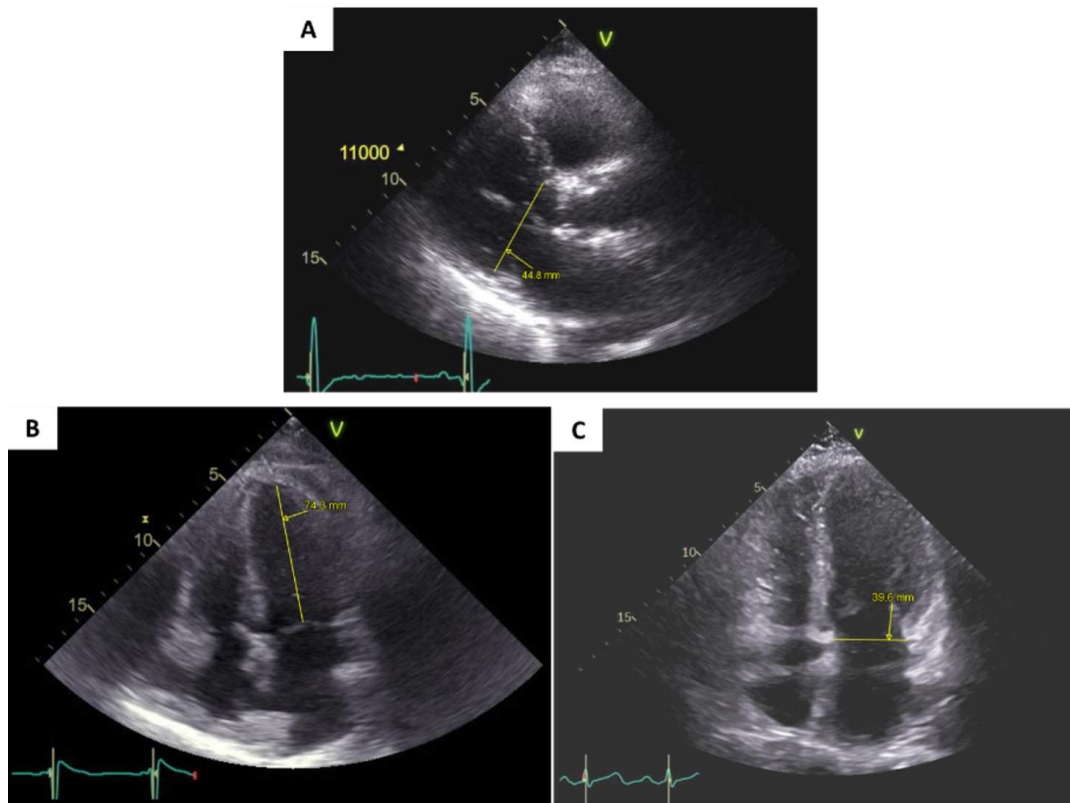


**Figure 4.8:** LV measures in diastolic phase from Ultrasound images of LV-D measure in long axis parasternal view (A) and measures of LV-H and VM-D in 4-chamber view (B and C, respectively).

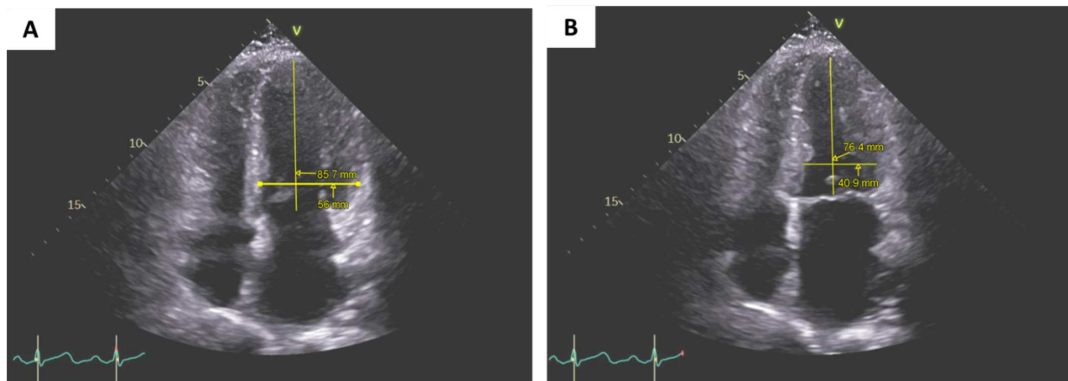


**Figure 4.9:** Ultrasound images during diastolic (A) and systolic (B) phases of LV-D and LV-H measures (for the same left ventricle) in 4-chamber view.

#### 4.4.2 Parameters definition

**Filling and clearing settings:** As explained previously, different settings of RIC are possible: for the filling phase, the Left ventricle Volume (VL) could be filled partially or totally and for the clearing phase, the clearing could be proportional to the Filling Time (FT) or fixed. The impact of different RIC settings on the PTPM performance is investigated (Table 4.3).

Area Under Curve (AUC) of the Receiver Operating Characteristic (ROC) curve eval-



Figure 4.10: Measure of IC implantation angle on CT-scan.

Setting	Filling phase (% VL)	Clearing phase (%FT)
Set 1	100	12s (Fixed)
Set 2	70	70
Set 3	100	50

Table 4.3: Filling and clearing phases investigated configurations.

uates the performance of the marker (Kamarudin et al., 2017). A higher AUC indicates a better performance (Hajian-Tilaki, 2013; Mandrekar, 2010). ROC curves related to each configuration were plotted for HM2 implanted patients (14 patients). Results are illustrated in Figure 4.11. We can observe that the AUC is the highest for Set 1. To obtain the best performance for PTPM, Set 1 (filling: 100% VL / clearing: 12 is adopted.

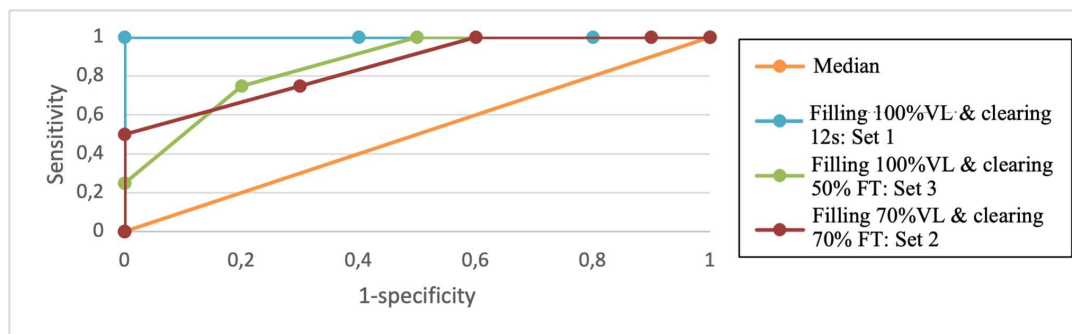


Figure 4.11: ROC curve of different filling and clearing phases for HM2 patients.

**Thrombogenic threshold settings:** The Youden Index (YI) derived of the ROC curve is used to interpret and evaluate PTPM. It is defined as the maximum potential effectiveness of the marker. It is usually used for “optimal” threshold definition as a

Threshold ( $10^{-3}$ )	Sensitivity	1-Specificity	J
0.2	1	1	0
0.3	1	0.8	0.2
0.4	1	0.4	0.4
0.5	1	0	1 (YI)
0.6	0.25	0	0.25
0.7	0	0	0
0.8	0	0	0
0.9	0	0	0

**Table 4.4:** Youden Index identification.

decision-making tool (Zhou et al., 2011). YI also evaluates the performance of the marker. A value of 1 reflects a perfect marker while a value of 0 reflect the inability of the marker to discriminate between the diseased and non-diseased patients (Bantis et al., 2019). YI is defined as follows:

$$YI = \max(J) \quad (4.24)$$

with  $J = \text{Sensitivity} + \text{Specificity} - 1$

Table 4.4 illustrates J computation for each threshold of the HM2 implanted patients. We conclude that the optimal thrombogenic threshold is set to 0.5 ( $YI = 1$ ). It is highlighted on the ROC curve through a red circle (Figure 4.12).

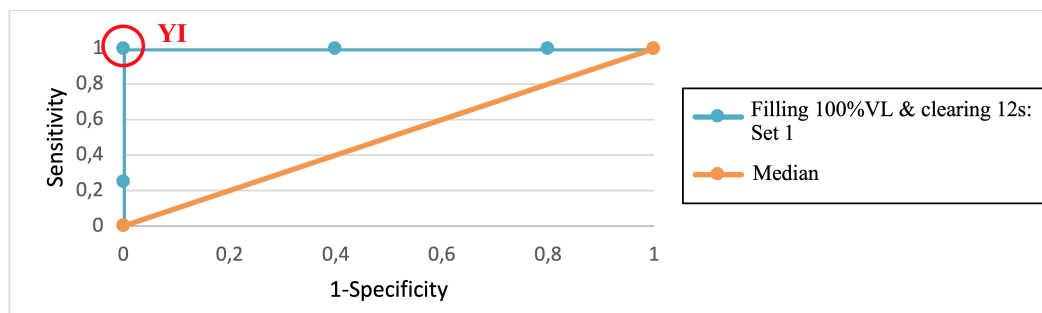


**Figure 4.12:** Youden Index identification on the ROC curve.

#### 4.4.3 PTPM: comparison to clinical outcome

PTPM is applied to configurations of two set of clinical data: HM2 implanted patients (Table 4.1) used for PTPM settings (RIC setting and thrombogenic threshold) and HM3 implanted patients (Table 4.2) used to check the performance of PTPM when a pump change occurs. Results are compared to clinical outcome.

Table 4.5 and Table 4.6 illustrate obtained results for HM2 and HM3 implanted patients, respectively. In the first column, patients IDs are coloured according to their clinical outcome: those coloured in red are patients that presented LVAD related complications (stroke or pump thrombosis) and those in green are patients that did not present any LVAD related complications. In the third column, PTPM results are coloured according to thrombogenic threshold: those coloured in light red and light green are considered as cases associated with high and low thrombogenic potential, respectively. It should be noted that from this point onward, PTPM results are presented with a scale of  $10^{-3}$ . For both data sets (HM2 and HM3), the marker is coherent with clinical outcome as it seems able to accurately distinguish between patients with and without LVAD related complications.

Patients IDs	IC implanted angle (°)	PTPM ( $10^{-3}$ )
P1	60	0.50
P3	45	0.33
P4	30	0.57
P5	30	0.57
P8	20	0.20
P9	50	0.47
P10	65	0.67
P11	20	0.41
P12	0	0.45
P13	30	0.39
P14	0	0.46
P15	35	0.33
P16	15	0.34
P22	0	0.22

Clinical outcome:	
	No LVAD related complications
	LVAD related complications
PTPM result:	
	Low thrombogenic potential
	High thrombogenic potential

**Table 4.5:** PTPM obtained for HM2 implanted patients.

## 4.5 PTPM: applications for decision support

PTPM is used to investigate the influence of IC and LV features on the thrombosis risk. Three features are considered: IC angulation, IC length and LV diameter.

Patients IDs	IC implanted angle (°)	PTPM ( $10^{-3}$ )
P2	25	0.53
P18	30	0.43
P19	20	0.24
P20	15	0.35
P23	15	0.21

**Table 4.6:** PTPM obtained for HM3 implanted patients.

#### 4.5.1 PTPM: Influence of IC angulation

The influence of IC angulation on the thrombogenic potential is investigated. The aim is to define the optimal IC angulation, associated with the least thrombogenic potential. Different IC angulations were considered for each patient (HM2 and HM3 patients). The maximum IC-AD recorded was chosen as the limit for the angulations range (4.25).

$$\text{ICAD} = 10.i; \quad i = 0, \dots, 6 \quad (4.25)$$

Table 4.7 illustrates PTPM associated with each IC angulation and the mean obtained for each patient (19 patients). As already mentioned, the patients ID column is coloured according to clinical outcome: in red are patients that presented LVAD related complications and in green are patients that did not present any LVAD related complications. PTPM results are also coloured according to thrombogenic threshold: light red and light green are considered as cases associated with high and low thrombogenic potential, respectively. For each patient, values written in bold highlights the IC angulation associated with the highest PTPM while values written in bold and underlined highlights the IC angulation associated with the least PTPM. When necessary, PTPM values are compared at the order  $10^{-6}$  to define the IC angulation associated with the highest or the least thrombogenic potential.

Looking into the obtained results, IC angulation does influence the thrombogenic potential. The mean PTPM is above the thrombogenic threshold for patients with LVAD related complications ( $\text{PTPM} \geq 0.5$ ) while the mean value is under the thrombogenic threshold for patients without LVAD related complications ( $\text{PTPM} < 0.5$ ). This suggest that we could categorise patients according to whether they have a thrombogenic or non-thrombogenic profile.

We notice that some non-complicated patients, such as P3, P8, P20 and P23, have a very low mean value, and their PTPM is slightly influenced by the IC angulation, especially for P8 and P23. Some complicated patients such as P2 and P10, although the

	0	10	20	30	40	50	60	Average
P1	<b>0.87</b>	0.46	0.74	0.43	<b>0.38</b>	0.61	0.50	0.57
P2	0.53	<b>0.52</b>	0.53	0.54	0.53	0.61	<b>0.67</b>	0.56
P3	0.23	0.26	<b>0.05</b>	0.31	0.32	<b>0.33</b>	0.32	0.26
P4	<b>0.48</b>	0.50	0.57	0.57	<b>0.68</b>	0.66	0.55	0.57
P5	<b>0.45</b>	0.51	0.56	0.57	0.59	<b>0.60</b>	0.59	0.55
P8	<b>0.19</b>	0.20	0.20	0.20	0.23	<b>0.25</b>	0.22	0.21
P9	0.41	0.45	0.42	0.39	<b>0.47</b>	0.47	<b>0.38</b>	0.43
P10	0.68	0.65	<b>0.68</b>	0.62	0.63	0.63	<b>0.51</b>	0.63
P11	0.57	<b>0.68</b>	0.41	<b>0.40</b>	0.41	0.47	0.56	0.49
P12	0.45	0.44	<b>0.40</b>	0.46	0.52	<b>0.64</b>	0.54	0.49
P13	0.67	<b>0.75</b>	<b>0.31</b>	0.39	0.37	0.35	0.36	0.46
P14	0.46	0.44	0.45	<b>0.53</b>	<b>0.40</b>	0.44	0.47	0.46
P15	0.33	<b>0.41</b>	0.35	0.28	0.30	<b>0.21</b>	0.38	0.32
P16	0.37	<b>0.41</b>	0.39	0.38	<b>0.25</b>	0.28	0.32	0.34
P18	0.49	<b>0.60</b>	0.57	0.43	<b>0.34</b>	0.39	0.46	0.47
P19	0.27	0.28	0.24	<b>0.22</b>	<b>0.41</b>	0.26	0.34	0.29
P20	0.30	0.32	0.32	0.35	0.26	<b>0.51</b>	<b>0.25</b>	0.33
P22	0.22	0.21	0.14	0.19	0.22	<b>0.12</b>	<b>0.29</b>	0.20
P23	0.21	0.21	0.22	0.22	0.23	<b>0.24</b>	<b>0.15</b>	0.21

**Table 4.7:** PTPM: influence of IC angulation.

PTPM is high for all angulations, its variation regarding IC angulation is significant between the highest and lowest PTPM. For P2, PTPM varies from 0.52 to 0.67 (+31%) for 10° and 60° angulations respectively and for P10, PTPM varies from 0.51 to 0.68 (+33%) for 60° and 20° angulations, respectively. If taking into account before LVAD implantation, the thrombogenic potential may be minimized.

For some patients, IC angulation may be a crucial factor. Indeed, some patients with a non-thrombogenic profile might suffer from LVAD related complications, when the IC is implanted in a specific angulation range. This is the case when the IC implanted angle is beyond 40°, for P12, or slightly deviated: [0°, 10°] for P13 and [0°, 20°] for P18.

When comparing only 0° and 10° results most patients (13 out of 19 patients) have a PTPM lower for 0° angulation than 10°. Although these observations are true on a reduced scale, when looking at a wider range of angulation, it could be noticed



an aligned IC is not systematically the least thrombogenic angulation. From these results, two main observations are concluded. Apical implantation with a perfectly aligned IC along the LV long axis, may not always be the ideal configuration and no IC specific angulation range is found to be the least thrombogenic for all patients. The IC angulation does influence the thrombogenic potential and this influence tightly depends on LV anatomy. Hence, conducting a preoperative study is mandatory to define the recommended IC angulation specific for each patient.

In the next section, the influence of IC insertion on of LV anatomy, especially LV diameter and its impact on thrombogenic potential is investigated.

Variation	LV-D (mm)	F <sub>AC</sub>
Config 1 (80%)	33.76	0.481
Config 2 (90%)	37.98	0.511
Config 3 (100%)	42.20	0.555
Config 4 (110%)	46.42	0.569
Config 5 (120%)	50.64	0.599

**Table 4.8:** Variation set of LV-D and its influence on the anatomical correction factor.

#### 4.5.2 PTPM: LV diameter

Depending on the LV diameter (LV-D), the geometry of the implanted IC may impact the LV haemodynamic, thus, thrombosis risk. This is a valuable information that may influence the clinicians' choice of the implanted LVAD, when investigated beforehand. These analyses were performed considering a slight IC angulation ( $0^\circ$ ,  $10^\circ$ ), likely to occur during the surgical procedure.

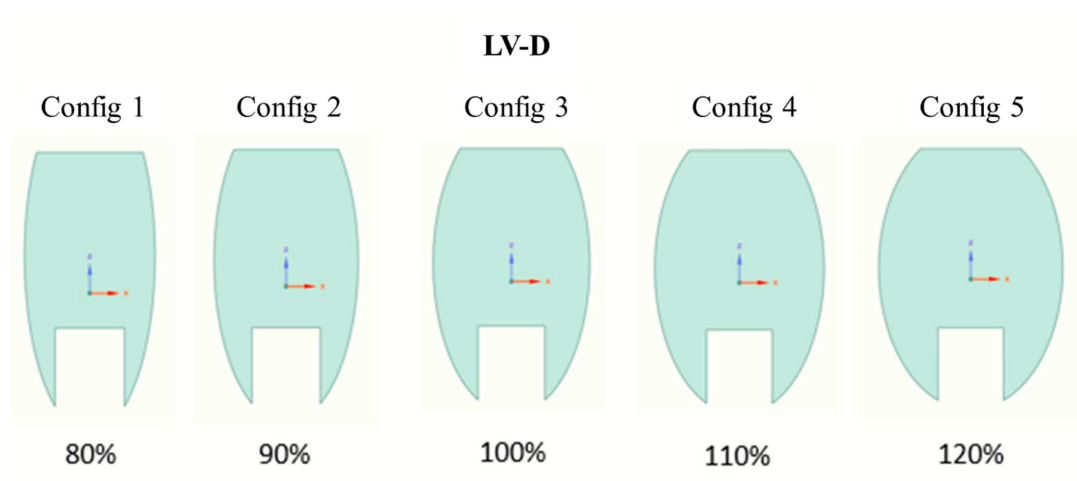
For the same pump, a variation ( $\pm 20\%$ ) of ventricular diameter is investigated and PTPM is considered for each configuration. Table 4.8 presents the variation set performed on LV-D and the resulting ventricular shapes are illustrated in Figure 4.13. These analyses are carried out on P14 (VL = 71.9 mm; Q = 5.2 L.min<sup>-1</sup>) for two different IC angulations [ $0^\circ$ ,  $10^\circ$ ]. For F<sub>AC</sub> computation, the sphericity index in the systolic phase was considered the same for all cases (SI<sub>ES</sub> = 0.493).

Table 4.9 illustrates the impact of LV-D on PTPM. Results are coloured according to the thrombogenic threshold as mentioned previously. Arrows in red and green point toward the directions where the PTPM increases and decreases, respectively. Overall, PTPM increases when the LV diameter is too small (80% and 90%) or too large (120%) which is consistent with clinical observations. We can also notice that for extreme cases, when the ventricle is relatively too small (80%) or especially, too large (120%), PTPM is higher when the IC angulation is slightly deviated ( $10^\circ$ ). For

Config	0°	10°		
1	1.068	1.093	↑	80%
2	0.564	0.531		90%
3	0.460	0.436	↓	100%
4	0.369	0.370		110%
5	0.634	0.955	↓	120%

**Table 4.9:** Influence of LV-D on PTPM.

median cases, PTPM is slightly lower when the IC is deviated at 10°. This observation would reflect that a small angulation of the IC might enhance the haemodynamics within the ventricle and reduces stagnation within these regions.




**Figure 4.13:** Influence of LV-D variation on ventricular shape.

### 4.5.3 IC length

IC insertion length is also an influencing feature that is under investigation. In the previous chapter (section 3.3.3), IC length was investigated for three different IC lengths (10 mm, 20 mm, 34 mm) while considering two different angulations [0°, 10°]. The analysis was carried out for two cases. These cases are P3 and P14.

Table 4.10 illustrates the obtained results. The red arrow points toward the direction where the PTPM increases. For all the investigated configurations, PTPM is under the thrombogenic threshold, which is coherent with previous observations as both patients (P3 and P14) have non-thrombogenic profiles. For both patients, PTPM increases proportionally to the IC length. This increase differs depending on the

	P3		P14	
	0°	10°	0°	10°
10 mm	0.10	0.24	0.33	0.38
20 mm	0.23	0.26	0.46	0.44
34 mm	0.31	0.28	0.47	0.49



**Table 4.10:** PTPM: influence of IC length combined with IC angulation for two patients.

anatomy as between an insertion length of 10 mm and 34 mm, PTPM increases 3 and 1.5 times for P3 and P14, respectively. The thrombogenic potential is mainly higher for 10° angulation.

So far PTPM seems to be able to recognise thrombogenic profiles and configurations. It was observed that IC features (angulation, length) do influence the thrombogenic potential related to LVAD implantation. Nevertheless, the anatomical factor seems to be the most determining factor of the extend of this influence on thrombogenic potential. Considering the simplified geometry of our model, the limitations and perspectives of PTPM are investigated.

## 4.6 PTPM: limitation and perspective

The objective is to analyse the main limitation of our model and to open some perspectives. Simulations of a 3D patient-specific geometrical model are used to analyse the influence of the shape approximation and the in-plan definition of the marker.

### 4.6.1 3D patient-specific model: Model presentation

The Geometrical model used in this section was developed previously by our team (Collin, 2018). The model generation steps are illustrated in Figure 4.14. The 3D model of the Left Ventricle (LV) was generated from a preoperative contrast-enhanced CT scan of an LVAD implanted patient. Subsequently, the CT scan was segmented using the multi-atlas segmentation method (Kirişli et al., 2010). The obtained result (3D mesh of LV endocardium, left atrium and aorta) was built with ITK-Snap software (Yushkevich et al., 2006). The MV was determined by the mid-plane of the contact area between the LV and left atrial meshes, while the aortic valve was determined with the LV and aortic meshes. A smoothing step was then conducted on FLUENT to improve the quality of the mesh. This final mesh is characterized by a minimum and maximum cell size of 0.5 to 2 mm. The selected patient was implanted with a HM II pump. The 3D geometry of the IC pump (HM II) has been designed as a cylinder

of 53 mm high, an inner diameter of 18mm and a thickness of 0.5 mm. The created IC geometry is then inserted (20 mm) into the LV.

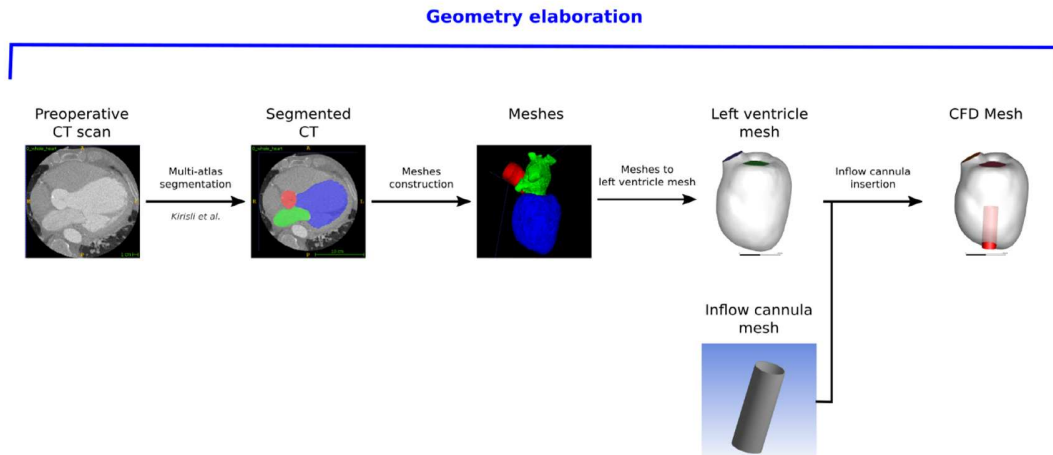


Figure 4.14: Illustration of the different geometry elaboration steps. <sup>1</sup>

Once the model is ready (designed and meshed), the numerical model is defined. The myocardial wall was considered a rigid material and the aortic valve was assumed close. A constant static pressure (0 Pa) was applied on the MV inlet surface, while a continuous mass flow rate of  $5 \text{ L} \cdot \text{min}^{-1}$  was set on the IC outlet surface. Blood was modelled as a Newtonian fluid with a density of  $1060 \text{ kg} \cdot \text{m}^{-3}$  and a viscosity of  $0.004 \text{ kg} \cdot \text{m}^{-1} \cdot \text{s}^{-1}$  Herman (2010). Figure 4.15 summarizes the numerical model. It should be noticed that except for the Large Eddy Simulation (LES) flow assumption, the numerical model is the same as the proposed 2D models. The turbulent flow assumption was tested with this model to enhance vortices formation.

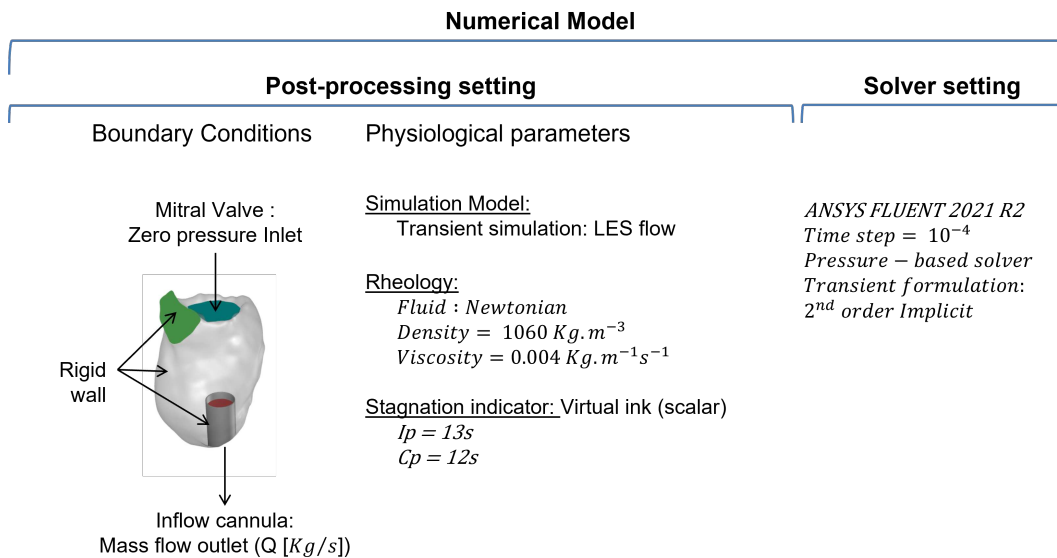
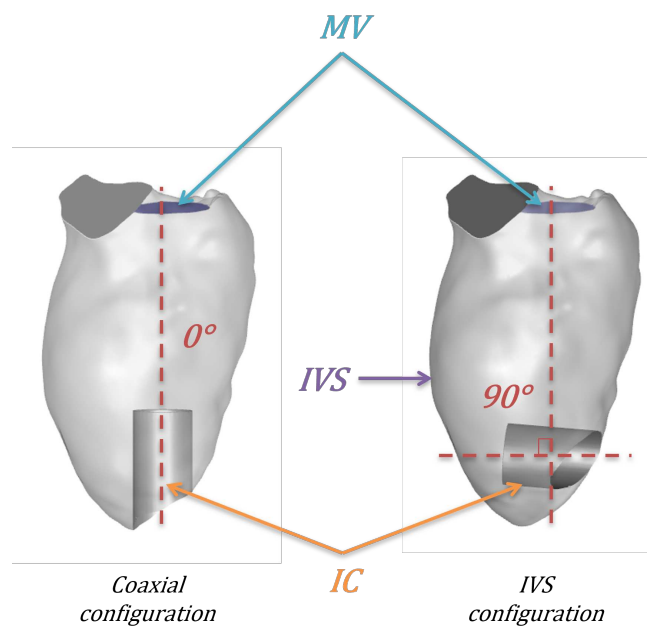


Figure 4.15: Numerical model of the CFD simulation.

1. Source (Collin, 2018)

Patient selection was performed based on its extreme IC angulation. The IC was implanted not at the LV apex but toward the IVS with a deviation of  $90^\circ$  from the LV long axis. This patient suffers from an hypo-density of the frontal lobe after 3.5 years of being implanted. His follow up was carried out in a different hospital, so due to lack of data only diastolic ventricular shape was taken into account for the PTPM anatomical correction factor ( $F_{AC} = 0.654$ ). Two configurations were considered: a coaxial configuration where the IC is implanted at the apex facing the MV as recommended by clinical guidelines and an IVS configuration which is the IC implanted angle (Figure 4.16). The modelled patient has a pump flow rate of 5 L/min.



**Figure 4.16:** Investigated Cases: Apical ( $0^\circ$ ) and IVS ( $90^\circ$ ) configurations.

#### 4.6.2 PTPM limitation: shape approximation

This analysis aims to evaluate how the PTPM is impacted by the 2D assumption on ventricular shape and haemodynamic. For that, two models are considered: the proposed 2D model and its corresponding 3D patient-specific model, presented above. For both models, two extreme IC angulations are studied: Apical and IVS configurations. PTPM is applied on both 2D models and their corresponding plans in the 3D models (Figure 4.17), results are compared between different configurations and confronted to the clinical outcome.

Table 4.11 illustrates the obtained results. As already mentioned, PTPM values are also presented with a scale of  $10^{-3}$ . 2D results are coloured according to the thrombotic threshold.

PTPM values are much higher for 3D models than for 2D models. This result is expected as the WSS in 3D simulations is significantly higher than 2D simulations and

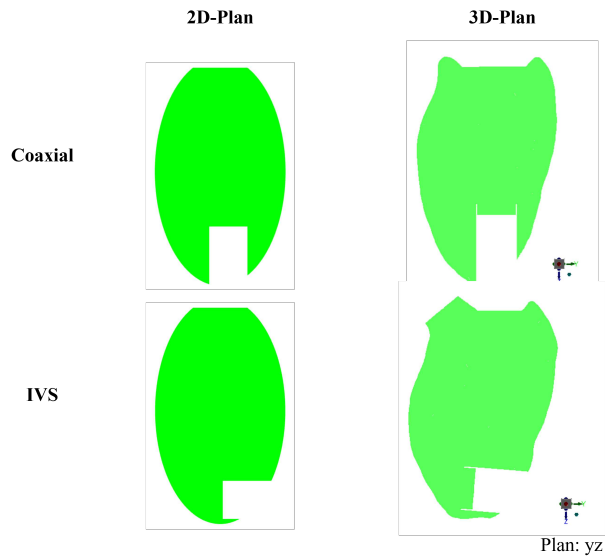


Figure 4.17: 2D proposed model and their corresponding 3D planes.

	2D	3D
Coaxial	0.65	2.7
IVS	0.69	6.9

Table 4.11: Investigated Cases.

vortices formation is enhanced with turbulent flow.

For both models, PTPM results present the same tendency as the thrombogenic potential is higher for IVS configuration. PTPM results are also coherent with clinical outcomes. Since the PTPM of 2D models is above the thrombogenic threshold for both angulations, this patient may have thrombogenic profile.

### 4.6.3 PTPM limitation: analysis plan definition

For this analysis, PTPM is evaluated within a plan and its evaluation considers a 3D ventricular haemodynamic. The 3D model presented previously with its two IC configurations is investigated. Several plans are considered: at the centre of the cannula, for coaxial and IVS configurations, and at a distant plan from the IC area. These plans are considered for each Cartesian axis (Figure 4.18). We can notice that for both configurations, the distant plan is in the middle of the ventricle in the xy plan while in the other plans, it is rather on the edge of the ventricle.

For each plan, PTPM results for coaxial and IVS configurations are presented in Table 4.12 and Table 4.13, respectively. The average value of PTPM at the IC centre plans, along cartesian axis, is coloured in blue and the average value of PTPM at the distant plans, along cartesian axis, is coloured in light orange for both configurations.

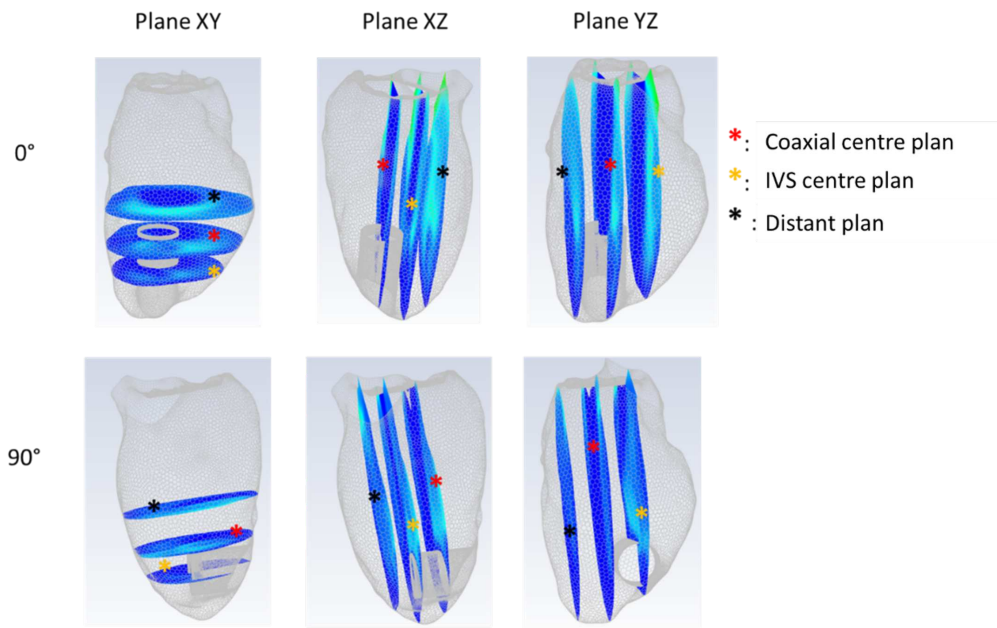


Figure 4.18: PTPM: investigated plans.

Overall, PTPM, whether per plan or per location, is higher for IVS than for coaxial configurations. The average values of PTPM for longitudinal plans (yz and xz) are close for both configurations. This suggests that considering one longitudinal plan might be sufficient to evaluate PTPM within the LV long axis. For distant plans, thrombogenic potential is considerably more important within yz and xz planes than within xy plan for both configurations. These results are coherent as yz and xz distant plans are located close to the LV wall which is known to be a stagnation region. In average, having a higher PTPM value (at distant plans) for IVS configuration, suggests that stagnation risk is higher for IVS configuration. For the IC centre plans, PTPM is almost three times higher for IVS than coaxial configurations. This difference might be explained by the higher WSS (not shown), especially around the IC for IVS configuration.

Coaxial configuration	Coaxial Centre plane	IVS Centre plane	Distant plane	Average per Plane
xy	3	3.6	2.3	3.0
yz	2.7	2.2	5	3.3
xz	1.6	2.9	5.8	3.4
Average per location	4.2	2.9	4.4	Total average: 3.2

	Plane at the centre of the IC
	Distant plane

Table 4.12: PTPM applied on different planes of the Coaxial configuration.

Coaxial configuration	Coaxial Centre plane	IVS Centre plane	Distant plane	Average per Plane
xy	6.5	7.8	4.1	6.1
yz	3.5	6.9	5.4	5.3
xz	3.8	5.7	6.4	5.3
Average per location	4.6	6.8	5.3	Total average: 5.6

**Table 4.13:** PTPM applied on different planes of the IVS configuration.

Thrombogenic potential is significantly higher for IVS than for coaxial configurations regardless of the analysis plan. PTPM, as currently defined, seem able to compare thrombogenic potential associated with several 3D configurations. Considering one plan is deemed sufficient to identify the most and the least thrombogenic configurations. Nevertheless, for a thorough investigation, two plans could be used: an IC centre plan and a longitudinal-distant plan to provide insight into blood stagnation and WSS, respectively.

The proposed 2D-PTPM seems coherent and relevant with 3D models. It should be noticed that these results are preliminary and that at this level of 3D analysis, the marker is used as a relative thrombogenic potential, capable to compare two given configurations. To obtain an absolute marker for 3D applications, more cases should be investigated to adjust the thrombogenic threshold. Another advantage of this marker is that PTPM definition have the ability to be extended to a 3D-PTPM by developing the vortices segmentation process, but at the cost of a higher computation time. This could be useful for further research and analysis.

## 4.7 Summary and conclusion

In this chapter, the Personalised Thrombogenic Potential Marker (PTPM) was proposed. It is a vortices-based marker that considers patients' clinical conditions such as LV morphology (geometry, ventricular shape in diastolic and systolic phases), IC specific features (geometry, implanted angle) and monitored data (pump flow rate). PTPM is an absolute marker that does not require a comparative configuration and is coherent with clinical outcomes. Our results showed that IC angulation does influence the thrombosis risk and this influence depends greatly on LV anatomy. Indeed, no specific IC angulation was neither optimal nor recommended for all patients. We noticed that the mean value of PTPM obtained for a wide range of simulated angulations could characterise the thrombogenic profile of the patient. These profiles reflect the tendency of LVAD related complications to occur. Results of the LV-D influence showed that for a LV rather small or relatively dilated, the thrombosis risk increases which is coherent with clinical observations. Results of the influence of IC



length showed that thrombosis risk increases with IC length, especially when the IC is deviated. Finally, we confronted PTPM results of a 2D model with a 3D patient-specific model for two configurations. Preliminary results on the 3D model had the same tendency with those obtained with the 2D model.

# Conclusion and perspectives

Heart Failure (HF) is a clinical condition where the heart fails to sustain the body needs. Its severity depends on the ability of the heart to pump blood and is classified into four stages. Once the end-stage is reached a Heart Transplant (HT) is required. However, facing heart graft shortage, Mechanical Circulatory Support (MCS) devices implantation are the only alternative. Depending on the condition of the patient, these devices could be used as a bridge to transplant or a destination therapy for patients that are ineligible for HT. Although MCS implantation has proven to be a sustainable therapy for HF patients, it is associated with adverse events, especially in the long-term consisting of thromboembolic events and pump dysfunction associated with thrombus formation.

In the literature, research took interest in the interaction of MCS devices with patients anatomy and physiology. Two main issues arose: morphological and fluid issues. The morphological constraints are mainly related to the available intra-thoracic space for MCS implantation and chest closure. In the case of Left Ventricular Assist Device (LVAD) implantation, this issue may result in Inflow Canula (IC) angulation which influences the haemodynamic within the ventricle. This brings to the second issue related to fluid constraints. Some reported works assumed that thrombosis would be related to IC features (tip, length and angulation). They investigated the influence of these features on Left Ventricle (LV) haemodynamic and attempted to evaluate the thrombosis risk through different means. In particular, Computational Fluid Dynamics (CFD) approaches have been used to analyse different Quantities Of Interest (QOI) in sought to asses blood stagnation, platelet activation and thrombosis risk as they are complex phenomena not fully grasped. Several issues remain unanswered since results are preliminary and even contradictory. The need to develop a marker able to predict thrombosis risk is still an open issue.

In this context, our work focused on thrombosis associated with LVAD implantation for HF patients. Using CFD computation, our aim was twofold: i) to better understand the behaviour of several QOI regarding the influence of some IC features

(length and angulation) and ii) to develop a personalised thrombogenic potential marker able to evaluate the thrombosis risk associated with IC features, especially IC angulation.

For the haemodynamic analysis, a generic 3D model was used as a reference to verify the 2D assumption where the same tendencies regarding IC angulation were found. A simplified 2D model that takes into account LV anatomy ratio and IC flow rate was proposed. This model was used to investigate the influence of a wide range of IC angulations and different IC lengths on the haemodynamic for two distinct LV shapes based on several QOI: velocity path-lines, Remaining Ink Concentration (RIC) and Wall Shear Stress (WSS). The 2D analysis emphasised the interest of considering the vortices formed within the ventricle. Indeed, IC angulation analysis highlighted that to pursue low velocity and RIC within vortices would allow a better understanding of LV haemodynamic. we distinguished three angulation ranges where QOI behaviour was different. IC length analysis concluded that IC angulation increases the impact of the IC length on LV haemodynamic.

Investigating QOI behaviour on a wide range allowed a better understanding of LV haemodynamic regarding IC features. Although the straightforward analysis of different QOI separately, allowed a considerable insight into blood stagnation and platelet activation, it could not be of immediate use for clinical decision support.

A Personalised Thrombogenic Potential Marker (PTPM) was proposed to predict the thrombosis risk. It considers platelet activation through WSS, Anatomical Correction Factor ( $F_{AC}$ ) through Left Ventricular Sphericity Index (LVSI) during diastolic and systolic phases and blood stagnation through low velocity, high RIC and swirling strength within vortical regions. By combining the 2D model and PTPM a pipeline of simulation adapted to clinical cases was proposed. This pipeline was applied to several clinical cases (19 patients implanted with HeartMate 2 (HM2) and HeartMate 3 (HM3)) to assess the marker settings, thrombogenic threshold (both for HM2 patients) and efficiency by confronting the marker results to the clinical outcome (for HM2 and HM3 patients). A wide range of IC angulations was investigated and we observed that PTPM seemed able to recognise thrombogenic configurations and highlight thrombogenic profiles. Our results also showed that the least thrombogenic IC angulation depends tightly on the LV anatomy. The influence of IC length on the PTPM for two IC angulations was also investigated and we noticed that the increase of IC length increases thrombosis risk. The increase of this risk is enhanced with IC angulation and its extent depends on the LV anatomy. Additional results showed that the PTPM obtained for a 2D model was coherent with the PTPM obtained for a 3D patient-specific model.

To the best of our knowledge, this is the first work where the proposed model is parameterised with patient and monitoring data (LV anatomical ratio, IC clinical an-

gulation and pump Flow Rate ( $Q$ )). This personalised aspect is emphasised with the proposed PTPM by considering the LVSI during diastolic and systolic phases. This absolute marker has the ability to evaluate the thrombosis risk related to a specific configuration without requiring a comparative configuration. Its definition has the potential to be adapted to different complexity levels according to the user interest (2D, 3D or 2D-3D).

However, this work presents some limitations. Since the number of implanted devices remains limited, the number of clinical cases used to investigate the PTPM is reduced. Acquiring more clinical data from neighbouring hospitals would allow to validate the PTPM on more cases. The Aortic Valve (AoV) is not taken into account and could be represented in the 2D model. In practice, the measurements of the long AoV diameter of each patient and its associated ejection fraction could be collected and considered in the CFD simulations. It would be interesting to analyse the influence of the AoV opening on the LV haemodynamic and its impact on the PTPM. A 3D approach of the marker could also be developed to deepen its use on 3D models. However, it should be taken into account that calculations are time-consuming and that a traditional computing machine is not a suitable solution for wide ranging investigations. Innovative solutions such as the Cloud or computing clusters may significantly reduce computation time. It would also be interesting to consider simulations taking into account heartbeats. Although HF patients have a reduced LV contractility, it remains interesting to perform heart-beating simulations, to investigate the influence of wall motions on suction events and blood stagnation, especially at the apex.

This work is a promising lead towards the ambitious objective of developing a clinical decision support system able to predict the optimal IC angulation associated with the least thrombosis risk.



# Appendices



## Total Artificial Hearts - TAH

Main developed TAH :

- Liotta-Cooley TAH is the first human-implanted TAH. It was developed by Domingo Liotta and implanted by Dr. Denton A. Cooley who is the founder of the Texas Heart Institute where the surgery was performed in 1969 as a BTT. It was an air driven double-ventricle pump (Figure A.1–(a)).
- Akutsu III TAH is the second human-implanted TAH. It was developed by Fr. Tetsuzo Akutsu and implanted by DR. Denton A. Cooley at the Texas Heart Institute in 1981 as a BTT also. Akutsu III TAH was similar to Liotta-Cooley TAH; the key differences relied on the material choice of the blood-contracting surfaces and the valves (Figure A.1–(b)).
- Sarn-3M TAH was developed by Dick Sarns. Even though in 1993, several animal implantations were performed and one animal had a 150 days survival, this TAH did not proceed beyond animal experimentation due to its large size, poor system reliability and lack of long-term durability (Figure A.1–(c)).
- Nimbus TAH was an electrohydraulic system. It was implanted in 12 calves with an average and maximal survival time of 32 days and 120 days respectively. However, the existence of many mechanical failures including wear particles in the hydraulic fluid lead to the early termination of the study preventing it from human implantation trials (Figure A.1–(d)).
- Jarvik-7 TAH was developed by willem Kolff and Robert Jarvik at the University of Utah. It was a double-ventricle pump, pneumatically driven, similar to Akutsu III TAH in terms of material choices of the chambers surfaces and valves. The first in-human implantation was performed in 1982 by Dr. William De Vries as DT. It had a survival time of 112 days. Through time, the longest survival time was of 620 days. As the device evolved its naming evolved as well



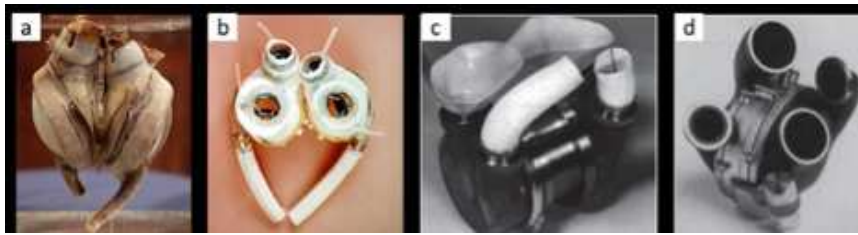


Figure A.1: TAH without FDA approval

( Symbion Aartificial Heart (1983-1991) ; CardioWest C-70 TAH (1991-2001); SynCardia temporary TAH (2004-present)). In 2004, the FDA approved its use as a BTT (Figure A.2–(a)).

- AbioCor TAH was developed by ABIOMED in Danvers, as the only fully in human-implantable, self-contained artificial heart developed between 1980 and 1990. As for Sarns-3M TAH and Nimbus TAH, this device had both, systemic and pulmonary pumping chambers made up of flexible membranes, alternately compressed however by hydraulic fluid pumped by centrifugal pump which was the key difference of the device. AbiCor carried out animal experimentation for 14 years during which the device was implanted into 120 calves and the first in-human implantation was performed in 2001 by Drs. Lauman Gray and Robert Dowling in Kentucky. The devices obtained FDA approval in 2006; however the project was shelved in 2007 (Figure A.2–(b)).
- Carmat TAH is a French product more recently developed in 2008 by Matra Défence (Airbus Group), Truffle Capital and Professor Alain Carpentier. It is electro-hydraulically driven with a shape close to that of a human heart, composed of two ventricles chambers separated into two parts by a membrane and four biological valves. It first in-human transplantation was performed in 2003 in Georges Pompidou European Hospital by Pr.Christian Latrémouille. Carmat received FDA approval in 2020 as a BTT for those who would undergo HT in the 180 days following device implantation (Figure A.2–(c)).

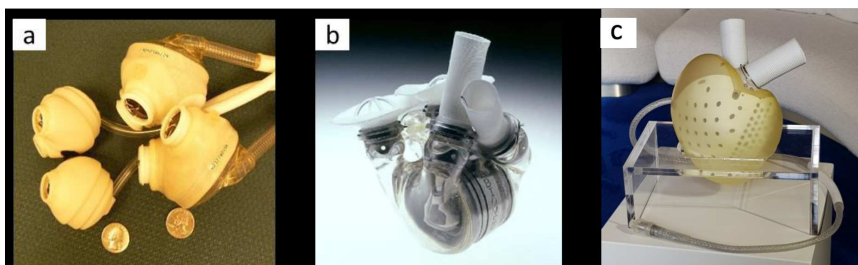


Figure A.2: TAH with FDA approval

- BiVACOR is a prototype of TAH developed by BiVACOR inc. founded in 2008 in Texas, US. It is a continuous flow magnetically powered device with a centrifu-

gal pump aiming to be implanted as DT for paediatric and adult use (Figure A.3–(a)).

- ReinHeart is a prototype of TAH developed by The ReinHeart TAH GmbH, founded in 2015 in Aachen in Germany. The ReinHeart device began its development in 2009 with an innovative electromagnetic linear drive mimicking the native heart function. It is also aiming for a DT usage (Figure A.3–(b)).

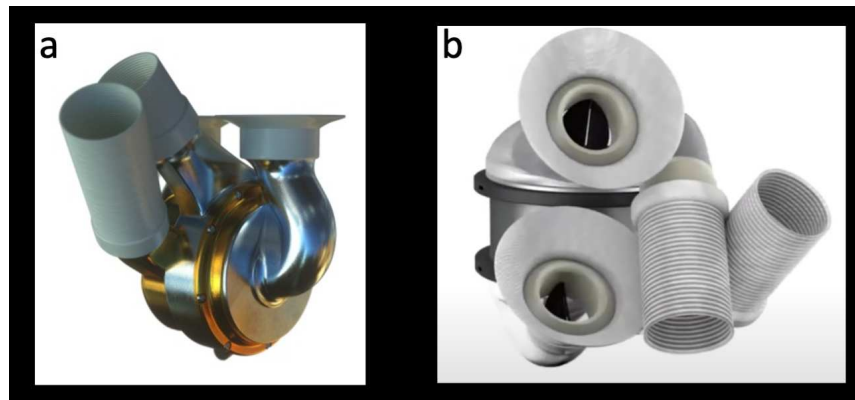


Figure A.3: TAH prototypes.



# Appendix B

## Ventricular Assist Device – VAD

First generation VADs:

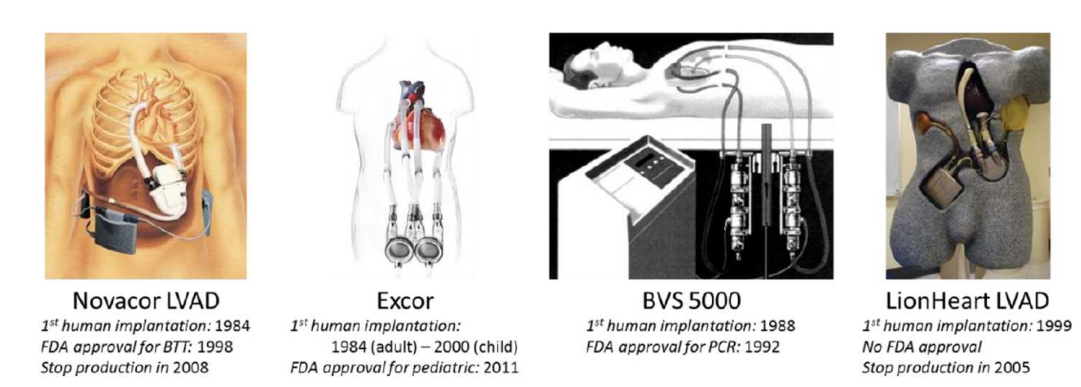


**Figure B.1:** Novacor (World Heart Corp. – US); Excor (Berlin Heart Inc. – Germany); BVS 5000 (ABIOMED – US) ; LionHeart (Arrox International Inc. – US).

Second generation VADs:

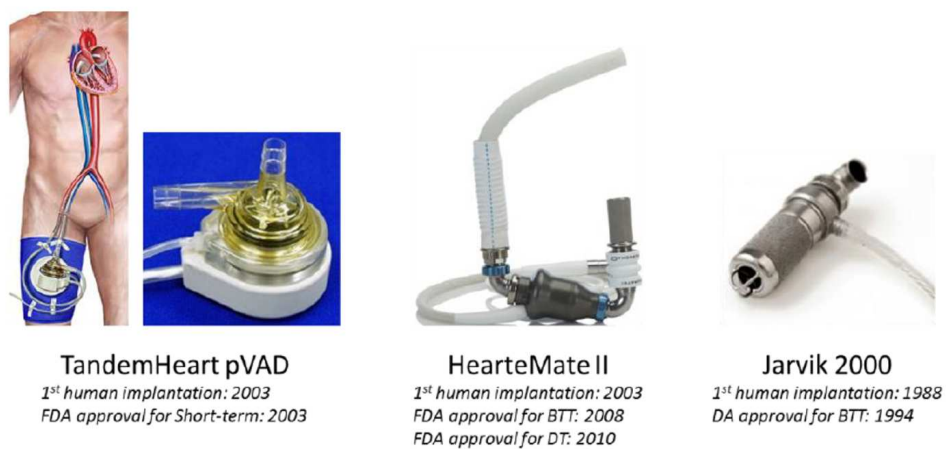


**Figure B.2:** TandemHeart (CardiacAssist, Inc. – USA); HeartMate II (Thoratec Corporation – US); Jarvik 2000 (Jarvik heart, Inc. – US).

Third generation VADs:

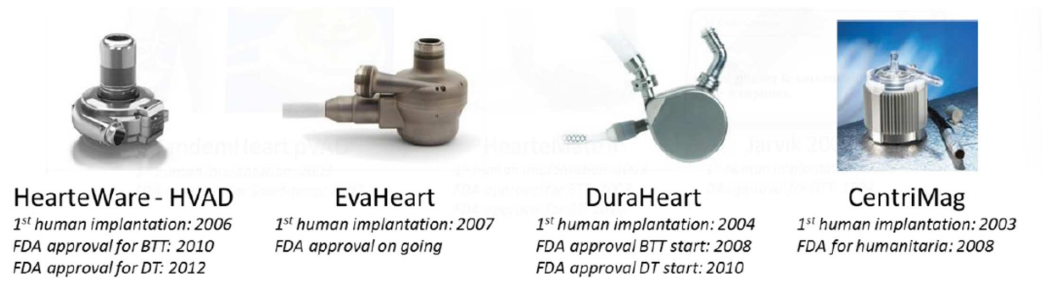


**Figure B.3:** HeartWare (Medtronic Inc. – US); EvaHeart (EvaHeart, Inc – US); DuraHeart (Terumo Corporation – Japan); CentriMag ( Thoratec Corporation – US).

## Conversion of flow rate $Q$

Flow rate [ $\text{L}\cdot\text{min}^{-1}$ ] conversion to a uniform velocity [ $\text{m}\cdot\text{s}^{-1}$ ] is performed in two steps:

- Unit conversion: where flow rate [ $\text{L}\cdot\text{min}^{-1}$ ] is converted to a flow rate [ $\text{m}^3\cdot\text{s}^{-1}$ ].
- Velocity conversion: where flow rate [ $\text{m}^3\cdot\text{s}^{-1}$ ] is converted to velocity [ $\text{m}\cdot\text{s}^{-1}$ ].

**Unit conversion:** Knowing that:

$$1[\text{L}] = 1[\text{dm}^3] \quad (\text{C.1})$$

and:

$$1[\text{dm}^3] = 0.001[\text{m}^3] \quad (\text{C.2})$$

Then:

$$Q'[\text{m}^3\cdot\text{s}^{-1}] = \frac{Q'[\text{L}\cdot\text{s}^{-1}] \times 0.001}{60} \quad (\text{C.3})$$

**Velocity conversion:** The flow rate, within a section area ( $S$ ), is computed as the following:

$$Q' = \int \int_S \vec{v} \cdot d\vec{S} \quad (\text{C.4})$$

Within a pipeline, all the particles do not travel at the same velocity. Indeed, for a laminar flow, the velocity profile across a section has a parabolic shape (Figure C.1). This velocity distribution is caused by the friction forces at the section wall.

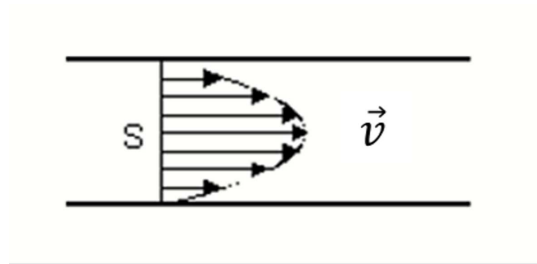


Figure C.1: Analytical velocity profile.

If the velocity at the section is considered uniform, the velocity is averaged, and it becomes independent of the section (Figure C.2).

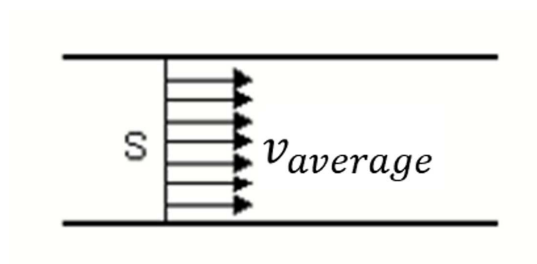


Figure C.2: Average velocity profile.

Hence, the flow rate formula becomes as the following:

$$Q'[\mathbf{m}^3 \cdot \mathbf{s}^{-1}] = \int \int_S \overrightarrow{v_{average}} \cdot \overrightarrow{dS} = v_{average}[\mathbf{m} \cdot \mathbf{s}^{-1}] \cdot S[\mathbf{m}^2] \quad (\text{C.5})$$

So, based on (C.3) and (C.5) the inlet velocity is computed as follows:

$$v[\mathbf{m} \cdot \mathbf{s}^{-1}] = \frac{Q'}{S} = \frac{Q \times 0.001}{S \times 60} \quad (\text{C.6})$$

## Mesh independence: 3D model

For mesh independence study, three different meshes with elements sizes of 1 mm, 2 mm and 3 mm were investigated. Data is exported every 0.5 s during 3 s and mean and max velocity magnitude is used as metrics for this study. The CFD simulation was performed using a second order implicit transient formulation, and Pressure Implicit with Splitting of Operators (PISO) with a pressure-velocity coupling. A second order spatial discretization was set for the pressure, momentum, and continuity equations. Convergence was achieved in each time-step ( $10^{-5}$  s) when the residuals were below  $10^{-6}$  for continuity, x, y, z. Mass imbalance did not exceed  $10^{-13}$  order.

One can observe that simulation results for meshes with elements sizes of 1 mm and 2 mm are identical for max and mean values of velocity magnitude (Figure D.1). However, results obtained with a mesh with elements size of 3 mm are different. To conclude, a mesh with elements size of 2 mm leads to simulation results that are independent of the underlying mesh. A mesh with elements size of 2 mm has been selected to perform all the simulations.

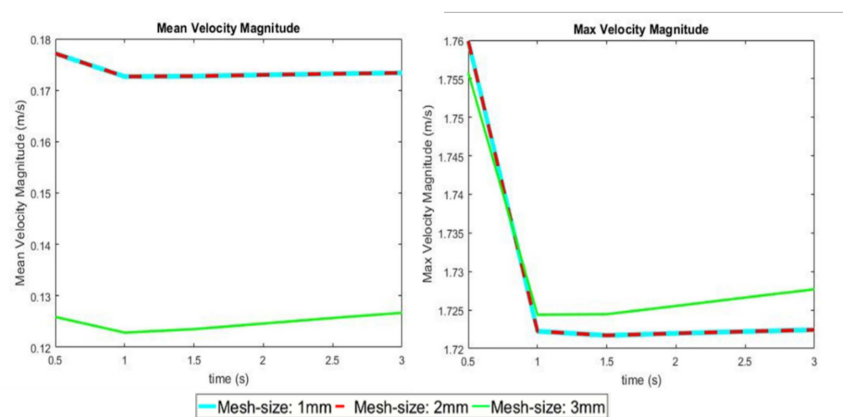


Figure D.1: Mesh independence: Velocity Magnitude.





## Mesh independence: 2D model

For mesh independence study, four different meshes with elements sizes of 0.5 mm, 1 mm, 2 mm and 3 mm were investigated. Data is exported every 1 s during 13 s and mean and max velocity magnitude were used as metrics for this study. The CFD simulation was performed using a second order implicit transient formulation, and a PISO pressure-velocity coupling. A second order spatial discretization was set for the pressure, momentum, and continuity equations. A time-step of  $10^{-3}$  s was used for meshes with elements sizes of 2 mm and 3 mm, and a time-step of  $10^{-4}$  s was used for meshes with elements sizes of 0.5 mm and 1 mm. For each mesh, these time-step ensured the Courant-Friedrichs-Lewy (CFL)  $< 1$  condition. Convergence was achieved in each time-step when the residuals were below  $10^{-6}$  for continuity,  $x$ ,  $y$  as required by the pressure-based solver.

Looking to Figure E.1, one can observe that mesh independence is reached for a mesh with elements size of 1 mm. However, 1 mm requires a time step of  $10^{-4}$  s set according to the CFL condition which results in a high computation time (Table E.1). The relative error of the obtained results for mesh with elements sizes of 2 mm and 3 mm compared to the results obtained for a mesh with element size of 1 mm is investigated. The relative error for a mesh with elements size of 2 mm is around 3% and 5.5% for mean and max velocity magnitude respectively (Figure E.2). These relative errors are considered within a tolerable range. Moreover, taking into account the time computation, residual convergences and mass imbalance which was under 1%, a mesh with size of 2 mm is considered sufficient to achieve a balance between accuracy and computational cost.

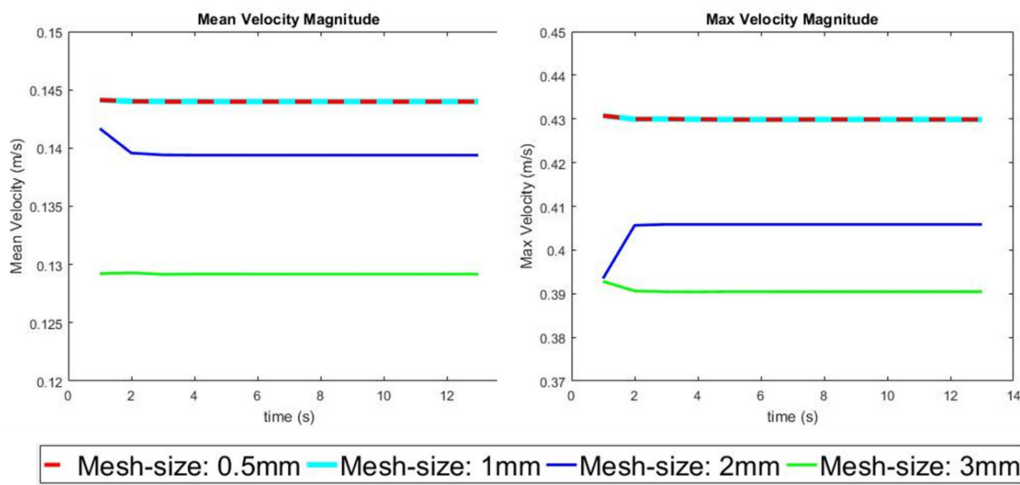


Figure E.1: Mesh independence: velocity magnitude.

Mesh size	Time computation
0.5 mm	45 – 50 min
1 mm	40 – 45 min
2 mm	2 – 3 min
3 mm	3 min

Table E.1: Computation time for 1 s of simulation time required for every mesh size.

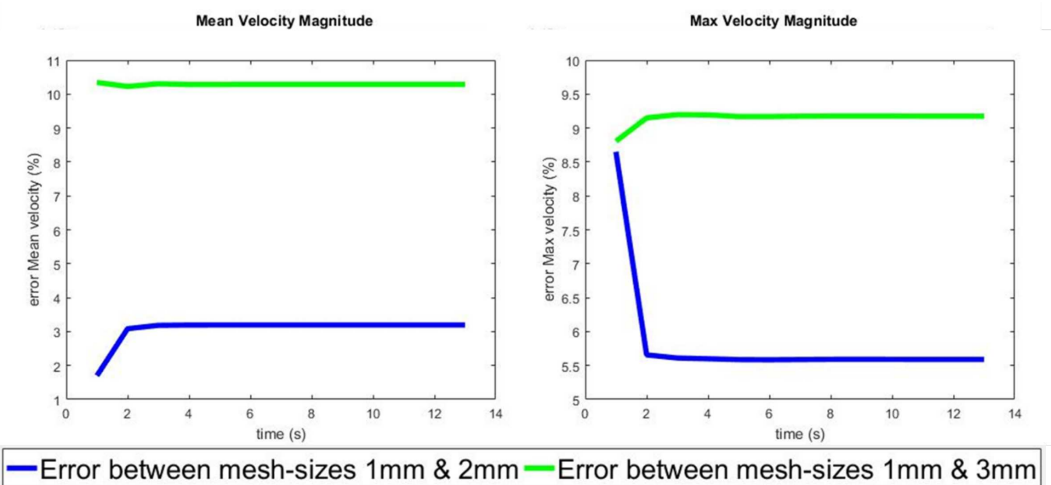


Figure E.2: Relative error for mesh size of 2 mm and 3 mm related to mean and max velocity magnitude.

## 2D model thickness

For 2D simulations, FLUENT software imposes a thickness definition. This thickness is used for various computation specific to the software, such as flow rate and areas computation. The choice of the model thickness could be arbitrary or based on significant variables such as IC surface, where the blood exits the ventricle. This thickness allows to obtain a realistic output surface of the HM2 inflow cannula.

Since the IC is modelled as a line (in a 2D plane), by adding a thickness to the model, the output IC surface becomes a rectangle (Figure F.1)

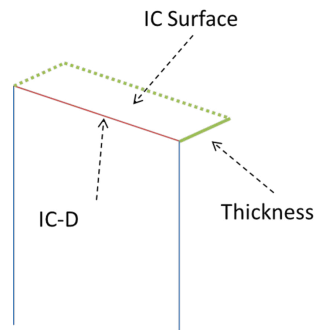


Figure F.1: Hypothetical IC output surface.

Hence, the hypothetical IC surface is computed as follows:

$$IC_{Surface} = IC-D \times Thickness \quad (F.1)$$

Knowing that IC surface of the HM2 pump is a cylinder with an internal diameter (Inflow Canula Diameter (IC-D)) of 18 mm, the output IC surface of the HM2 pump is computed as the following:

$$IC_{Surface}^{3D} = \pi \left( \frac{IC-D}{2} \right)^2 \quad (F.2)$$

Knowing that the rectangle long axis represents the IC diameter (IC-D), the thickness used for the 2D models is computed as follows:

$$\text{Thickness} = \frac{\pi}{4} \text{IC-D} \quad (\text{F.3})$$

Numerical application:

$$\text{Thickness} = 0.0014 \text{ m} \quad (\text{F.4})$$

## Bibliography

- Addetia, K., Uriel, N., Maffessanti, F., Sayer, G., Adatya, S., Kim, G. H., Sarswat, N., Fedson, S., Medvedofsky, D., Kruse, E., Collins, K., Rodgers, D., Ota, T., Jeevanandam, V., Mor-Avi, V., Burkhoff, D., and Lang, R. M. (2018). 3d morphological changes in lv and rv during lvad ramp studies. *JACC: Cardiovascular Imaging*, 11:159–169.
- Affeld, K., Scharnweber, H., and Claussen, C. (1983). The use of computer graphics to find an optimal fit for a human total artificial heart. *Transactions - American Society for Artificial Internal Organs*, 29:103–9.
- Agnetti, G., Piepoli, M. F., Siniscalchi, G., and Nicolini, F. (2015). New insights in the diagnosis and treatment of heart failure. *BioMed Research International*, 2015:1–16.
- Ahmed, M. M. E.-S., Aftab, M., Singh, S. K., Mallidi, H. R., and Frazier, O. H. (2014). Left ventricular assist device outflow graft: alternative sites. *Annals of cardiothoracic surgery*, 3:541–545.
- Aigner, P., Schlöglhofer, T., Plunger, L. C., Beitzke, D., Wielandner, A., Schima, H., Zimpfer, D., and Moscato, F. (2021). Pump position and thrombosis in ventricular assist devices: Correlation of radiographs and ct data. *International Journal of Artificial Organs*, 44:956–964.
- Akutsu, T. and Kolff, W. (1958). Permanent substitutes for valves and hearts. *American Society for Artificial Internal Organs*, 4:230–234.
- Alonazi, K. A., Lovell, N. H., and Dokos, S. (2015). Simulation of aortic valve dynamics during ventricular support. *Proceedings of the Annual International Conference of the IEEE Engineering in Medicine and Biology Society, EMBS*, 2015-Novem:1881–1885.
- Alpert, C. M., Smith, M. A., Hummel, S. L., and Hummel, E. K. (2017). Symptom burden in heart failure: assessment, impact on outcomes, and management. *Heart Failure Reviews*, 22:25–39.
- Amidror, I. (2002). Scattered data interpolation methods for electronic imaging systems: a survey. *Journal of Electronic Imaging*, 11:157.
- Anselmi, A., Collin, S., Haigron, P., Verhoye, J. P., and Flecher, E. (2016a). Virtual implantation and patient-specific simulation for optimization of outcomes in ventricular assist device recipients. *Medical Hypotheses*, 91:67–72.
- Anselmi, A., Collin, S., Haigron, P., Verhoye, J. P., and Flecher, E. (2016b). Virtual implantation and patient-specific simulation for optimization of outcomes in ventricular assist device recipients. *Medical Hypotheses*, 91:67–72.

- Anselmi, A., Collin, S., Haigron, P., Verhoye, J. P., and Flecher, E. (2017). Device-specific evaluation of intraventricular left ventricular assist device position by quantitative coaxiality analysis. *Journal of Surgical Research*, 213:110–114.
- Aymami, M., Donal, E., Guihaire, J., Helloco, A. L., Federspiel, M., Galli, E., Carré, F., Lelong, B., Chabanne, C., Corbineau, H., Leguerrier, A., Verhoye, J. P., and Flécher, E. (2016). Rest and exercise adaptation of the right ventricular function in long-term left ventricular assist device patients: A prospective, pilot study. *Journal of Cardiac Failure*, 22:240–241.
- Bachman, T. N., Bhamra, J. K., Verkaik, J., Vandenberghe, S., Kormos, R. L., and Antaki, J. F. (2011). In vitro evaluation of ventricular cannulation for rotodynamic cardiac assist devices. *Cardiovascular Engineering and Technology*, 2:203–211.
- Bantis, L. E., Nakas, C. T., and Reiser, B. (2019). Construction of confidence intervals for the maximum of the youden index and the corresponding cutoff point of a continuous biomarker. *Biometrical Journal*, 61:138–156.
- Ben Abid, A., Morgenthaler, V., Aymami, M., Flecher, E., and Haigron, P. (2021). A CFD based analysis of the influence of IC angulation on blood stagnation for Left Ventricular Assist Device implantation. In *2020 IEEE-EMBS Conference on Biomedical Engineering and Sciences (IECBES)*, pages 218–223. IEEE.
- Ben Abid, A., MORGENTHALER, V., HAIGRON, P., and FLECHER, E. (2019). CFD based study of blood stagnation caused by LVAD inflow cannula angulation. In *SURGETICA International Conference on Computer-Assisted Medical Inter-ventions: scientific problems, tools and clinical applications*, pages 112–114. SURGETICA International Conference on Computer-Assisted Medical Inter-ventions: scientific problems, tools and clinical applications.
- Beyersdorf, F., Scheumann, J., and Siepe, M. (2017). Implantation of the heartmate 3—description of the surgical technique. *Operative Techniques in Thoracic and Cardiovascular Surgery*, 22:173–185.
- Bonnemain, J., Malossi, A. C. I., Lesinigo, M., Deparis, S., Quarteroni, A., and von Segesser, L. K. (2013). Numerical simulation of left ventricular assist device implantations: Comparing the ascending and the descending aorta cannulations. *Medical Engineering & Physics*, 35:1465–1475.
- Brink, J. G. and Hassoulas, J. (2009). The first human heart transplant and further advances in cardiac transplantation at groote schuur hospital and the university of cape town. *Cardiovascular Journal of Africa*, 20:31–36.
- Bytyçi, I. and Bajraktari, G. (2015). Mortality in heart failure patients. *Anadolu Kardiyoloji Dergisi/The Anatolian Journal of Cardiology*, 15:63–68.

- Carlhäll, C. J. and Bolger, A. (2010). Passing strange flow in the failing ventricle. *Circulation: Heart Failure*, 3:326–331.
- Carrascal, P. G., García, J. G., Pallares, J. S., Ruiz, F. C., and Martín, F. J. M. (2017). Numerical study of blood clots influence on the flow pattern and platelet activation on a stented bifurcation model. *Annals of Biomedical Engineering*, 45:1279–1291.
- Chair, S. Y., Yu, D. S., Ng, M. T., Wang, Q., Cheng, H. Y., Wong, E. M., and Sit, J. W. (2016). Evolvement of left ventricular assist device: The implications on heart failure management. *Journal of Geriatric Cardiology*, 13:425–430.
- Chakraborty, P., Balachandar, S., and Adrian, R. J. (2005). On the relationships between local vortex identification schemes. *Journal of Fluid Mechanics*, 535:189–214.
- Chatel, D., Martin-Bouyer, Y., Vicaut, E., Bouchoucha, H., Achard, F., Sablayrolles, J. L., and Carpentier, A. (1993). Criteria for anatomical compatibility of the total artificial heart: computerized three-dimensional modeling of the cardiovascular anatomy. *Artificial Organs*, 17:1022–1035.
- Chen, H., Li, D., Bai, R., and Wang, X. (2018). Comparison of swirling strengths derived from two- and three-dimensional velocity fields in channel flow. *AIP Advances*, 8.
- Chiu, W. C., Alemu, Y., Mclarty, A. J., Einav, S., Slepian, M. J., and Bluestein, D. (2017). Ventricular assist device implantation configurations impact overall mechanical circulatory support system thrombogenic potential. *ASAIO Journal*, 63:285–292.
- Chivukula, V. K., Beckman, J. A., Li, S., Masri, S. C., Levy, W. C., Lin, S., Cheng, R. K., Farris, S. D., Wood, G., Dardas, T. F., Kirkpatrick, J. N., Koomalsingh, K., Zimpfer, D., MacKensen, G. B., Chassagne, F., Mahr, C., and Aliseda, A. (2020). Left ventricular assist device inflow cannula insertion depth influences thrombosis risk. *ASAIO Journal*, pages 766–773.
- Chivukula, V. K., Beckman, J. A., Prisco, A. R., Dardas, T., Lin, S., Smith, J. W., Mokadam, N. A., Aliseda, A., and Mahr, C. (2018). Left ventricular assist device inflow cannula angle and thrombosis risk. *Circulation: Heart Failure*, 11:1–9.
- Chorro, F. J., Such-Belenguier, L., and López-Merino, V. (2009). Modelos animales de enfermedad cardiovascular. *Revista Espanola de Cardiologia*, 62:69–84.
- Chung, J. S., Emerson, D., Megna, D., and Arabia, F. A. (2020). Total artificial heart: Surgical technique in the patient with normal cardiac anatomy. *Annals of Cardiothoracic Surgery*, 9:81–88.
- Cohn, W. E., Timms, D. L., and Frazier, O. H. (2015). Total artificial hearts: Past, present, and future. *Nature Reviews Cardiology*, 12:609–617.



- Collin, S. (2018). *Preoperative planning and simulation for artificial heart implantation surgery*. PhD thesis, MATHSTIC - Université de Rennes 1.
- Colvin, M., Smith, J. M., Hadley, N., Skeans, M. A., Uccellini, K., Goff, R., Foutz, J., Israni, A. K., Snyder, J. J., and Kasiske, B. L. (2020). Optn/srtr 2018 annual data report: Heart. *American Journal of Transplantation*, 20:340–426.
- Copeland, J. G., Arabia, F. A., Smith, R. G., Sethi, G. K., Nolan, P. E., and Banchy, M. E. (1999). Arizona experience with cardiowest total artificial heart bridge to transplantation. *The Annals of Thoracic Surgery*, 68:756–760.
- Copeland, J. G., Copeland, H., Gustafson, M., Mineburg, N., Covington, D., Smith, R. G., and Friedman, M. (2012). Experience with more than 100 total artificial heart implants. *Journal of Thoracic and Cardiovascular Surgery*, 143:727–734.
- Cucitore, R., Quadrio, M., and Baron, A. (1999). On the effectiveness and limitations of local criteria for the identification of a vortex. *European Journal of Mechanics, B/Fluids*, 18:261–282.
- Cuttone, F., Debauchez, M., Saplacan, V., Desgué, J., and Massetti, M. (2011). L'assistance ventriculaire mécanique. *Sang Thrombose Vaisseaux*, 23:539–544.
- Dickstein, K., Cohen-Solal, A., Filippatos, G., McMurray, J. J., Ponikowski, P., Poole-Wilson, P. A., Stromberg, A., van Veldhuisen, D. J., Atar, D., Hoes, A. W., Keren, A., Mebazaa, A., Nieminen, M., Priori, S. G., Swedberg, K., Vahanian, A., Camm, J., Caterina, R. D., Dean, V., Dickstein, K., Filippatos, G., Funck-Brentano, C., Hellems, I., Kristensen, S. D., McGregor, K., Sechtem, U., Silber, S., Tendera, M., Widimsky, P., Zamorano, J. L., Tendera, M., Auricchio, A., Bax, J., Bohm, M., Corra, U., della Bella, P., Elliott, P. M., Follath, F., Gheorghide, M., Hasin, Y., Hernborg, A., Jaarsma, T., Komajda, M., Kornowski, R., Piepoli, M., Prendergast, B., Tavazzi, L., Vachiery, J.-L., Verheugt, F. W. A., Zamorano, J. L., and Zannad, F. (2008). Esc guidelines for the diagnosis and treatment of acute and chronic heart failure 2008: The task force for the diagnosis and treatment of acute and chronic heart failure 2008 of the european society of cardiology. developed in collaboration with the heart failure association of the esc (hfa) and endorsed by the european society of intensive care medicine (esicm). *European Heart Journal*, 29:2388–2442.
- Drummond, A. and Antaki, J. (2008). Virtual fit study of pediatric heart assist system. *Digital Human Modeling: Trends in Human Algorithms*, pages 71–89.
- Drummond, A., Bachman, T., and Antaki, J. (2006). Three-dimensional virtual anatomic fit study for an implantable pediatric ventricular assist device. *Lecture Notes in Computer Science (including subseries Lecture Notes in Artificial Intelligence and Lecture Notes in Bioinformatics)*, 3994 LNCS:855–861.

- Elbaz, M. S., Calkoen, E. E., Westenberg, J. J., Lelieveldt, B. P., Roest, A. A., and Geest, R. J. V. D. (2014). Vortex flow during early and late left ventricular filling in normal subjects: Quantitative characterization using retrospectively-gated 4d flow cardiovascular magnetic resonance and three-dimensional vortex core analysis. *Journal of Cardiovascular Magnetic Resonance*, 16:1–12.
- Entezari, S., Shakiba, A., and Niazmand, H. (2021). Numerical investigation of the effects of cannula geometry on hydraulic blood flow to prevent the risk of thrombosis. *Computers in Biology and Medicine*, 134:104484.
- Estep, J. D., Stainback, R. F., Little, S. H., Torre, G., and Zoghbi, W. A. (2010). The role of echocardiography and other imaging modalities in patients with left ventricular assist devices. *JACC: Cardiovascular Imaging*, 3:1049–1064.
- European Directorate for the Quality of Medicines and Healthcare (EDQM) (2020). International figures on donation and transplantation 2019 - newsletter transplant vol 25.
- Evin, M., Callaghan, F., Fletcher, D. F., and Grieve, S. M. (2019). Left ventricle vortex detection by 3d + t phase contrast mri: a feasibility study. *Computer Methods in Biomechanics and Biomedical Engineering*, 22:S71–S73.
- Feldman, D., Pamboukian, S. V., Teuteberg, J. J., Birks, E., Lietz, K., Moore, S. A., Morgan, J. A., Arabia, F., Bauman, M. E., Buchholz, H. W., Eng, M., Dickstein, M. L., El-Banayosy, A., Elliot, T., Goldstein, D. J., Grady, K. L., Jones, K., Hryniewicz, K., John, R., Kaan, A., Kusne, S., Loebe, M., Massicotte, M. P., Moazami, N., Mohacsi, P., Mooney, M., Nelson, T., Pagani, F., Perry, W., Potapov, E. V., Rame, J. E., Russell, S. D., Sorensen, E. N., Sun, B., Strueber, M., Mangi, A. A., Petty, M. G., Rogers, J., and Rowe, A. W. (2013). The 2013 international society for heart and lung transplantation guidelines for mechanical circulatory support: Executive summary. *Journal of Heart and Lung Transplantation*, 32:157–187.
- Flécher, E. (2014). Assistance circulatoire mécanique de longue durée en 2014: Une alternative à la transplantation cardiaque? *Presse Medicale*, 43:809–812.
- Fotiadis, D. I. and Athanasiou, L. K. M. L. S. (2017). *Atherosclerotic Plaque Characterization Methods Based on Coronary Imaging*. Elsevier Science.
- Fraser, K. H., Zhang, T., Taskin, M. E., Griffit, B. P., and Wu, Z. J. (2011). Computational fluid dynamics analysis of thrombosis potential in left ventricular assist device drainage cannulae. *ASAIO journal (American Society for Artificial Internal Organs: 1992)*, 56:157–163.
- Fraser, K. H., Zhang, T., Taskin, M. E., Griffith, B. P., and Wu, Z. J. (2010). Computational fluid dynamics analysis of thrombosis potential in left ventricular assist device drainage cannulae. *ASAIO Journal*, 56:157–163.

- Fritschi, A., Laumen, M., Spiliopoulos, S., Finocchiaro, T., Egger, C., Schmitz-Rode, T., Tenderich, G., Koerfer, R., and Steinseifer, U. (2013). Image based evaluation of mediastinal constraints for the development of a pulsatile total artificial heart. *BioMedical Engineering OnLine*, 12:81.
- Fujimoto, L. K., Smith, W. A., Jacobs, G. B., Pazirandeh, P., Kramer, J. R., Kiraly, R., Golding, L., Matsushita, S., and Nosé, Y. (1985). Anatomical considerations in the design of a long-term implantable human left ventricle assist system. *Artificial Organs*, 9:361–374.
- Ghodrati, M., Khienwad, T., Maurer, A., Moscato, F., Zonta, F., Schima, H., and Aigner, P. (2021). Validation of numerically simulated ventricular flow patterns during left ventricular assist device support. *International Journal of Artificial Organs*, 44:30–38.
- Ghodrati, M., Maurer, A., Schlöglhofer, T., Khienwad, T., Zimpfer, D., Beitzke, D., Zonta, F., Moscato, F., Schima, H., and Aigner, P. (2020). The influence of left ventricular assist device inflow cannula position on thrombosis risk. *Artificial Organs*, 44:939–946.
- Givertz, M. M. (2011). Ventricular assist devices: Important information for patients and families. *Circulation*, 124:305–311.
- Gohean, J. R., George, M. J., Pate, T. D., Kurusz, M., Longoria, R. G., and Smalling, R. W. (2013). Verification of a computational cardiovascular system model comparing the hemodynamics of a continuous flow to a synchronous valveless pulsatile flow left ventricular assist device. *ASAIO Journal*, 59:107–116.
- Gonzalez, R. C., Woods, R. E., and Eddins, S. L. (2003). *Digital Image Processing Using MATLAB*. Prentice-Hall, Inc.
- Groenewegen, A., Rutten, F. H., Mosterd, A., and Hoes, A. W. (2020). Epidemiology of heart failure. *European Journal of Heart Failure*, 22:1342–1356.
- Hajian-Tilaki, K. (2013). Receiver Operating Characteristic (ROC) Curve Analysis for Medical Diagnostic Test Evaluation. *Caspian journal of internal medicine*, 4(2):627–35.
- Hall, C. W., Liotta, D., and Bakey, M. E. D. (1967). Bioengineering efforts in developing artificial hearts and assistors. *The American Journal of Surgery*, 114:24–30.
- Hanke, J., Rojas, S., Avsar, M., Haverich, A., and Schmitto, J. (2015). Minimally-invasive lvad implantation: State of the art. *Current Cardiology Reviews*, 11:246–251.
- Hellmuth, R., Bruzzi, M. S., and Quinlan, N. J. (2016). Analysis of shear-induced platelet aggregation and breakup. *Annals of Biomedical Engineering*, 44:914–928.

- Herman, I. P. (2010). Physics of the human body. *Choice Reviews Online*, 48:48–0858–48–0858.
- Hsu, P. L., McIntyre, M., Boehning, F., Dang, W., Parker, J., Autschbach, R., Schmitz-Rode, T., and Steinseifer, U. (2016). In-series versus in-parallel mechanical circulatory support for the right heart: A simulation study. *Artificial Organs*, 40:561–567.
- Imamura, T., Narang, N., Nitta, D., Fujino, T., Nguyen, A., Kim, G., Raikhelkar, J., Rodgers, D., Ota, T., Jeevanandam, V., Sayer, G., and Uriel, N. (2020). Optimal cannula positioning of heartmate 3 left ventricular assist device. *Artificial Organs*, 44:e509–e519.
- Inamdar, A. and Inamdar, A. (2016). Heart failure: Diagnosis, management and utilization. *Journal of Clinical Medicine*, 5:62.
- Jeong, J. and Hussain, F. (1995). On the identification of a vortex. *Journal of Fluid Mechanics*, 285:69–94.
- Jhun, C.-S., Sun, K., and Cysyk, J. P. (2014). Continuous flow left ventricular pump support and its effect on regional left ventricular wall stress: finite element analysis study. *Medical & Biological Engineering & Computing*, 52:1031–1040.
- John, R., Mantz, K., Eckman, P., Rose, A., and May-Newman, K. (2010). Aortic valve pathophysiology during left ventricular assist device support. *Journal of Heart and Lung Transplantation*, 29:1321–1329.
- Kadado, A. J., Akar, J. G., and Hummel, J. P. (2018). Arrhythmias after left ventricular assist device implantation: Incidence and management. *Trends in Cardiovascular Medicine*, 28:41–50.
- Kamarudin, A. N., Cox, T., and Kolamunnage-Dona, R. (2017). Time-dependent roc curve analysis in medical research: current methods and applications. *BMC Medical Research Methodology*, 17:53.
- Khanna, S., Bhat, A., Chen, H. H., Tan, J. W., Gan, G. C., and Tan, T. C. (2020). Left ventricular sphericity index is a reproducible bedside echocardiographic measure of geometric change between acute phase takotsubo’s syndrome and acute anterior myocardial infarction. *IJC Heart and Vasculature*, 29:100547.
- Kheradvar, A., Milano, M., and Gharib, M. (2007). Correlation between vortex ring formation and mitral annulus dynamics during ventricular rapid filling. *ASAIO Journal*, 53:8–16.
- Kheradvar, A. and Pedrizzetti, G. (2012). *Vortex Formation in the Cardiovascular System*. Springer London.

- Khush, K. K., Cherikh, W. S., Chambers, D. C., Harhay, M. O., Hayes, D., Hsich, E., Meiser, B., Potena, L., Robinson, A., Rossano, J. W., Sadavarte, A., Singh, T. P., Zuckermann, A., and Stehlik, J. (2019). The international thoracic organ transplant registry of the international society for heart and lung transplantation: Thirty-sixth adult heart transplantation report — 2019; focus theme: Donor and recipient size match. *Journal of Heart and Lung Transplantation*, 38:1056–1066.
- Kida, S. and Miura, H. (1998). Identification and analysis of vortical structures. *European Journal of Mechanics - B/Fluids*, 17:471–488.
- Kirişli, H. A., Schaap, M., Klein, S., Papadopoulou, S. L., Bonardi, M., Chen, C. H., Weustink, A. C., Mollet, N. R., Vonken, E. J., van der Geest, R. J., van Walsum, T., and Niessen, W. J. (2010). Evaluation of a multi-atlas based method for segmentation of cardiac cta data: a large-scale, multicenter, and multivendor study. *Medical Physics*, 37:6279–6291.
- Kirklin, J. K. ., Collum, C., Timkovich, N., Hollifield, K., and Cleggett, M. (2017). Interagency registry for mechanically assisted circulatory support (intermacs) quarterly statistical report 2017 q2. implant and event dates: June 23, 2006 to june 30, 2017. *The Data and Clinical Coordinating Center University of Alabama at Birmingham*.
- Kirklin, J. K., Naftel, D. C., Myers, S. L., Pagani, F. D., and Colombo, P. C. (2020). Quantifying the impact from stroke during support with continuous flow ventricular assist devices: An sts intermacs analysis. *Journal of Heart and Lung Transplantation*, 39:782–794.
- Kirklin, J. K., Naftel, D. C., Pagani, F. D., Kormos, R. L., Stevenson, L. W., Blume, E. D., Myers, S. L., Miller, M. A., Baldwin, J. T., and Young, J. B. (2015). Seventh intermacs annual report: 15,000 patients and counting. *Journal of Heart and Lung Transplantation*, 34:1495–1504.
- Klabunde, R. (2017). Cv physiology | ventricular pressure-volume relationship.
- Klotz, S., Meyer-Saraei, R., Frydrychowicz, A., Scharfschwerdt, M., Putman, L. M., Halder, S., and Sievers, H. H. (2016). Proposing a novel technique to exclude the left ventricle with an assist device: Insights from 4-dimensional flow magnetic resonance imaging. *European Journal of Cardio-thoracic Surgery*, 50:439–445.
- Kolář, V. (2007). Vortex identification: New requirements and limitations. *International Journal of Heat and Fluid Flow*, 28:638–652.
- Komoda, T., Uyama, C., Maeta, H., and Ozaki, K. (1992). Study of anatomic constraints using three dimensionally reconstructed images for total artificial heart implantation. *ASAIO Journal*, 38:M564–M569.

- Korakianitis, T. and Shi, Y. (2007). Numerical comparison of hemodynamics with atrium to aorta and ventricular apex to aorta vad support. *ASAIO Journal*, 53:537–548.
- Laumen, M., Kaufmann, T., Timms, D., Schlanstein, P., Jansen, S., Gregory, S., Wong, K. C., Schmitz-Rode, T., and Steinseifer, U. (2010). Flow analysis of ventricular assist device inflow and outflow cannula positioning using a naturally shaped ventricle and aortic branch. *Artificial Organs*, 34:798–806.
- Leong, X. F., Ng, C. Y., and Jaarin, K. (2015). Animal models in cardiovascular research: Hypertension and atherosclerosis. *BioMed Research International*, 2015.
- Li, X., Bai, J., and He, P. (2002). Simulation study of the hemopump as a cardiac assist device. *Medical and Biological Engineering and Computing*, 40:344–353.
- Liao, S., Neidlin, M., Li, Z., Simpson, B., and Gregory, S. D. (2018). Ventricular flow dynamics with varying lvad inflow cannula lengths: In-silico evaluation in a multiscale model. *Journal of Biomechanics*, 72:106–115.
- Little, B. . C. (1994). Classification of functional capacity and objective assessment. *American Heart Association*.
- Litwak, K. N., Koenig, S. C., Cheng, R. C., Giridharan, G. A., Gillars, K. J., and Pantalos, G. M. (2005). Ascending aorta outflow graft location and pulsatile ventricular assist provide optimal hemodynamic support in an adult mock circulation. *Artificial Organs*, 29:629–635.
- Litwak, K. N., Unger, L. S., Fukamachi, K., and Saeed, D. (2008). Retrospective analysis of adverse events in preclinical ventricular assist device experiments. *ASAIO Journal*, 54:347–350.
- Liu, G. M., Chen, H. B., Luo, F. L., Zhang, Y., Sun, H. S., Zhou, J. Y., and Hu, S. S. (2012). Numerical simulation of lvad inflow cannulas with different tip. *International Journal of Chemical Engineering*, 2012.
- Lumen Learning (2015). Cardiac cycle | anatomy and physiology ii.
- Mandrekar, J. N. (2010). Receiver operating characteristic curve in diagnostic test assessment. *Journal of Thoracic Oncology*, 5(9):1315–1316.
- May-Newman, K., Marquez-Maya, N., Montes, R., and Salim, S. (2019a). The effect of inflow cannula angle on the intraventricular flow field of the left ventricular assist device-assisted heart: An in vitro flow visualization study. *ASAIO Journal*, 65:139–147.

- May-Newman, K., Montes, R., Campos, J., Marquez-Maya, N., Vu, V., Zebrowski, E., Motomura, T., and Benkowski, R. (2019b). Reducing regional flow stasis and improving intraventricular hemodynamics with a tipless inflow cannula design: An in vitro flow visualization study using the evaheart lvad. *Artificial Organs*, 43:834–848.
- May-Newman, K., Moon, J., Ramesh, V., Montes, R., Campos, J., Herold, B., Isingoma, P., Motomura, T., and Benkowski, R. (2017). The effect of inflow cannula length on the intraventricular flow field: An in vitro flow visualization study using the evaheart left ventricular assist device. *ASAIO Journal*, 63:592–603.
- Mazzitelli, R., Condemni, F., Renzulli, A., Serraino, G. F., and Fragomeni, G. (2013). Three-dimensional numerical simulations of the aortic flow in presence of a left ventricle assist device with two outflow graft placements. *International Journal of Privacy and Health Information Management*, 1:76–95.
- McCormick, M., Nordsletten, D., Kay, D., and Smith, N. (2011). Modelling left ventricular function under assist device support. *International Journal for Numerical Methods in Biomedical Engineering*, 27:1073–1095.
- McCormick, M., Nordsletten, D., Vecchi, A. D., Kay, D., and Smith, N. P. (2009). Fluid-mechanics simulations of ventricular function under lvad support. *IFMBE Proceedings*, 25:1572–1575.
- McCormick, M., Nordsletten, D. A., Kay, D., and Smith, N. P. (2013). Simulating left ventricular fluid-solid mechanics through the cardiac cycle under lvad support. *Journal of Computational Physics*, 244:80–96.
- Moin, P. and Kim, J. (1985). The structure of the vorticity field in turbulent channel flow. part 1. analysis of instantaneous fields and statistical correlations. *Journal of Fluid Mechanics*, 155:441.
- Moore, R. A., Lorts, A., Madueme, P. C., Taylor, M. D., and Morales, D. L. (2016). Virtual implantation of the 50cc syncardia total artificial heart. *The Journal of Heart and Lung Transplantation*, 35:824–827.
- Moore, R. A., Madueme, P. C., Lorts, A., Morales, D. L. S., and Taylor, M. D. (2014). Virtual implantation evaluation of the total artificial heart and compatibility: Beyond standard fit criteria. *The Journal of Heart and Lung Transplantation*, 33:1180–3.
- Morris, P. D., Narracott, A., Tengg-Kobligk, H. V., Soto, D. A. S., Hsiao, S., Lungu, A., Evans, P., Bressloff, N. W., Lawford, P. V., Hose, D. R., and Gunn, J. P. (2016). Computational fluid dynamics modelling in cardiovascular medicine. *Heart*, 102:18–28.

- Motomura, T., Tuzun, E., Yamazaki, K., Tatsumi, E., Benkowski, R., and Yamazaki, S. (2019). Preclinical evaluation of the evaheart 2 centrifugal left ventricular assist device in bovines. *ASAIO Journal*, 65:845–854.
- National Heart, Lung, and Blood Institute (NHLBI) (2022). Total artificial heart - how does it work?
- Noecker, A. M., Cingoz, F., Ootaki, Y., Liu, J., Kuzmiak, S., Kopcak, M. W., Fukamachi, K., and Duncan, B. W. (2007). The cleveland clinic pedipump: anatomic modeling and virtual fitting studies in a lamb model. *Asaio J*, 53:716–719.
- Ong, C., Dokos, S., Chan, B., Lim, E., Abed, A. A., Osman, N. A. B. A., Kadiman, S., and Lovell, N. H. (2013). Numerical investigation of the effect of cannula placement on thrombosis. *Theoretical biology & medical modelling*, 10:35.
- Ong, C. W., Chan, B. T., Lim, E., Osman, N. A. A., Abed, A. A., Dokos, S., and Lovell, N. H. (2012). Fluid structure interaction simulation of left ventricular flow dynamics under left ventricular assist device support. *2012 Annual International Conference of the IEEE Engineering in Medicine and Biology Society*, pages 6293–6296.
- Otsu, N. (1979). A threshold selection method from gray-level histograms. *IEEE Transactions on Systems, Man, and Cybernetics*, 9:62–66.
- Park, S. S., Sanders, D. B., Smith, B. P., Ryan, J., Plasencia, J., Osborn, M. B., Wellnitz, C. M., Southard, R. N., Pierce, C. N., Arabia, F., Lane, J., Frakes, D., Velez, D., Pophal, S. G., and Nigro, J. J. (2014). Total artificial heart in the pediatric patient with biventricular heart failure. *Perfusion*, 29:82–8.
- Peta, A. (2018). Principles of management of acute heart failure. In *College of Intensive Care Medicine (CICM)*. SlideShare.
- Peyvandi, F., Garagiola, I., and Baronciani, L. (2011). Role of von willebrand factor in the haemostasis. *Blood transfusion = Trasfusione del sangue*, 9 Suppl 2:s3–8.
- Porter, T. R., Shillcutt, S. K., Adams, M. S., Desjardins, G., Glas, K. E., Olson, J. J., and Troughton, R. W. (2015). Guidelines for the use of echocardiography as a monitor for therapeutic intervention in adults: A report from the american society of echocardiography. *Journal of the American Society of Echocardiography*, 28:40–56.
- Prisco, A. R., Aliseda, A., Beckman, J. A., Mokadam, N. A., Mahr, C., and Garcia, G. J. (2017). Impact of lvad implantation site on ventricular blood stagnation. *ASAIO Journal*, 63:392–400.
- Quaini, A., Čanić, S., and Paniagua, D. (2011). Numerical characterization of hemodynamics conditions near aortic valve after implantation of left ventricular assist device. *Mathematical Biosciences and Engineering*, 8:785–806.



- Rogers, J. G., Aaronson, K. D., Boyle, A. J., Russell, S. D., Milano, C. A., Pagani, F. D., Edwards, B. S., Park, S., John, R., Conte, J. V., Farrar, D. J., and Slaughter, M. S. (2010). Continuous flow left ventricular assist device improves functional capacity and quality of life of advanced heart failure patients. *Journal of the American College of Cardiology*, 55:1826–1834.
- Rojano, R. M., Zhussupbekov, M., and Antaki, J. F. (2021). Multi-constituent simulation of thrombus formation at lvad inlet cannula connection: Importance of virchow's triad. *Artificial Organs*, 45:1014–1023.
- Ruggeri, Z. M., Orje, J. N., Habermann, R., Federici, A. B., and Reininger, A. J. (2006). Activation-independent platelet adhesion and aggregation under elevated shear stress. *Blood*, 108:1903–1910.
- Ryan, A. J., Brougham, C. M., Garcarena, C. D., Kerrigan, S. W., and O'Brien, F. J. (2016). Towards 3d in vitro models for the study of cardiovascular tissues and disease. *Drug Discovery Today*, 21:1437–1445.
- Ryan, J., Teal, J., Pophal, S., Nigro, J., Adachi, I., Jaquiss, R., Frakes, D., Jarvik, R., and Baldwin, T. (2017). Virtual implantation of the infant jarvik 2015 for eligibility criteria establishment. *The Journal of Heart and Lung Transplantation*, 36:S13–S14.
- Saad, J., Asuka, E., and Schoenberger, L. (2022). *Physiology, Platelet Activation*. StatPearls Publishing.
- Sacks, J., Gonzalez-Stawinski, G. V., Hall, S., Lima, B., MacHannaford, J., Dockery, W., Cura, M., and Chamogeorgakis, T. (2015). Utility of cardiac computed tomography for inflow cannula patency assessment and prediction of clinical outcome in patients with the heartmate ii left ventricular assist device. *Interactive CardioVascular and Thoracic Surgery*, 21:590–593.
- Schlöglhofer, T., Aigner, P., Migas, M., Beitzke, D., Dimitrov, K., Wittmann, F., Riebandt, J., Granegger, M., Wiedemann, D., Laufer, G., Moscato, F., Schima, H., and Zimpfer, D. (2022). Inflow cannula position as risk factor for stroke in patients with heartmate 3 left ventricular assist devices. *Artificial organs*, pages 1–9.
- Schmid, C., Jurmann, M., Birnbaum, D., Colombo, T., Falk, V., Feltrin, G., Garatti, A., Genoni, M., Gerosa, G., Göttel, P., Gummert, J., Halfmann, R., Hammel, D., Hennig, E., Kaufmann, F., Lanfranconi, M., Meyns, B., Mohr, F., Müller, J., Nikolov, D., Rucinkas, K., Scheld, H.-H., Schmid, F.-X., Schneider, M., Sirvydis, V., Tandler, R., Vitali, E., Vlasselaers, D., Weyand, M., Wilhelm, M., and Hetzer, R. (2008). Influence of inflow cannula length in axial-flow pumps on neurologic adverse event rate: Results from a multi-center analysis. *The Journal of Heart and Lung Transplantation*, 27:253–260.

- School of Health Sciences (2009). Cardiac conduction system - normal function of the heart - cardiology teaching package - practice learning - division of nursing - the university of nottingham.
- Shadden, S. C., Lekien, F., and Marsden, J. E. (2005). Definition and properties of lagrangian coherent structures from finite-time lyapunov exponents in two-dimensional aperiodic flows. *Physica D: Nonlinear Phenomena*, 212:271–304.
- Sonntag, S. J., Lipinski, E., Neidlin, M., Hugenothe, K., Benkowski, R., Motomura, T., and Kaufmann, T. A. S. (2019). Virtual fitting and hemodynamic simulation of the evaheart 2 left ventricular assist device and double-cuff tipless inflow cannula. *ASAIO Journal*, 65:698–706.
- Stewart, G. C. and Givertz, M. M. (2012). Mechanical circulatory support for advanced heart failure: Patients and technology in evolution. *Circulation*, 125:1304–1315.
- Stewart, G. C. and Stevenson, L. W. (2011). Keeping left ventricular assist device acceleration on track. *Circulation*, 123:1559–1568.
- Sukavaneshvar, S., Rosa, G. M., and Solen, K. A. (2000). Enhancement of stent-induced thromboembolism by residual stenoses: Contribution of hemodynamics. *Annals of Biomedical Engineering*, 28:182–193.
- Sunagawa, G., Horvath, D. J., Karimov, J. H., Moazami, N., and Fukamachi, K. (2016). Future prospects for the total artificial heart. *Expert Review of Medical Devices*, 13:191–201.
- Tainter, C. R., Braun, O., Teran, F., Nguyen, A. P., Robbins, K., O'Brien, E. O., McMullan, Z. M., Schmidt, U., Meier, A., Goebel, M., Pretorius, V., Brambatti, M., Adler, E. D., and Seethala, R. (2018). Emergency department visits among patients with left ventricular assist devices. *Internal and Emergency Medicine*, 13:907–913.
- Taylor, C. A. and Draney, M. T. (2004). Experimental and computational methods in cardiovascular fluid mechanics. *Annual Review of Fluid Mechanics*, 36:197–231.
- Taylor, C. J., Ordóñez-Mena, J. M., Roalfe, A. K., Lay-Flurrie, S., Jones, N. R., Marshall, T., and Hobbs, F. D. R. (2019). Trends in survival after a diagnosis of heart failure in the united kingdom 2000-2017: population based cohort study. *BMJ*, 364:l223.
- Taylor, C. J., Rutten, F. H., Brouwer, J. R., and Hobbs, F. R. (2017). Practical guidance on heart failure diagnosis and management in primary care: recent epccs recommendations. *British Journal of General Practice*, 67:326–327.
- Teuteberg, J. J., Cleveland, J. C., Cowger, J., Higgins, R. S., Goldstein, D. J., Keebler, M., Kirklin, J. K., Myers, S. L., Salerno, C. T., Stehlik, J., Fernandez, F., Badhwar, V.,

- Pagani, F. D., and Atluri, P. (2020). The society of thoracic surgeons intermacs 2019 annual report: The changing landscape of devices and indications. *The Annals of Thoracic Surgery*, 109:649–660.
- Tsukiya, T., Toda, K., Sumikura, H., Takewa, Y., Watanabe, F., Taenaka, Y., and Tsumi, E. (2011). Computational fluid dynamic analysis of the flow field in the newly developed inflow cannula for a bridge-to-decision mechanical circulatory support. *Journal of Artificial Organs*, 14:381–384.
- Tuppin, P., Cuerq, A., de Peretti, C., Fagot-Campagna, A., Danchin, N., Juillière, Y., Alla, F., Allemand, H., Bauters, C., Drici, M.-D., Hagège, A., Jondeau, G., Jourdain, P., Leizorovicz, A., and Paccaud, F. (2014). Two-year outcome of patients after a first hospitalization for heart failure: A national observational study. *Archives of Cardiovascular Diseases*, 107:158–168.
- Töger, J., Kanski, M., Carlsson, M., Kovács, S. J., Söderlind, G., Arheden, H., and Heiberg, E. (2012). Vortex ring formation in the left ventricle of the heart: Analysis by 4d flow mri and lagrangian coherent structures. *Annals of Biomedical Engineering*, 40:2652–2662.
- Velagaleti, R. S. and Vasan, R. S. (2007). Heart failure in the twenty-first century: Is it a coronary artery disease or hypertension problem? *Cardiology Clinics*, 25:487–495.
- Walter, E. M. D. and Hetzer, R. (2013). Surgical treatment concepts for heart failure. *HSR proceedings in intensive care & cardiovascular anesthesia*, 5:69–75.
- Warriner, R. K., Haddad, M., Hendry, P. J., and Mussivand, T. (2004). Virtual anatomical three-dimensional fit trial for intra-thoracically implanted medical devices. *ASAIO Journal*, 50:354–359.
- Wilson, S. R., Mudge, G. H., Stewart, G. C., and Givertz, M. M. (2009). Evaluation for a ventricular assist device: Selecting the appropriate candidate. *Circulation*, 119:2225–2232.
- Wu, W.-T., Jamiolkowski, M. A., Wagner, W. R., Aubry, N., Massoudi, M., and Antaki, J. F. (2017). Multi-constituent simulation of thrombus deposition. *Scientific Reports*, 7:42720.
- Yancy, C. W., Jessup, M., Bozkurt, B., Butler, J., Casey, D. E., Drazner, M. H., Fonarow, G. C., Geraci, S. A., Horwich, T., Januzzi, J. L., Johnson, M. R., Kasper, E. K., Levy, W. C., Masoudi, F. A., McBride, P. E., McMurray, J. J., Mitchell, J. E., Peterson, P. N., Riegel, B., Sam, F., Stevenson, L. W., Tang, W. W., Tsai, E. J., and Wilkoff, B. L. (2013). 2013 accf/aha guideline for the management of heart failure. *Circulation*, 128.

- Yushkevich, P. A., Piven, J., Hazlett, H. C., Smith, R. G., Ho, S., Gee, J. C., and Gerig, G. (2006). User-guided 3d active contour segmentation of anatomical structures: Significantly improved efficiency and reliability. *NeuroImage*, 31:1116–1128.
- Zhang, B., Masuzawa, T., Tatsumi, E., Taenaka, Y., Uyama, C., Takano, H., and Takamiya, M. (1999). Three-dimensional thoracic modeling for an anatomical compatibility study of the implantable total artificial heart. *Artificial Organs*, 23:229–234.
- Zhang, B., Tatsumi, E., Taenaka, Y., Takano, H., and Masuzawa, T. (2000). Noninvasive assessment method to determine the anatomic compatibility of an implantable artificial heart system. *ASAIO Journal*, 46:590–595.
- Zhang, Q., Wang, C. M., Shi, S. T., Chen, H., and Zhou, Y. J. (2019). Relationship of left ventricular thrombus formation and adverse outcomes in acute anterior myocardial infarction in patients treated with primary percutaneous coronary intervention. *Clinical Cardiology*, 42:69–75.
- Zhang, Y., Liu, K., Xian, H., and Du, X. (2018). A review of methods for vortex identification in hydroturbines. *Renewable and Sustainable Energy Reviews*, 81:1269–1285.
- Zhou, B. Y., Xie, M. X., Wang, J., Wang, X. F., Lv, Q., Liu, M. W., Kong, S. S., Zhang, P. Y., and Liu, J. F. (2017). Relationship between the abnormal diastolic vortex structure and impaired left ventricle filling in patients with hyperthyroidism. *Medicine (United States)*, 96:1–7.
- Zhou, J., Adrian, R. J., Balachandar, S., and Kendall, T. M. (1999). Mechanisms for generating coherent packets of hairpin vortices in channel flow. *Journal of Fluid Mechanics*, 387:353–396.
- Zhou, X.-H., Obuchowski, N. A., and McClish, D. K. (2011). *Statistical Methods in Diagnostic Medicine, 2nd Edition*. John Wiley & Sons, Inc.



---

**Titre:** Analyse in silico du risque de thrombose pour l'implantation d'un dispositif d'assistance ventriculaire gauche.

**Mot clés:** Implantation DAVG, Analyse MFN, Marqueur Thrombogène Personnalisé

**Résumé:** L'implantation d'un dispositif d'assistance ventriculaire gauche (DAVG) est envisagée au stade final de l'insuffisance cardiaque. Elle peut cependant entraîner des complications. L'objectif de cette thèse est d'étudier l'influence des caractéristiques (longueur et angulation) de la Canule Apicale (CA) sur le risque de thrombose en considérant l'anatomie ventriculaire par une approche de la Mécanique des Fluides Numérique (MFN). Nous proposons, un modèle simplifié. L'hypothèse 2D est d'abord vérifiée en comparant un modèle 3D et son modèle 2D correspondant, les mêmes tendances hémodynamiques ont été trouvées. Le modèle proposé est ensuite utilisé pour analyser l'hémodynamique ventriculaire en fonction des caractéristiques de la CA et construire un Marqueur du Potentiel Thrombogène Personnalisé (MPTP) sur la base de la formation de vortex et de la mor-

phologie ventriculaire. Pour évaluer l'efficacité du marqueur, plusieurs cas cliniques sont étudiés (19 patients implantés avec HM2 & HM3). Les résultats sont comparés aux résultats cliniques. Le marqueur semble capable de distinguer avec précision les patients avec et sans complications pour les deux types pompes. Un large intervalle d'angulations de la CA est étudié et les résultats obtenus révèlent que le marqueur proposé semble capable de mettre en évidence des configurations et des profils thrombogènes. Si les caractéristiques de la CA influencent le risque de thrombose, les simulations suggèrent également que l'anatomie ventriculaire semble être un facteur déterminant de l'étendue de cette influence. Le pipeline de simulation proposé est une piste prometteuse vers le développement d'un système d'aide à la décision clinique.

---

**Title:** In silico thrombosis risk analysis for left ventricular assist device implantation

**Keywords:** LVAD implantation, CFD analysis, Personalised Thrombogenic Marker

**Abstract:** In the context of end stage heart failure, implantation of a Left Ventricular Assist Device (LVAD) is associated with serious complications. The aim of this thesis is to investigate the influence of IC features (length and angulation) on thrombosis risk by considering ventricular anatomy through a Computational Fluids Dynamics (CFD) approach. We propose a simplified model. The 2D assumption is first verified by comparing a 3D model and its corresponding 2D model, same haemodynamic tendencies were found. The proposed model is then used to analyse the influence of IC features on LV haemodynamic which allowed proposing a Personalised Thrombogenic Potential Marker (PTPM) based on vortices formation and ventricular morphology. To assess the marker effi-

ciency, several clinical cases are investigated (19 patients implanted with HM2 & HM3). PTPM results are compared to clinical outcome. The marker seems able to accurately distinguish between patients with and without LVAD related complications. A wide range of IC angulation is investigated and obtained results reveal that the proposed marker seems able to recognise thrombogenic configurations and highlighted thrombogenic profiles. While IC features do influence the thrombosis risk, simulations also suggest that the ventricular anatomy seems to be a determining factor of the extent of this influence. The proposed pipeline of simulation is a promising lead towards the development of a clinical decision support system.